Recycled Materials Resource Center

Final Report

Project 31

PERMEABLE REACTIVE BARRIERS FOR CONTAMINANT CONTROL IN

BENEFICIAL USE APPLICATIONS IN HIGHWAYS

Kevin H. Gardner

T. Taylor Eighmy

Carolina Gonzalez

Executive Summary

Reactive barriers are used to remediate contaminated sites where the potential for leaching of heavy metals exists. Permeable reactive barriers (PRB) could be used in highway applications below either embankments or base courses constructed with recycled materials where a possibility of contaminant leaching exists. The objective of this project is to develop technologies that use apatite minerals as permeable reactive barriers (PRB) applied in highway construction that use recycled materials in alternative construction applications.

Sorption of heavy metals and radionuclides onto apatite has been well demonstrated. Interest in apatite is primarily due to the high stability of the metal-phosphate minerals that result from the interaction between the contaminants and the apatite. However, the exact molecular scale mechanism of removal is not completely understood. This research sought to investigate the sorption mechanism using a combination of methods, including batch tests and surface analytical techniques, to study how Zn^{2+} is immobilized by apatite. Three different synthetic apatites were use in this investigation: hydroxyapatite ($Ca_5(PO_4)_3OH$), fluoroapatite ($Ca_5(PO_4)_3F$) and carbonate apatite ($Ca_5(PO_4,CO_3)_3(OH)$).

BET isotherms indicate that at low Zn^{2+} concentrations sorption proceeds as surface complexation and at increased concentrations it is followed by the formation of a co-precipitate and in turn a pure precipitate. The zeta potential analysis is in agreement with the proposed complexation – co-precipitation/precipitation mechanism. In this study

two distinct rates of change were observed in the surface charge (mV) of the apatite particle as a function of Zn^{2+} loading (mmol Zn/g Apatite).

The spectroscopic analysis indicates that co-precipitation begins to occur even at concentrations well below the solubility limit of Zn – minerals. The XAS spectra of HAP and CAP at 0.0016 mM had very strong similarities to the mineral structure of scholzite, a naturally occurring Zn-phosphate mineral and to synthetic zinc phosphate, respectively. At 0.92 - 0.99 mmol Zn/g apatite XPS identified scholzite and hopeite as likely species present at the particle surface. It is proposed that dissolution-precipitation reactions account for the formation of a Zn-phosphate solid solution, this indicates that co-precipitation begins to occur well before the maximum sorption capacity, q_{max}, predicted by the Langmuir isotherm.

At the elevated Zn^{2+} loadings of all three apatites, 8.22 mmol/g HAP, 4.48 mmol/g CAP and 2.74 mmol/g FAP, XAS evidenced similarities to hydrozincite, $(Zn_5(CO_3)_2(OH)_6)$ and XPS identified the likely presence of zinc carbonate hydroxide, $[ZnCO_3]_2 \cdot [Zn(OH)_2]$. The formation of a zinc carbonate hydroxide implies that dissolved CO_3 plays an important role in the complexation of Zn^{2+}, under the given experimental conditions.

Results from this research suggest that surface complexation, surface precipitation, co-precipitation and precipitation all play an important role in the sorption mechanism of Zn^{2+} onto apatite. This identification of a Zn-phosphate co-precipitate and hydrozincite emphasize that although the formation of Zn-phosphates does occur, competing reactions also lead to the formation of other Zn complexes such as Zn carbonates and/or hydroxides.

CHAPTER 3

MATERIALS

Three different synthetic apatites were used in this experiment: hydroxyapatite ($Ca_5(PO_4)_3OH$), fluoroapatite ($Ca_5(PO_4)_3F$) and carbonate apatite ($Ca_5(PO_4,CO_3)_3(OH)$). Synthetic apatites were used so that impurities in the system did not interfere with the analysis of the molecular scale sorption mechanism. Zinc was selected because not much information is available in comparison to other heavy metals (Pb, Cd, etc.) regarding its sorption behavior onto apatite.

3.1. Apatite Production

Apatite is widely mined both in the U.S. and worldwide. According to the USGS (2004), 37 million tons of marketable product was mined in the U.S. in 2004 at a value of approximately 1 billion US dollars. The main deposits of the mineral are found in Florida and North Carolina (85%) with important quarries also found in Idaho and Utah. The United States is the main producer of phosphate rock, followed by Morocco. It is mined primarily for the production of phosphoric acid and superphosphoric acid, which are in turn used for the production of animal feed supplements and fertilizers, in addition to industrial applications (USGS, 2004).

Phosphate rock is mined mostly through large-scale surface methods, including opencast dragline or open-pit shovel/excavator mining methods (UNEP, 2001). After the phosphate rock has been excavated the first step is to separate the large rock and sand

from the fines, which are used in the production processes. The sand that is discarded in this initial phase is this portion that is of interest for the construction of PRBs, as it has the structural properties that are necessary for being used as a construction material and it also has the geochemical properties that make it desirable for remediation purposes. Using the fraction that is not utilized for the production of phosphoric acid gives economic value to what otherwise would be considered a waste product.

3.2.   Apatite Mineralogy

An understanding of the basic crystallography of apatite is important in order to study the possible mechanisms by which Zn is incorporated into a geologically stable mineral. Apatite is a calcium phosphate mineral with the basic formula: $Ca_5(PO_4)_3X$, where X can be substituted by a halide (fluorine, chlorine, bromine), a hydroxyl group, or a carbonate group. Pure apatite is hard to find; isomorphic substitutions are common in naturally-occurring apatite. It is found in all rock types (especially metamorphic) and it also has biological importance as the main inorganic constituent of bone.

The unit cell of hydroxyapatite has a hexagonal crystal system denoted by $P6_3/m$. Unit cell parameters are a = 9.43 Å and c = 6.88 Å. Each unit cell has 6 equivalent phosphorous sites and 2 crystallographic sites for Ca, Ca(1) and Ca(2). Ca(1) has 4 atoms per unit cell and Ca(2) 6 atoms per unit cell (Monteil-Rivera, 2000; Fedoroff, 1999; McConnell, 1973). Fedoroff *et. al.* (1999) found that in HAP some Ca(2) sites are unoccupied, whereas, most Ca(1) are filled.

Figure 3.1 depicts a portion of the crystal lattice structure of fluoroapatite, hydroxyapatite and chloroapatite. It shows the location of the F⁻, OH⁻ and Cl⁻ groups in

the (c) unit cell axes, with intermittent mirror planes of Ca^{2+} in the (a) unit cell axes. It

also shows how the F ion is closer to the Ca ions and therefore more tightly bound than

OH⁻ or Cl⁻ (Posner, 1982). Figure 3.2 depicts the crystal structure of fluoroapatite; the

individual frames depict the location of calcium (Ca), phosphorous (P), oxygen (O) and

fluorine (F) in the structure.

Fluoroapatite   Hydroxyapatite   Chloroapatite
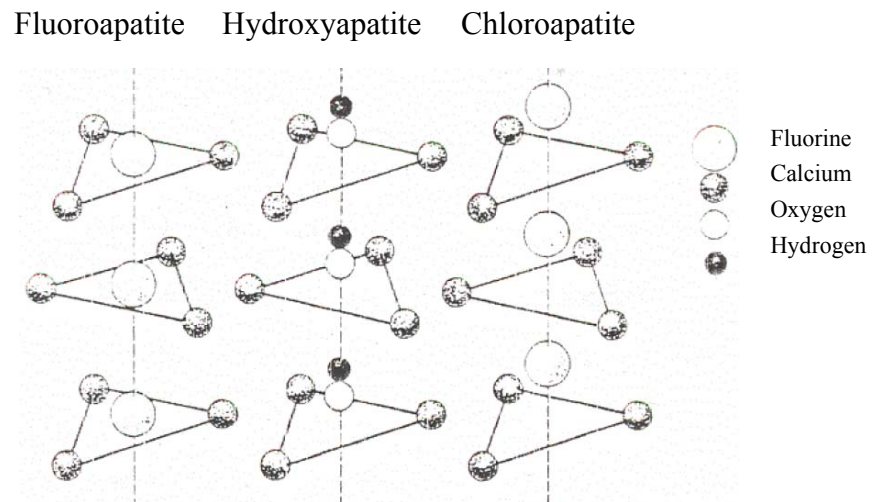
Figure 3.1: Atomic structure of Fluoroapatite, Hydroxyapatite, & Chloroapatite (Posner, 1982)
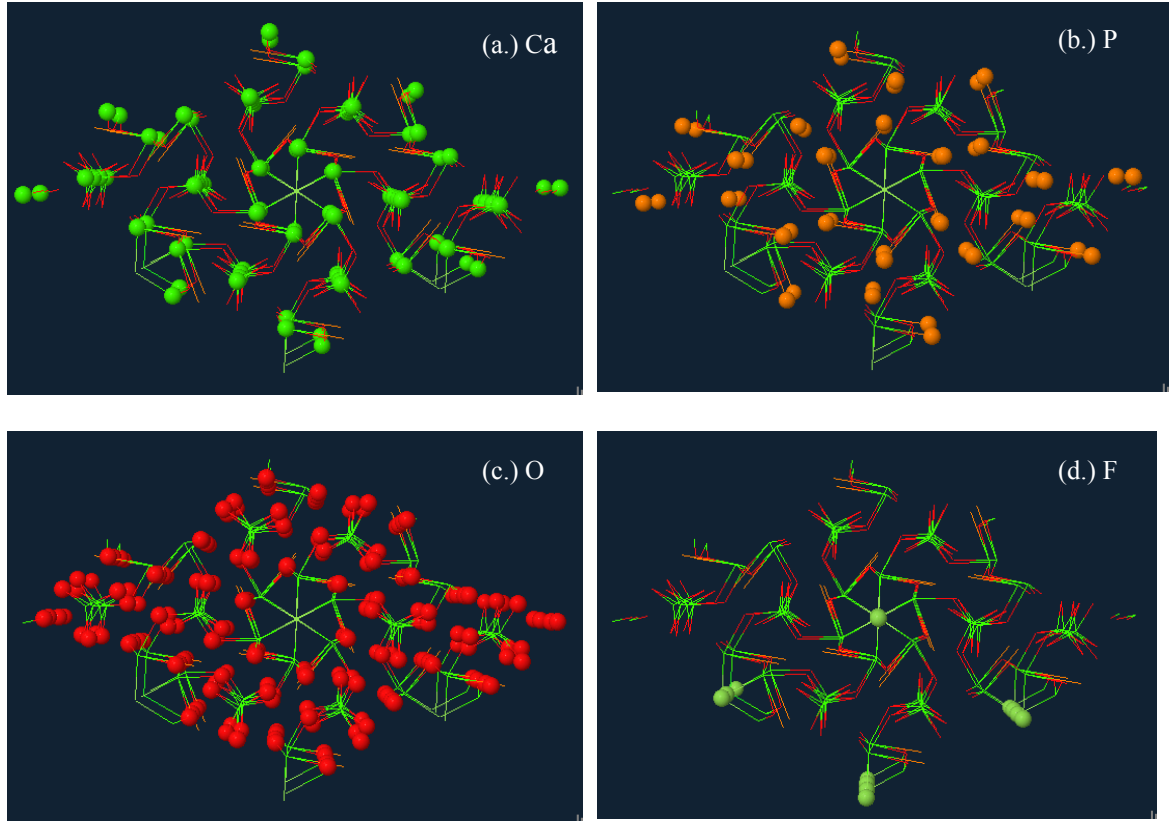
Figure 3.2: Crystal Structure of Fluoroapatite (a) displays Ca atoms, (b) P atoms, (c) O atoms and (d) F atoms.
(source: www.soils.wisc.edu/virtual_museum/fluorapatite/index.html)

3.3. Experimental Materials

All three apatites used in the experiments are high purity synthetic minerals. The hydroxyapatite, $Ca_5(PO_4)_3OH$, was purchased from Fischer Scientific, and the fluoroapatite, $Ca_5(PO_4)_3F$, and carbonate apatite, $Ca_5(PO_4,CO_3)_3(OH)$ were purchased from HiMed. The zinc solutions were prepared from its nitrate salt, $Zn(NO_3)_2 \cdot 6H_2O$, and sodium hydroxide (NaOH) and nitric acid (HNO_3) were used to adjust and control the pH. Table 3.1 lists several synthetic and natural occurring minerals that were used as reference standards.

Two co-precipitates were prepared in the lab by methods described in Jarcho *et. al.* (1976) and Ergun *et. al.* (2001). These samples were prepared to simulate a co-

precipitate in which Zn exchanges for Ca in the crystal structure. One co-precipitate was prepared to represent a high loading of Zn, $(Ca,Zn_4)(PO_4)_3OH$, and the other a low loading, $(Ca_4,Zn)(PO_4)_3OH$. Briefly, a 0.1 M $Ca(NO_3)_2$ solution was spiked with $Zn(NO_3)_2 \cdot 6H_2O$ at 4:1 and 1:4 molar ratios. The solution was adjusted to pH 11 using concentrated NaOH and then stirred vigorously at room temperature. A 0.6 M $(NH_4)HPO_4$ solution , also at pH 11, was added dropwise over 60 minutes till a milky, gelatinous solution formed. The solutions were then centrifuged, filtered with a 0.2μm cellulose acetate filter and the resulting solid was freeze-dried. XRD spectra of the resulting co-precipitates were collected to confirm the formation of a zinc-substituted hydroxyapatite; spectra are presented in Appendix C.

Table 3.1: Reference Standards. Naturally Occurring and Synthetic Minerals

Mineral	Formula	Source (cat. No.)
Hopeite	$Zn_3(PO_4)_2 \cdot 4H_2O$	Harvard University Mineralogical Museum (110695) Broken Hill Mine. Kabwe, Zambia
Scholzite	$CaZn_2(PO_4)_2 \cdot 2H_2O$	Harvard University Mineralogical Museum (134656) Reaphook Hill, South Australia
Faustite	$ZnAl_6(PO_4)_4(OH)_8 \cdot 4H_2O$	Harvard University Mineralogical Museum (134655) Copper King Mine. Eureka, Nevada
Spencerite	$Zn_4(PO_4)_2(OH)_2 \cdot 3H_2O$	Harvard University Mineralogical Museum (125139) Hudson Bay Mine, Salmo, British Colombia, Canada
Zinc phosphate	$Zn_3(PO_4)_2$	Sigma-Aldrich
Zinc Oxide	ZnO	Standard obtained at SPring8 facility.
Zinc carbonate	$ZnCO_3$	Fluka
Zinc carbonate hydroxide	$[ZnCO_3]_2 \cdot [Zn(OH)_2]_3$	Fluka
(2) Zn-Ca co-precipitates	$(CaZn)_5(PO_4)_3OH,$	Prepared in lab

CHAPTER 4

METHODS

A combination of batch tests and surface analyses were used to study mechanisms of zinc removal by apatite. Characterization of the pure apatite mineral, prior to sorption, was conducted with x-ray diffraction (XRD), scanning electron microscopy (SEM) and determination of particle size and surface area. Three main types of laboratory batch experiments using zinc and the apatite minerals were conducted: (i) the determination of the kinetic rates of removal, (ii) pH adsorption edge and (iii) sorption isotherm experiments. Sorption studies consisted of equilibrating Zn^{2+} with apatites at various loadings below and above the maximum sorptive capacity in order to characterize changes that occur in the crystalline structure over a broad range of Zn concentrations. Characterization of the Zn-sorbed apatite was carried out using a combination of surface analytical techniques, including surface spectroscopy and an analysis of the particle's surface charge, in an integrated approach to determine the molecular scale mechanisms of contaminant retention, including surface complexation, surface precipitation, and co-precipitation.

Analysis of the metals concentration in solution was conducted with inductively coupled plasma – optic emission spectroscopy (ICP). The ICP instrument utilized was a VISTA AX from VARIAN, located in Gregg Hall at the University of New Hampshire. The Vista version v1.3 software program was used for data collection.

4.1. Characterization of Minerals

4.1.a Particle Surface Area and Size

Brunauer, Emmett, and Teller (BET) nitrogen adsorption was used to determine the surface area of the three apatites. A Tristar 3000 from Micromeritics Instruments was utilized. The weighted samples were degassed for four hours at a temperature of 200°C. The temperature was subsequently lowered by immersion of the vessel into a bath of liquid nitrogen. The instrument then gases the sample vessel with 30% nitrogen and 70% helium gas and measures sorption of the gas as a function of pressure. Once equilibrium is reached, desorption is induced by heating the sample. The resulting sorption and desorption BET isotherm can then be used to determine surface area of the particles (www.micromeritics.com).

Particle size was determined using the ZetaSizer Nano ZS from Malvern Instruments. The analytical technique consists of shining a laser onto the particles (in an aqueous solution) and measuring the intensity of the scattered light. Movement of the particles, due to the Brownian motion, causes fluctuations in the intensity of the scattered light. Because large particles move slower than small particles, the fluctuations in intensity can be correlated to the size of the particle.

4.1.b Scanning Electron Microscope

Field emission scanning electron microscopy (FESEM) was employed to characterize the surface morphology of the apatites. An AMRAY 3300 FE (field emission electron source) was used; the microscope was run at 7 keV, with a working

distance of 6.7 mm and samples were plated with an Au/Pd coating. Micrographs were taken at several magnifications.

4.1.c   X-Ray Diffraction

X-Ray diffraction (XRD) was used to characterize the apatite minerals. XRD measurements were carried out with a Rigaku-Geigerflex goniometer using a CuKα radiation source (40 kV, 30 mA). Scans were conducted using a continuous scanning technique from 4 to 90° 2θ, a scan rate of step 1.8 degree/min and a step size of 0.1 s/step. A divergence slit of 1°, a scattering slit of 1°, a receiving slit (crystal) of 0.3° and a receiving slit (monochromator) of 0.6° were used. All measurements were performed with an elemental tungsten (W) addition as an internal standard. Data was collected using Datascan 3.1, a Materials Data Inc (MDI) product and the XRD spectra were analyzed using the Materials Data JADE 5 XRD pattern processing program. The software analyzes the data using a search and match method where the difractograms collected from the samples are compared to difractograms of pure material stored within a CD-ROM database from the International Centre for Diffraction Data (ICDD). When the program determines that a match has been made, it rates the match with a Figure of Merit (FOM) ranging from 1- 100. Only FOM < 15 were considered as likely matches.

4.2.   pH Adsorption Edge

Determination of the pH edge of zinc sorption onto the three apatites helped to determine the optimal pH under which the reaction occurs. The study of the pH adsorption edge is also important because it gives important information regarding the solubility of zinc by

analyzing aqueous Zn concentrations, $[Zn]_{aq}$, as a function of pH. This can provide insight on the speciation of Zn under experimental conditions, as well as the preferential precipitation of zinc minerals.

The pH edge experiments were conducted using an initial zinc solution of 4 x 10^{-4} mM, containing a 0.01 M KNO_3 background electrolyte. The Zn solution was prepared from its nitrate salt, $Zn(NO_3)_2 \cdot 6H_2O$. The samples contained 0.01 g apatite giving a Zn-loading of 40 μM Zn/g apatite. Nine 125 ml HDPE bottles containing 35 mL of solution were prepared with pHs ranging from 3 – 11. The pH was adjusted using HNO_3 or NaOH, and was measured using a Schott Titronic universal meter pH probe. Titration curves were carried out prior to the experiment to determine the amount of nitric acid and sodium hydroxide necessary to adjust the pH of the samples containing the zinc solution and apatite. The samples were equilibrated for 24 hours in a closed vessel that eliminated the presence of CO_2. They were tumbled in a motorized rotation device that turns end over end to allow for adequate mixing, and then filtered using disposable 0.2 μm cellulose acetate syringe filters. The total Zn concentration, $[Zn_T]_{aq}$, upon completion of sorption was analyzed with ICP.

Zinc solubility curves were modeled with Visual MINTEQ (ver. 2.3) to determine the Zn concentration and pH at which zinc minerals would precipitate from solution. The first three minerals predicted to precipitate were smithsonite, $ZnCO_3$, hydrozincite, $Zn_5(CO_3)_2(OH)_6$, and zinc oxide, ZnO. Hydrozincite is reported to be the most stable species in the natural environment (Zachara, 1989; Waychunas, 2002), whereas ZnO is the first to form when the system is not exposed to the atmosphere. This information was used in designing the experiments, in that the initial $[Zn]_{aq}$ at which the experiment was

conducted was below the Zn solubility curves, along the pH range studied (pH 3-11), to assure that removal of Zn from solution was due to sorption onto apatite and not precipitation from solution as one of the above-mentioned minerals.

4.3. Kinetic Rates of Removal

The kinetic rates of removal experiments measure sorption as a function of time in order to determine the time required for the reaction to reach equilibrium.

A mass of 10 mg of apatite was added to 35 mL of 5.32 x 10^{-4} mM Zn solution containing 0.01 M KNO_3 as a background electrolyte (Zn loading = 53.2 μM Zn/g apatite). Solutions were adjusted to pH 8 using 0.05 M NaOH. The experiments were conducted in 125 mL HDPE bottles and tumbled in the same motorized rotation device used for the pH edge experiment. The time periods sampled were: 10 min, 30 min, 60 min, 3 hrs, 6 hrs 12, hrs 24 hrs, 3 days and 7 days. Upon completion of the determined contact period the samples were filtered using a 0.2 μm cellulose acetate disposable syringe filter and the final Zn concentrations were measured with ICP.

As in the design of the pH edge experiments, the initial $[Zn]_{aq}$ solution was chosen based on Visual Minteq modeling of zinc solubility to assure that the solubility limit of zinc precipitates are not exceeded throughout the batch test.

4.4. Sorption Isotherm

In designing the sorption experiments it is desirable to conduct the tests at various loadings below and above the maximum sorptive capacity in order to characterize the behavior over a broad range of concentrations. Two different experimental approaches

were conducted to determine the sorption isotherms. The first group is the traditional method where the total amount of $[Zn]_{aq}$ is added in a single aliquot. In the second method aliquots are added in a step-wise manner in an attempt to maintain zinc below the solubility limit. This second method was employed to test the hypothesis that the availability of Zn^{2+} in solution has a direct impact on the amount and manner by which zinc is sorbed. These experiments will be referred to as the Traditional and Modified sorption isotherms, respectively.

4.4.a   Traditional Sorption Isotherm

The samples were placed in 125 mL HDPE bottles and tumbled in a motorized rotation device at room temperature. They had an initial volume of 100 mL to which 0.1 g of apatite was added. The initial $[Zn]_{aq}$ ranged from 0.006 – 2.0 mM, giving a Zn-loading of 0.06 – 20 mM Zn/g apatite. The pH was adjusted to pH 8 $\pm$ 0.3, using concentrated NaOH. After a 24-hour equilibration period approximately 15 mL of the sample was filtered with a 0.2 µm disposable syringe filters and analyzed with the ICP. The solid was recovered using a 0.2 µm filter and a vacuum filtration device and then freeze-dried. Freeze drying was conducted using a Freezone6 – Freeze Dry System from Labconco Corportation (Kansas City, Missouri), which removes moisture from the sample by creating a vacuum around the sample at low temperatures.

4.4.b   Modified Sorption Isotherm

A mass of 0.5 g of apatite was added to 1.0 L of deionized water. Zinc was added to the vessel from a concentrated solution of 115 mM Zn in aliquots of 0.01 mL every 5

minutes using an automatic titrator. Initial $[Zn]_{aq}$ ranged from 0.002 – 6.23 mM, giving

Zn-loadings ranging from 0.02 – 62.3 mM Zn/g apatite. Results from the kinetic

experiments indicated that the reaction occurs rapidly, which served as the basis for

selecting a 5-minute equilibration period. A stir bar was used to keep the solution well

mixed and pH was maintained at 8 using 0.5 M NaOH. Multiple samples were collected

from the vessel at various intervals (ranging from 1.3 hrs to 5 days) in order to determine

how the system assimilated the addition of Zn^{2+}. At each interval approximately 5 mL

samples were removed using a 0.2 μm syringe filter. In an effort to keep the total volume

at 1.0 L the ~5 mL of sample removed was replaced with 5 mL of deionized water. The

samples $[Zn]_T$ was measured with ICP.

4.5.   Zeta Potential

Zeta potential (ZP) measurements were conducted with a ZetaSizer Nano ZS and

analyzed using standard operating procedures provided in the accompanying Dispersion

Technology software, version 4.0.

In this research it was of interest to measure the surface charge (mV) of the

particle as a function of Zn^{2+} loading (mM Zn/g apatite). Changes in the surface charge

can provide important information regarding the interactions between the potential

determining ions present at the liquid-solid interface. Measurements were performed on

1.0 mL aliquots removed from the sorption isotherm batch tests at the same intervals the

sorption samples were removed. Efforts were made to not alter the solution when

sampling as disturbing the delicate environment surrounding the apatite particle would

have a direct effect on its surface charge.

Measurement of the zeta potential as a function of pH was used to determine the point of zero charge (PZC) of the particle. For this purpose, an MPT-2 Autotitrator from Malvern Instruments was used. The apatite sample (0.1 mg/mL), with no sorbed zinc, was titrated to pH 2 and 12 using 0.1 M HNO_3 and NaOH, respectively.

4.6. Spectroscopy

XAS and XPS were used to conduct a spectroscopic analysis of the zinc-sorbed minerals. The samples were prepared in the range between low surface loading at low solution concentration and high surface loading at high solution concentration. End members of this continuum, including natural apatites and possible Zn-Ca apatite minerals were also used. The apatite samples obtained from the sorption isotherm batch tests, after the apatite had been filtered and freeze dried, were a fine powder.

4.6.a <u>X-Ray Absorption Spectroscopy</u>

X-Ray adsorption spectroscopy (XAS) was conducted at two synchrotron facilities. XAS was collected at the Japan Synchrotron Radiation Research Institute (JASRI), Super Photon Ring 8GeV (SPring-8) BLO1B1 beam line and at the Advanced Photon Source (APS), Argonne National Laboratory synchrotron facility at the13-BM beam line while attending a XAS training course offered by the APS. Both facilities are third generation synchrotrons, with energy capacities of 8GeV and 7GeV, respectively, and as such offer cutting edge technology to gain insight into the crystal structure and atomic coordination of the zinc-sorbed apatite mineral.

In the SPring8 facility spectra was collected at the Zn K-edge using a Si (111) monochromator. The storage ring operated at 8 GeV and had an average current of 100 mA. The apatite samples were measured at room temperature in fluorescence mode with a 19 element Ge solid state detector positioned 45° to the incident beam and approximately 2 cm from the sample. The Zn standards were measured in transmission mode using ion chambers. The beam was calibrated with Cu foil to 8980 eV and the XAS data was collected at the Zn K – edge over the energy range of 9.16 – 11.18 keV. The powder apatite samples were made into pellets approximately 1 cm in diameter and 3 mm in thickness. The pellets were fixed onto Kapton tape, and placed on a slide mount for analysis. An approximately 1 x 1 cm window was cut out of one layer of Kapton tape to expose the sample.

At the APS facility spectra were also collected at the Zn K edge using a Si (111) monochromator. Depending on the Zn concentrations present in the sample the XAS spectra were collected in transmission mode or in fluorescence mode with a 13 element Ge detector at room temperature. The storage ring operated at 7 GeV and had an average current of 101.7 mA. The first peak in the derivative of the zinc spectrum was assigned an energy of 9,659 eV and data was collected from 9.56 to 10.3 keV. The powder samples were spread sparsely on tape and multiple layers of tape were placed atop each other.

The samples analyzed at the SPring8 facility included the pure apatite with no addition of Zn and Zn-loadings of 0.15 μM/g and 16 μM/g. The Zn-loadings were the same for all three apatites. The XAS spectra of all reference standards listed in Table 3.1 were also collected at SPring8. At the APS facility the samples analyzed included: 3.04 mM/g

HAP, 8.26 mM/g HAP, 4.48 mM/g CAP and 2.74 mM/g FAP, as well as $Zn_3(PO_4)_2$ and $ZnCO_3$ as reference standards.

Data analysis was conducted using the software program ATHENA, developed by Dr. Bruce Ravel and Dr. Matthew Newville (Ravel, 2005). It performs preliminary XAS data processing, including conversion of raw data to mu (E), background removal, alignment, merging, deglitching, Fourier transforms and plotting. Among ATHENA's main features is its ability to plot energy (E), photoelectron wavelength, (k) and the Fourier Transform (R), of individual and multiple spectra for XANES and EXAFS.

4.6.b   X-Ray Photoelectron Spectroscopy

The surfaces of zinc-sorbed apatite were examined using an AXIS HS spectrometer from Kratos Analytical, data was collected and processed using the VISION v. 2.0 software program (Casa Software Ltd. Wilmslow, Cheshire, UK). The instrument had been calibrated to 84 eV using the Au $4f_{7/2}$ photoelectron. The excitation source was a Mg K_α anode (1253.6 eV) and the aperture a Slot-M. A flood gun typically operating at -0.4 V was used as a charge neutralizer. The vacuum chamber operated at a pressure of around 10^{-8} Torr. A current of 10 mA was used. The powder samples were pressed onto copper tape, which was then placed on a stainless steel stub. The loading levels analyzed were: 0.93 mmol/g and 8.22 mmol/g for HAP, 0.99 mmol/g and 4.48 mmol/g for CAP, and 0.92 mmol/g and 2.74 mmol/g for FAP, as well as the pure apatites prior to Zn addition.

Low-resolution surveys were collected of each sample to obtain a general composition spectrum of the specimen. For the surveys, spectra were collected from 1200

to 0 eV, pass energy of 160 was used and the step size was of 1.0 eV with a 1000 ms dwell time. High-resolution spectra were collected for each element of interest; the photoelectron binding energies collected were: Ca $2p_{3/2}$, Ca $2p_{1/2}$, P $2p_{3/2}$, P $2s$, O $1s$, F $1s$, C $1s$ and Zn $2p$, as well as the Zn LMM auger line. A pass energy of 40 was used, with a step size of 0.1 eV and scan times ranging from 20 – 360 minute.

Charge referencing was conducted by ascribing the adventitious C 1s peak to a binding energy of 284.8 eV. Adventitious carbon is a ubiquitous substance that contaminates surfaces upon exposure to atmospheric air and/or by sample handling. Because it is found on most surfaces it has widespread use as an internal standard. CasaXPS was used for component curve fitting of the high-resolution photoelectron and auger lines. The program allows the user to select the peak region of interest, synthetic components are fit in this specified region and two fitting algorithms are available to optimize the parameters (Simplex and Marquardt). For the purposes of this research a Marquardt algorithm was used. Care was taken when fitting curves to maintain the full width half maximum (FWHM) values between 1.5 – 3.0 eV for most spectra. Touggard background subtraction was employed and an 80%Gaussian-20% Lorentzian line shape was used. Reference binding energy (BE) values were obtained from the NIST XPS Database 3.4 (http://srdata.nist.gov/xps/) and the literature (listed in appendix 1).

4.7. Visual Minteq

Visual MINTEQ is the windows version of the USEPA's MINTEQA2 code. It is a chemical equilibrium model used to calculate metal speciation and solubility equilibrium. To simulate the chemical environment of the experiments, the initial $[Zn]_{aq}$

used in each batch test was input into the program. A multi-problem sweep was conducted to determine changes in $[Zn]_{aq}$ as a function of pH. The simulations were run open to the atmosphere and oversaturated species were allowed to precipitate from the systems in order to predict what zinc minerals could potentially be forming. With each simulation the precipitation of one mineral dominated the Zn speciation. In order to identify other possible precipitates the given mineral was excluded from the system and the simulation was rerun under the same conditions. The program was then able to determine subsequent species that may precipitate.

5.5. Zeta Potential

Surface characterization of the apatites was carried out with the use of a Malvern Instruments Zeta Sizer - Nano Series zeta potential meter. Changes in the zeta potential can result from a combined effect of Zn^{2+} speciation, acid - base chemistry and the dominant potential determining ions present at liquid - solid interface. The relationship between pH and surface charge can be observed in figure 5.7 (a) HAP, (b) CAP and (c) FAP. The plots show that all three apatites have a predominantly negative surface charge throughout the pH range studied (3 -11). FAP exhibits a PZC at approximately pH 3. Both HAP and CAP maintained a negative surface charge throughout the pH range studied. Results from this study are below the PZCs reported in the literature, which range from 4 - 7.6 for hydroxyapatite and 4 to 8.5 for fluoroapatite (Wu, 1991).

According to the following acidity constants (Wu, 1991) the dominant phosphate species in the system would be HPO_4^{2-} and the dominant calcium species Ca^{2+}. Having a PZC at the low pHs observed in this study implies that throughout most of the pH range the dominant surface functional group is HPO_4^{2-}.

$$PO_4^{3-} + H^+ = HPO_4^{2-} \qquad \text{Log K} = 12.3 \qquad \text{eq. 5.1}$$
$$HPO_4^{2-} + H^+ = H_2PO_4^- \qquad \text{Log K} = 7.2 \qquad \text{eq. 5.2}$$
$$H_2PO_4^- + H^+ = H_3PO_4 \qquad \text{Log K} = 2.2 \qquad \text{eq. 5.3}$$
$$Ca^{2+} + H_2O = CaOH^+ + H^+ \qquad \text{Log K} = -12.9 \qquad \text{eq. 5.4}$$
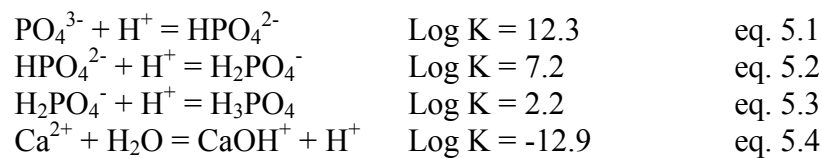
Figure 5.7 (c) shows results for the FAP experiment run with and without a background electrolyte, KNO_3. It can be observed that the presence of a background electrolyte does not have a significant effect on the relationship between zeta potential and pH in this experiment. This is consistent with Somasundaran *et. al.* (1984) where the presence of KNO_3 did not alter the isoelectric point of HAP.
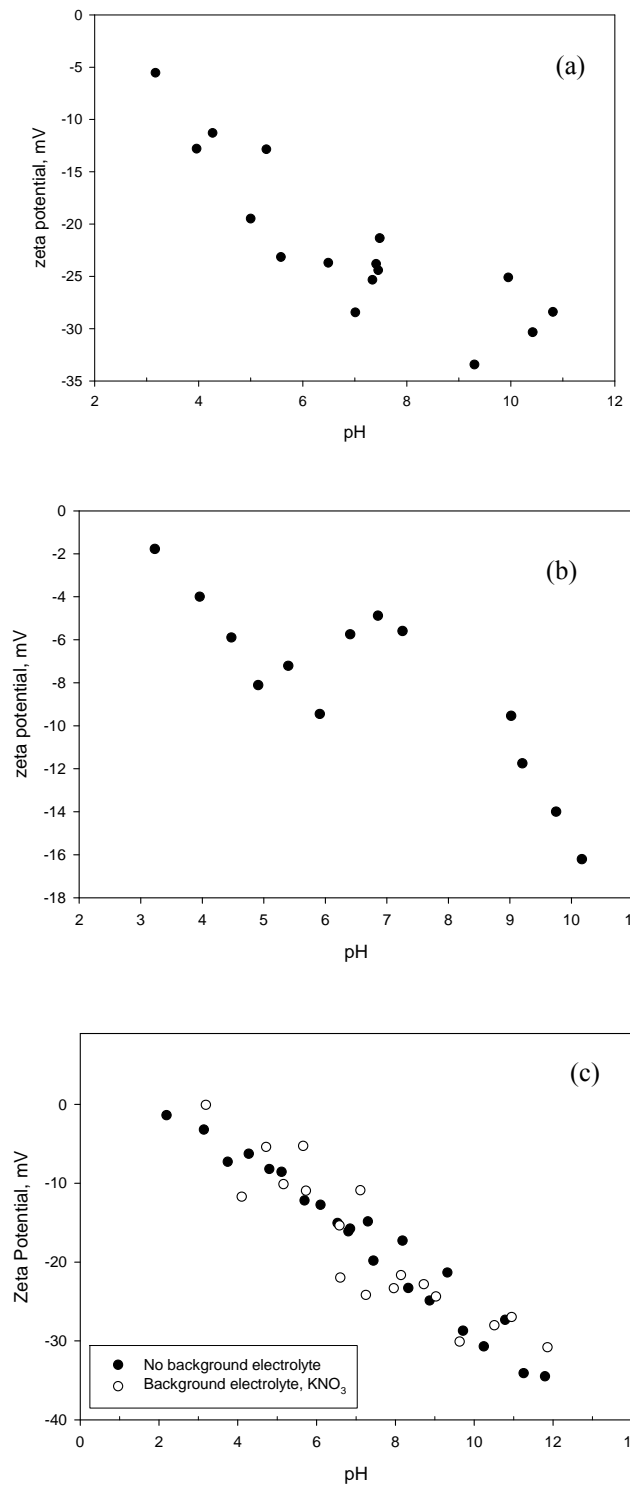
Figure 5.7: Point of Zero Charge for (a) HAP, (b) CAP and (c) FAP. Apatite=0.1 mg/mL

For the TSI experiments, the pH of all samples was adjusted to pH 8 ± 0.3, the sorption reaction was carried out for a 24 hour contact period and prior to filtration the zeta potential and pH of the samples was measured. This was done to study changes in the surface charge of the particle as a function of Zn^{2+} loading (mmol/g). Results are presented in figure 5.8 (a), (b) and (c).

In TSI-HAP and TSI-FAP it is possible to observe that at the lower contaminant loadings the surface charge rises at a higher rate of change than at the elevated loadings. A linear polynomial was fit to the two different regions. The two regions correspond to the portion in the BET isotherm attributed to complexation at lower loadings and the formation of a co-precipitate at higher loadings. Figure 5.8 specifies the slope (m) of each line fit, this is a measure of the rate of change and indicates that there are two distinct trends occurring in the different regions.

This behavior can be explained by considering that at low loading the surface of the particle responds dramatically to the increase of positively charged particles, Zn^{2+}. This would be characteristic of surface complexation. When the mechanism shifts to the formation of a co-precipitate the increased presence of ions does not have the same effect on the surface as the Zn^{2+} as the precipitate being formed has a neutral charge.

In TSI-CAP no evidence of co-precipitation was observed when fitting the BET isotherms (Fig. 5.6.b). Nevertheless, in Figure 5.8.b it is possible to observe that the rate of change in zeta potential as a function of Zn-loading does seem to shift from the low loading to the higher loadings.

The identification of two possible trends observed in Fig 5.8 (a) HAP and (c) FAP support the BET isotherm results for the TSI experiments (Fig 5.4 (a) and (c)) that

indicate a change in sorption mechanism occurs at approximately 3.3 ± 0.3 mmol/g for FAP, and between $1.32 - 3.4$ mmol/g for HAP. Results for CAP were more difficult to interpret, as co-precipitation was not identified in the TSI-BET isotherm (Fig. 5.6.b).
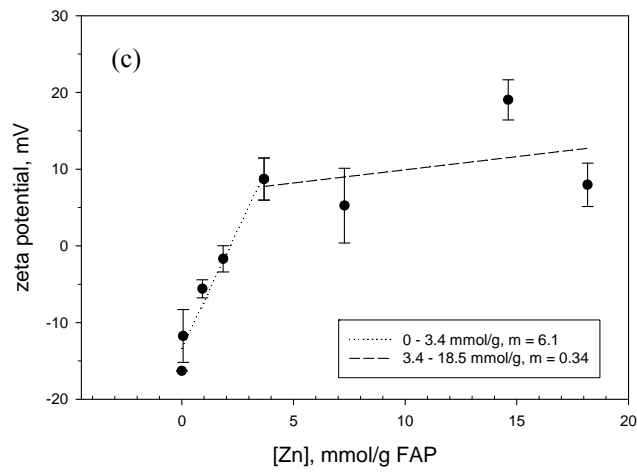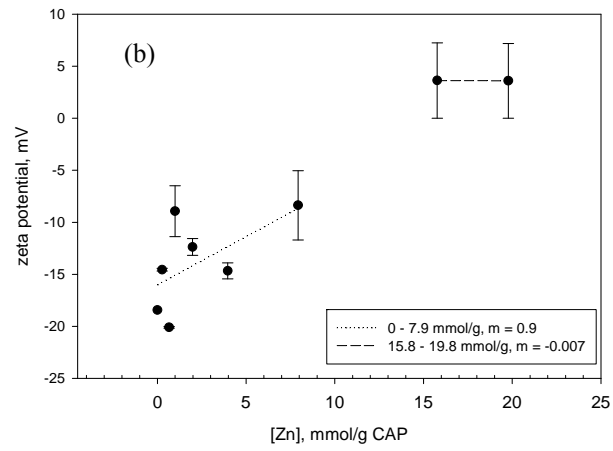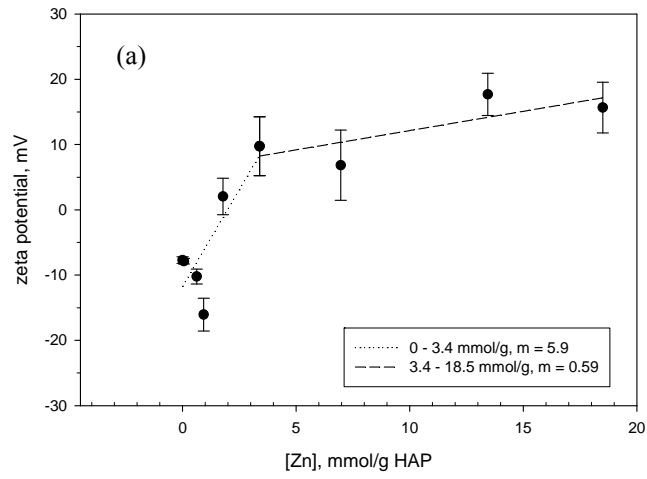
Figure 5.8: Zeta Potential vs. [Zn], mmol/g for (a) TSI-HAP, (b) TSI-CAP and (c) TSI-FAP. Initial $[Zn]_{aq} = 0.006 – 2.0$ mM. Apatite = 1.0 g /L.

5.6.   X-Ray Absorption Spectroscopy

Data analysis was conducted using the software program ATHENA, the following section discusses the spectra in terms of the plot energy (E), photoelectron wavelength (k), and the Fourier Transform (R), of individual and multiple spectra.

ATHENA was used to perform qualitative analysis of the XANES data. The multiple spectra of samples collected in fluorescence mode were calibrated individually and summed for analysis. Standard procedures were followed to remove background and normalize the XAFS data. For background removal a simple/linear polynomial was fitted to the spectrum below the edge and a quadratic polynomial for the post edge. The edge step is approximated by ATHENA and the spectrum is normalized by that value. The first inflection point in the edge region was used to determine the threshold energy (E_0), which was in turn used to convert the data to k-space, χ (k) was weighted by k^2 to emphasize the oscillations and was then Fourier Transformed.

For the present analysis the XAS spectra collected for each apatite sample was compared to Zn mineral standards also collected for this research. The figures presented in this section display the best fits between the Zn sorbed samples and the reference materials, as determined visually by overlaying the spectra. Appendix B includes the spectra of the Zn sorbed samples and the remaining reference standards specified in Table 3.1.

5.6.a   <u>Hydroxyapatite</u>

Figures 5.9 (a) – (f) compare the background-removed photoelectron wavelength, χ(k) and Fourier Transform, χ (R), of Zn-sorbed hydroxyapatite and three standards. Figure 5.9 (a) and (b) present χ(k) and χ (R) of the 0.0016 mmol/g HAP sample

compared to scholzite, $CaZn_2(PO_4)_2$. Figures (c) and (d) depict the 8.26 mmol/g HAP sample compared to zinc carbonate hydroxide, $[ZnCO_3]_2 \cdot [Zn(OH)_2]_3$. Figures (e) and (f) compare the high loading sample to ZnO; these plots illustrate the lack of fit that may be observed.
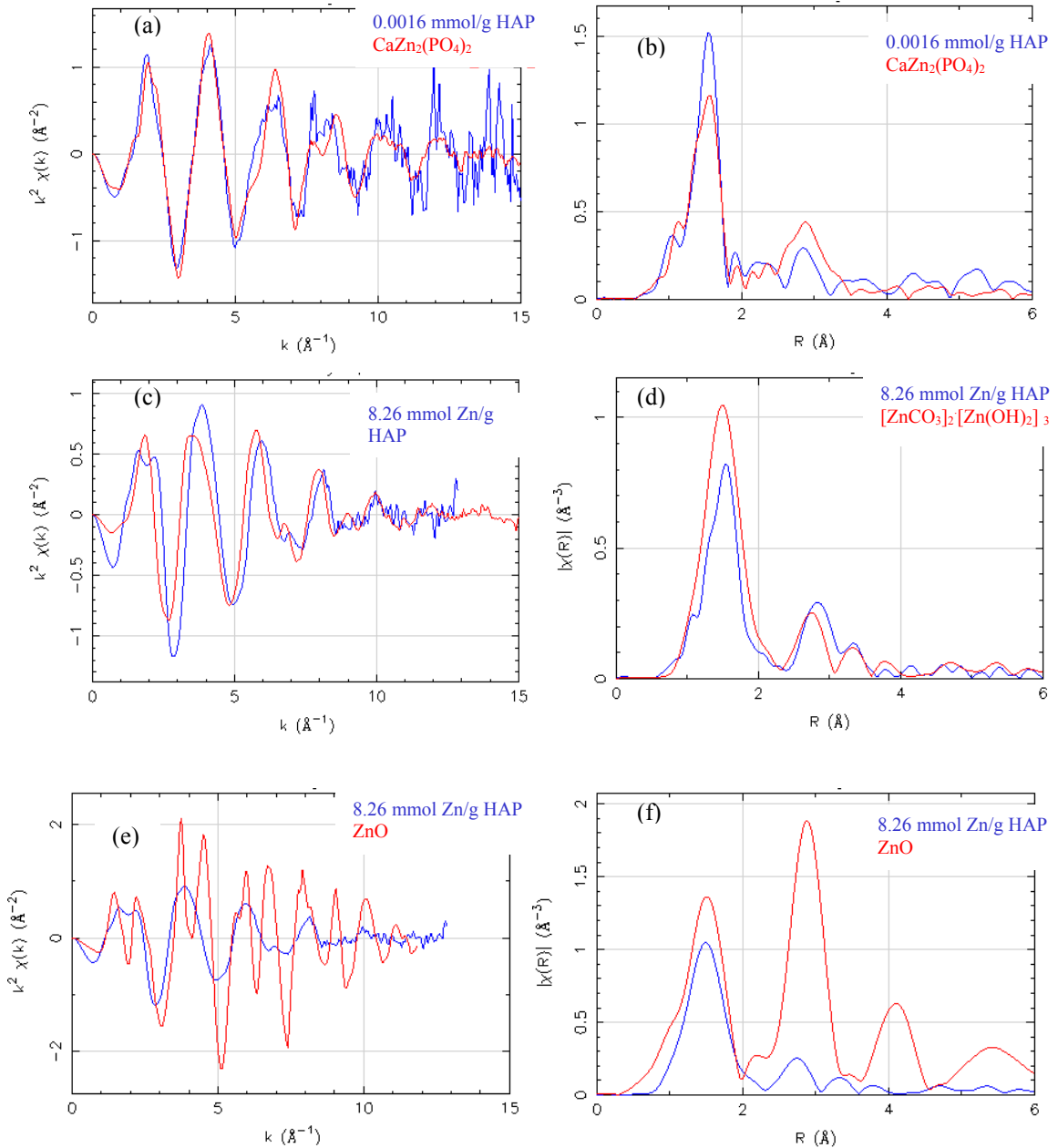
Figure 5.9: XAS spectra for HAP (a) $\chi(k)$ for 0.0016 mmol/g, (b) χ (R) for 0.0016 mmol/g, (c) $\chi(k)$ for 8.26 mmol/g, (d) χ (R) for 8.26 mmol/g, (e) $\chi(k)$ for 8.26 mmol/g and (f) χ (R) for 8.26 mmol/g.

5.6.b Carbonate Apatite

Figures 5.10 (a) – (d) compare the background removed photoelectron wavelength, χ (k) and Fourier Transform, χ (R), of Zn-sorbed hydroxyapatite and two standards. Figure 5.10 (a) and (b) presents χ (k) and χ (R) of CAP with a low loading of Zn (0.0016 mmol/g) compared to zinc phosphate ($Zn_3(PO_4)_2$). Figures (c) and (d) depict a CAP with high loading (4.48 mmol/g) compared to zinc carbonate hydroxide, $[ZnCO_3]\cdot[Zn(OH)_2]_3$.
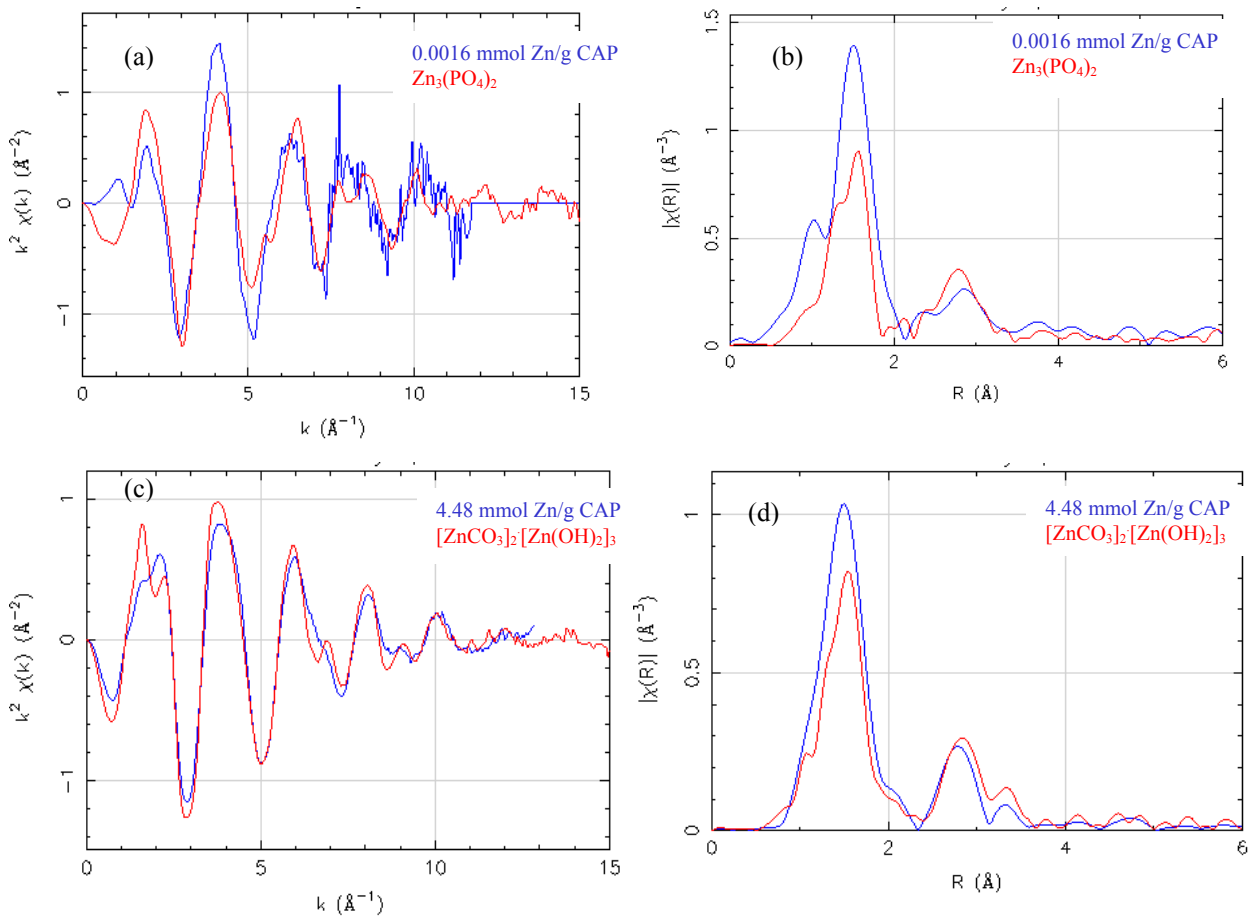
Figure 5.10: XAS spectra for CAP (a) χ(k) for 0.0016 mmol/g, (b) χ (R) for 0.0016 mmol/g, (c) χ(k) for 4.48 mmol/g and (d) χ (R)for 4.48 mmol/g.

5.6.c   <u>Fluoroapatite</u>

Figures 5.11 (a) – (f) compare the background removed photoelectron wavelength, χ(k) and Fourier Transform, χ (R), of Zn-sorbed FAP and three standards. Figure 5.11 (a) and (b) presents χ(k) and χ (R) of the FAP high loading (2.74 mmol/g) compared to the zinc co-precipitate prepared in the lab, $(Ca_4Zn)(PO_4)_2(OH)$. Figures (c) and (d) present the FAP high loading compared to both zinc carbonate hydroxide $([ZnCO_3]\cdot[Zn(OH)_2]_3)$ and zinc carbonate $(ZnCO_3)$.
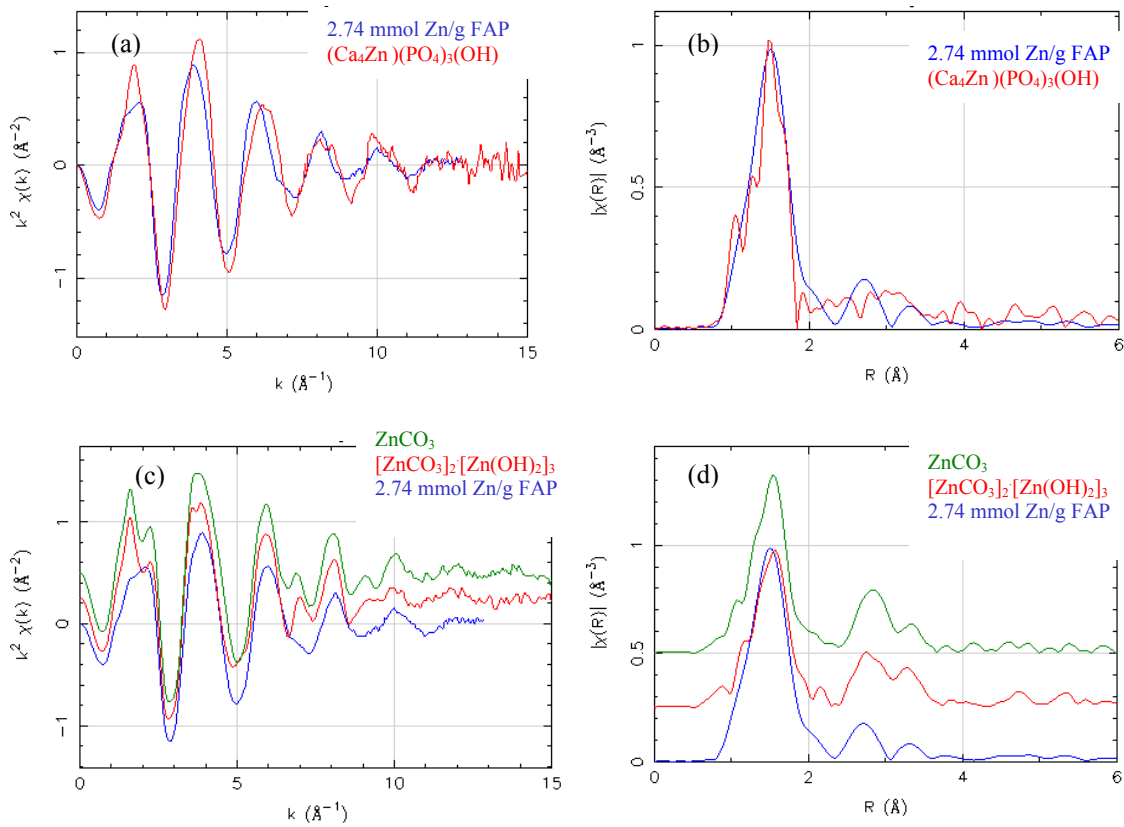
Figure 5.11: XAS spectra for FAP (a) χ(k) for 2.74 mmol/g, (b) χ (R) for 2.74 mmol/g, (c) χ(k) for 2.74 mmol/g and (d) χ (R)for 2.74 mmol/g.

In simple terms, the Fourier transform (FT), χ (R), is a mathematical interpretation of the scattering of x-rays by matter (Ramachandran, 1970) to describe its structure. The peaks in the FT may correspond to either a single shell orbital or a convolution of orbitals surrounding the absorbing atom (Zn). It can therefore provide a basic radial distribution of the molecule. Fourier transforms make it possible to compare nearest neighbor distances even without a rigorous physical and chemical interpretation of the spectral features.

The high loading samples of all three apatite presented strong similarities to the spectra of the synthetic mineral standard zinc carbonate hydroxide, $[ZnCO_3]_2 \cdot [Zn(OH)_2]_3$. The three main peaks of the standard material had matching peaks in the Zn-sorbed samples. The spectral match is supported by modeling results with Visual Minteq, which predicts that under the experimental conditions hydrozincite, $Zn_5(CO_3)_2(OH)_6$, is the dominant mineral species formed. This was also found to be the case by Lee *et. al.* (2005) and Fuller *et. al.* (2002), who determined that the combined effect of elevated contaminant level, alkaline pH and the presence of dissolved CO_3 favor the formation of hydrozincite and therefore interfere with the formation of a zinc-phosphate mineral.

The low loading samples of HAP and CAP had very similar spectral features to scholzite and hopeite, respectively. This presents strong evidence that the formation of a Zn-phosphate mineral occurs even when the dominant removal mechanism is surface complexation. In considering the possible formation of a Zn-phosphate mineral at low contaminant levels it is important to bear in mind that the BET isotherm model dictates that in multi-layer sorption the formation of a co-precipitate can begin to occur well before all surface sites are filled. Therefore the formation of a Zn-phosphate mineral at

the low Zn-loadings is not unreasonable. XAS low detection limit and ability to determine inter-atomic distances makes it ideal for the identification of a co-precipitate forming at trace levels. Both hopeite and scholzite have an orthorhombic unit cell so similarities in the spectral features could indicate that the structure of the co-precipitate being formed is characteristic of a Zn-phosphate mineral with an orthorhombic structure.

For the XAS spectra discussed above both the photoelectron wavelength, $\chi(k)$ and Fourier Transform, $\chi(R)$ plots gave good matches between the sample and mineral standards. Figure 5.11 (c) and (d) compares the $\chi(k)$ and $\chi(R)$ plots of 2.74 mmol/g FAP and the low loading co-precipitate prepared in the lab, $(Ca_4,Zn)(PO_4)_3OH$. In this case a good match is obtained for $\chi(k)$ but not for $\chi(R)$. This emphasizes that $\chi(k)$ and $\chi(R)$ give different information regarding the mineral structure and composition, and therefore similarities in both plots are important when doing qualitative comparison of XANES data.

5.7.   X-Ray Photoelectron Spectroscopy

In addition to the zinc-sorbed samples, spectra were collected for each apatite mineral prior to Zn^{2+} addition. This was done to both characterize the pure minerals as well as to assist in investigating changes in elemental speciation as a function of Zn^{2+} loading. To verify that the data obtained for the each apatite mineral was in accordance with published values a systematic analysis of the Ca 2p, P 2p and O 1s high-resolution spectra was conducted. First, the photoelectron lines of the pure apatite (Ca 2p, P 2p, O 1s and F 1s) were confirmed to be within the range of reported values ($\pm$ 0.3 eV). Although, no publication of CAP was found in the literature, the reported HAP and FAP

Ca 2p lines are within close proximity (347.7 - 347.8 eV) and therefore the Ca 2p line of CAP is expected to be within the same range. Once it was confirmed that the results for the pure minerals matched published values, the Ca 2p of the sorbed species were also compared and these too were observed to match published values. The same approach was used for the P 2p and O 1s lines. For each P 2p spectra only one synthetic component was fit between 133.5 - 133.8 eV, corresponding to the PO_4^{3-} ion. For the O 1s photoelectron lines the main (or sole) curve fit was determined to correspond to the PO_4^{3-} ion. It is important to note that the O 1s binding energies for phosphate, hydroxide and carbonate overlap from approximately 530.9 – 532 eV and therefore it is possible that the large peaks represents an overlap of the three species (Sugiyama, 2001; Zin, 2004). The high-resolution spectra for the Ca 2p, P 2p, P 2s, C1s, F1s peaks and general surveys can be found in appendix A.

Tables 5.5 –5.11 summarize the BE of the samples and reference materials. The tables facilitate the comparison of experimental results with published values and standards. The low loading sample of HAP is denoted as Zn - $Ca_5(PO_4)_3OH$ and the high loading as $(Ca,Zn)_5(PO_4)_3OH$, CAP and FAP are named similarly. The spectra of naturally occurring hopeite, $Zn_3(PO_4)_2$, and scholzite, $CaZn_2(PO_4)_6$, were used as zinc phosphate mineral standards, Figures 5.15 and 5.16.

Figures 5.12, 5.13 and 5.14 display the curves fit for the Zn 2p and Zn LMM lines of the zinc-substituted apatites. Each figure displays two apatite samples, one at a low loading level, representative of the sorption behavior described by the Langmuir model and one at a high loading level representative of sorption behavior where co-precipitation is expected to occur. The loading levels analyzed were: 0.93 mmol/g and 8.22 mmol/g for

HAP, 0.99 mmol/g and 4.48 mmol/g for CAP, and 0.92 mmol/g and 2.74 mmol/g for FAP.

For component peak assignment, two classes of matches were used. The term "likely" was used in cases where both the photoelectron (Zn 2p) and auger line (Zn LMM) identified the same Zn species. The term "possible" was used when only one line identified the potential Zn species. A margin of $\pm$ 0.3 eV was used when matching the BE's of peaks. In most cases more than one likely match was identified.

The XPS data was also compared with results from XAS. This provided additional information on which to base the assignment of likely (or possible) chemical speciation. Table 5.4 summarizes the results from both XAS and XPS.

The HAP low loading sample (0.93 mmol/g) identified a likely match to scholzite, hopeite (scholzite and hopeite are within 0.1 eV) and $Zn(OH)_2$. The high loading (8.22 mmol/g HAP) gave likely matches for hydrozincite, $Zn_5(CO_3)_2(OH)_6$ and $Zn(OH)_2$. The CAP low loading sample (0.99 mmol/g) identified a likely match for scholzite/hopeite and $Zn(OH)_2$. For the high loading (4.48 mmol/g CAP) there was a likely match to $Zn(OH)_2$ and a possible match to $Zn_5(CO_3)_2(OH)_6$. The FAP low loading sample (0.92 mmol/g) also had a likely match for scholzite/hopeite and $Zn(OH)_2$. The high loading sample (2.74 mmol/g FAP) identified $Zn(OH)_2$, $Zn_5(CO_3)_2(OH)_6$ and $ZnCO_3$ as likely matches.

Table 5.4: Summary of XAS and XPS Results

APATITE	XAS	XPS
HAP	0.0016 mmol/g: $CaZn_2(PO_4)_6$ 8.22 mmol/g: $[ZnCO_3]_2 \cdot [Zn(OH)_2]_3$	0.93 mmol/g: $CaZn_2(PO_4)_6$, $Zn_3(PO_4)_2$ or $Zn(OH)_2$ 8.22 mmol/g: $Zn_5(CO_3)_2(OH)_6$ or $Zn(OH)_2$
CAP	0.0016 mmol/g: $Zn_3(PO_4)_2$ (synthetic) 4.48 mmol/g: $[ZnCO_3]_2 \cdot [Zn(OH)_2]_3$	0.99 mmol/g: $CaZn_2(PO_4)_6$, $Zn_3(PO_4)_2$ or $Zn(OH)_2$ 4.48 mmol/g: $Zn_5(CO_3)_2(OH)_6$ or $Zn(OH)_2$
FAP	2.74 mmol/g: $(Ca_4,Zn)(PO_4)_3OH$ 2.74 mmol/g: $[ZnCO_3]_2 \cdot [Zn(OH)_2]_3$ or $ZnCO_3$	0.92 mmol/g: $CaZn_2(PO_4)_6$, $Zn_3(PO_4)_2$ or $Zn(OH)_2$ 2.74 mmol/g: $Zn_5(CO_3)_2(OH)_6$, $ZnCO_3$ or $Zn(OH)_2$

(a) Zn 2p for 0.93 mmol/g HAP

x 10¹

Name	Pos.	FWHM
Zn 2p	1022.12	2.612
Zn 2p	1045.70	1.862

CaZn2(PO4)6/Zn3(PO4)2
Zn(OH)2

Binding Energy (eV)

(b) Zn LMM for 0.93 mmol/g HAP

Name	Pos.	FWHM
Zn LMM	986.89	2.796
Zn LMM	989.81	2.703
Zn LMM	984.21	2.195

CaZn2(PO4)6/Zn3(PO4)2
Zn(OH)2

Kinetic Energy (eV)

(c) Zn 2p for 8.26 mmol/g HAP

x 10¹

Name	Pos.	FWHM
Zn 2p	1022.64	2.511
Zn 2p	1045.58	2.657

Zn5(CO3)2(OH)6
Zn(OH)2

Binding Energy (eV)

(d) Zn LMM for 8.26 mmol/g HAP

Name	Pos.	FWHM
Zn LMM	987.02	4.192
Zn LMM	990.56	2.912

Zn(OH)2
Zn5(CO3)2(OH)6

Kinetic Energy (eV)

Figure 5.12: XPS spectra for HAP (a) Zn 2p for 0.93 mmol/g, (b) Zn LMM for 0.93 mmol/g (c) Zn 2p for 8.22 mmol/g, and (d) Zn LMM for 8.22 mmol/g.
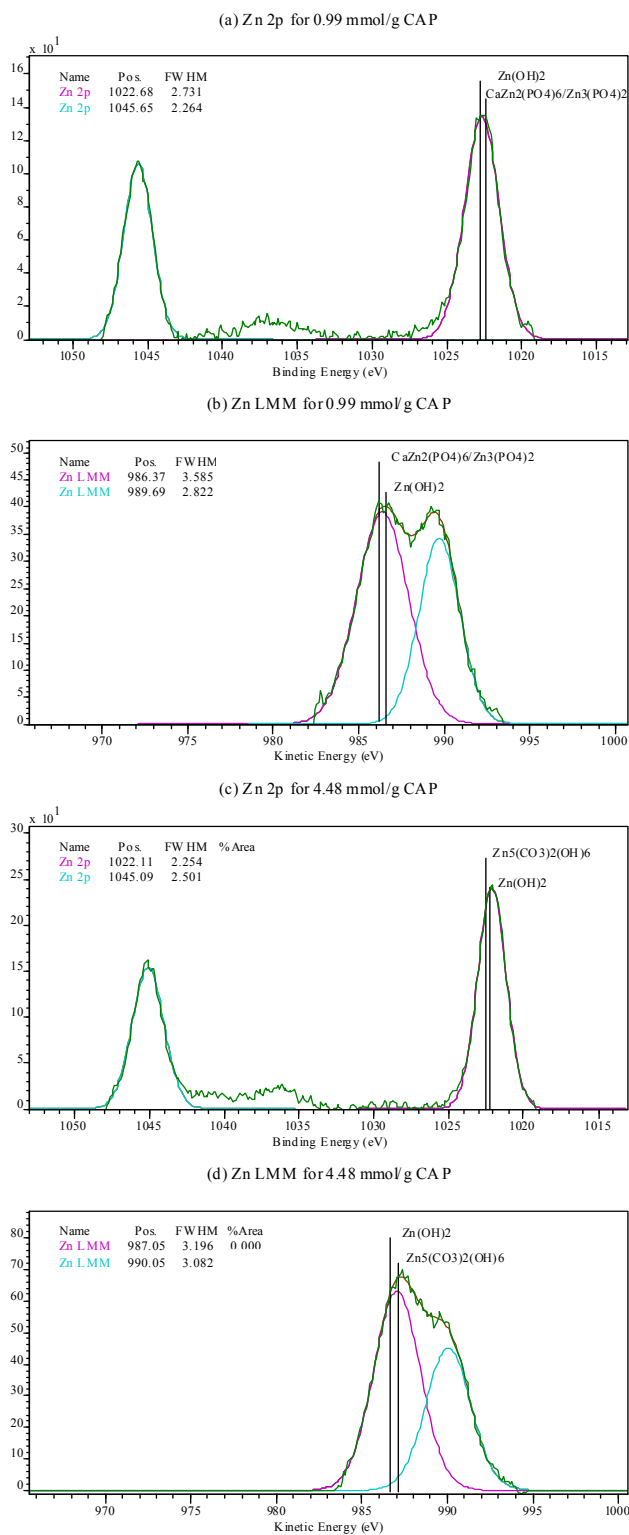
Figure 5.13: XPS spectra for CAP (a) Zn 2p for 0.99 mmol/g, (b) Zn LMM 0.99 mmol/g, (c) Zn 2p for 4.48 mmol/g and (d) Zn LMM for 4.48 mmol/g.

(a) Zn 2p for 0.92 mmol/g FAP

Name	Pos.	FWHM	%Area
Zn 2p	1045.76	1.994	29.057
Zn 2p	1022.77	2.969	70.943

Zn(OH)2
CaZn2(PO4)6/Zn3(PO4)2

Binding Energy (eV)

(b) Zn LMM for 0.92 mmol/g FAP

Name	Pos.	FWHM	%Area
Zn LMM	986.31	2.144	0.000
Zn LMM	988.91	2.988	0.000
Zn LMM	984.66	3.197	0.000

CaZn2(PO4)6/Zn3(PO4)2
Zn(OH)2

Kinetic Energy (eV)

(c) Zn 2p for 2.74 mmol/g FAP

Name	Pos.	FWHM	%Area
Zn 2p	1022.33	2.499	61.105
Zn 2p	1045.38	2.585	38.895

Zn(OH)2/Zn(CO3)
Zn5(CO3)2(OH)6

Binding Energy (eV)

(d) Zn LMM for 2.74 mmol/g FAP

Name	Pos.	FWHM	%Area
Zn LMM	986.98	3.778	0.000
Zn LMM	990.38	2.910	0.000

Zn(OH)2/Zn(CO3)
Zn5(CO3)2(OH)6

Kinetic Energy (eV)

Figure 5.14: XPS spectra for FAP (a) Zn 2p for 0.93 mmol/g, (b) Zn LMM for 0.93 mmol/g, (c) Zn 2p for 2.74 mmol/g and (d) Zn LMM 2.74 mmol/g.

(a) Zn 2p - Hopeite

Name	Pos.	FWHM
Zn 2p	1022.47	2.991
Zn 2p	1045.75	4.752

(b) Zn LMM - Hopeite

Name	Pos.	FWHM
Zn LMM	986.33	2.967
Zn LMM	989.52	3.016
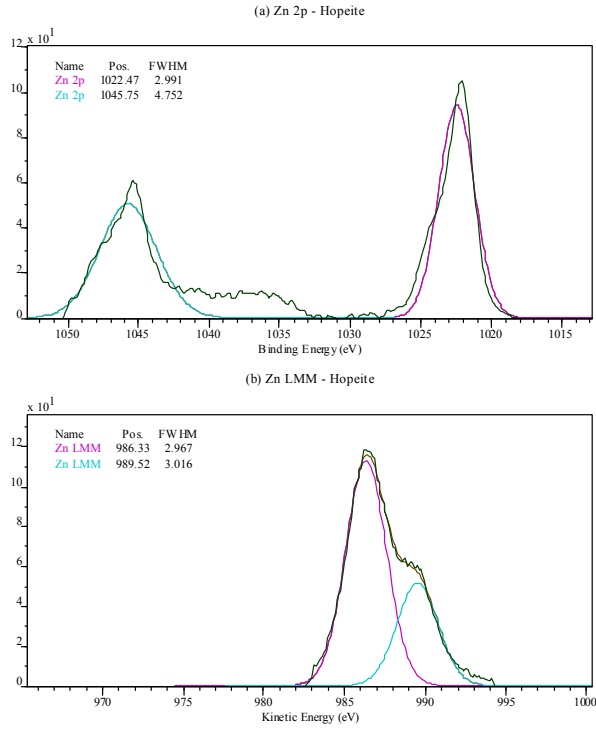
Figure 5.15: (a) Zn 2p and (b) Zn LMM spectra for Hopeite, $Zn_3(PO_4)_2$

(a) Zn 2p - Scholzite

Name	Pos.	FWHM
Zn 2p	1022.40	2.184
Zn 2p	1045.29	2.363

(b) Zn LMM - Scholzite

Name	Pos.	FWHM
Zn LMM	986.52	3.311
Zn LMM	989.82	2.536
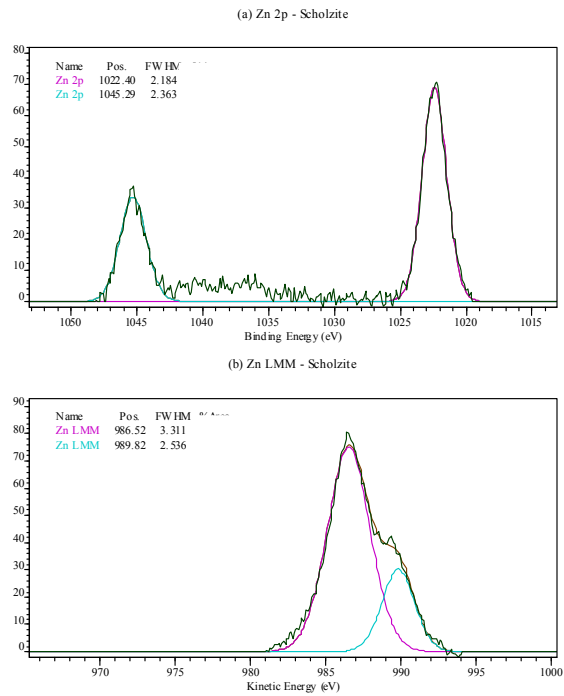
Figure 5.16: (a) Zn 2p and (b) Zn LMM spectra for Scholzite, $CaZn_2(PO_4)_2$

Table 5.5: Zn 2p — Binding Energy, eV

Type	Mineral	1021.1	1021.2	1021.3	1021.4	1021.5	1021.6	1021.7	1021.8	1021.9	1022.0	1022.1	1022.2	1022.3	1022.4	1022.5	1022.6	1022.7	1023.9	1024.0	1024.1	1024.2	1024.3	1024.4	1024.5	1024.6	1024.7	1024.8
Lit	$Zn(OH)_2$													■	----	----	----	■										
Lit	ZnO		■	----	■	■	■	■	■	■	■	■	----	■	----	----	----	■										
Lit	$ZnCO_3$															■												
Lit	$Zn_5(CO_3)_2(OH)_6$				■	----	■											■										
Lit	$Zn_3(PO_4)_2$																											■
Std	$Zn_3(PO_4)_2$																■											
Std	$CaZn_2(PO_4)_6$														■													
Sample	$Zn - Ca_5(PO_4)_3OH$													■														
Sample	$(Ca,Zn)_5(PO_4)_3OH$																■											
Sample	$Zn - Ca_5(PO_4,CO_3)_3OH$																	■										
Sample	$(Ca,Zn)_5(PO_4,CO_3)_3OH$													■														
Sample	$Zn - Ca_5(PO_4)_3F$																	■										
Sample	$(Ca,Zn)_5(PO_4)_3F$															■												

Table 5.6: Zn LMM		Kinetic Energy, eV																						
Type	**Mineral**	986.1	986.2	986.3	986.4	986.5	986.6	987.0	987.1	987.2	987.3	987.4	987.5	987.6	987.7	987.8	987.9	988.0	988.1	988.2	988.3	988.4	988.5
Lit	$Zn(OH)_2$					▬	▬			▬					▬								
Lit	ZnO																			▬			▬
Lit	$ZnCO_3$											▬											
Lit	$Zn_5(CO_3)_2(OH)_6$								▬									▬					
Std	$Zn_3(PO_4)_2$			▬																			
Std	$CaZn_2(PO_4)_6$				▬																		
Sample	$Zn\text{-}Ca_5(PO_4)_3OH$							▬															
Sample	$(Ca,Zn)_5(PO_4)_3OH$							▬															
Sample	$Zn\text{-}Ca_5(PO_4,CO_3)_3OH$				▬																		
Sample	$(Ca,Zn)_5(PO_4,CO_3)_3OH$							▬															
Sample	$Zn\text{-}Ca_5(PO_4)_3F$			▬																			
Sample	$(Ca,Zn)_5(PO_4)_3F$							▬															

Table 5.7: P 2p

Type	Mineral	Binding Energy, eV																						
		132.1	132.2	132.3	132.4	132.5	132.6	132.7	132.8	132.9	133.0	133.1	133.2	133.3	133.4	133.5	133.6	133.7	133.8	133.9	134.0	134.1	134.2	134.3
Lit	$Ca_5(PO_4)_3OH$								█	----	----	----	█	----	----	----	----	----	█					
Lit	$Ca_5(PO_4)_3F$																	█						
Lit	$Ca(H_2PO_4)_2 \cdot H_2O$																							█
Lit	phosphate		█	█	█	█	█																	
Lit	$Zn_3(PO_4)_2$																█							
Std	$Zn_3(PO_4)_2$																					█		
Std	$CaZn_2(PO_4)_6$																				█			
Sample	$Ca_5(PO_4)_3OH$																█							
Sample	$Zn - Ca_5(PO_4)_3OH$															█								
Sample	$(Ca,Zn)_5(PO_4)_3OH$															█								
Sample	$Ca_5(PO_4,CO_3)_3OH$																█							
Sample	$Zn - Ca_5(PO_4,CO_3)_3OH$																	█						
Sample	$(Ca,Zn)_5(PO_4,CO_3)_3OH$																█							
Sample	$Ca_5(PO_4)_3F$																█							
Sample	$Zn - Ca_5(PO_4)_3F$																	█						
Sample	$(Ca,Zn)_5(PO_4)_3F$																	█						

Table 5.8: Ca 2p — Binding Energy, eV

Type	Mineral	347.1	347.2	347.3	347.4	347.5	347.6	347.7	347.8	347.9
Lit	$Ca_5(PO_4)_3OH$	■	----	----	■	----	----	----	■	
Lit	$Ca_5(PO_4)_3F$					■				
Std	$CaZn_2(PO_4)_6$									■
Sample	$Ca_5(PO_4)_3OH$				■					
Sample	$Zn - Ca_5(PO_4)_3OH$					■				
Sample	$(Ca,Zn)_5(PO_4)_3OH$		■							
Sample	$Ca_5(PO_4,CO_3)_3OH$				■					
Sample	$Zn - Ca_5(PO_4,CO_3)_3OH$				■					
Sample	$(Ca,Zn)_5(PO_4,CO_3)_3OH$				■					
Sample	$Ca_5(PO_4)_3F$					■				
Sample	$Zn - Ca_5(PO_4)_3F$						■			
Sample	$(Ca,Zn)_5(PO_4)_3F$					■				

Table 5.9: F 1s — BINDING ENERGY, EV

Type	Mineral	684.0	684.1	684.2	684.3	684.4	684.5	684.6	684.7	684.8	684.9
Lit	$Ca_5(PO_4)_3F$							■			
Sample	$Ca_5(PO_4)_3F$						■				
Sample	$Zn - Ca_5(PO_4)_3F$					NP					
Sample	$(Ca,Zn)_5(PO_4)_3F$						■				

*NP: No

Table 6.0: O 1s — Binding Energy, eV

Type	Mineral	530.4	530.5	530.6	530.7	530.8	530.9	531.0	531.1	531.2	531.3	531.4	531.5	531.6	531.7	531.8	531.9	532.0	532.1	532.2	532.3	532.4	532.5	532.6
Lit	$Ca_5(PO_4)_3OH$								██	----	----	----	----	----	----	██								
Lit	$Ca_5(PO_4)_3F$											██												
Lit	ZnO	██	██	██	██	██	██																	
Lit	$Zn_3(PO_4)_2$																							
Lit	carbonate														██	██	██	██	██	██	██	██	██	
Lit	phosphate	██	██	██	██	██	██	██	██	██	██	██	██	██	██	██	██	██	██	██	██	██	██	██
Lit	hydroxide						██	██	██	██	██	██	██	██	██	██	██	██	██	██	██	██	██	██
Lit	H_2O																							
Std	$Zn_3(PO_4)_2$																	██						
Std	$CaZn_2(PO_4)_6$													██										
Sample	$Ca_5(PO_4)_3OH$								██															
Sample	Zn - $Ca_5(PO_4)_3OH$										██													
Sample	$(Ca,Zn)_5(PO_4)_3OH$							██						▓										
Sample	$Ca_5(PO_4,CO_3)_3OH$								██															
Sample	Zn - $Ca_5(PO_4,CO_3)_3OH$									██														
Sample	$(Ca,Zn)_5(PO_4,CO_3)_3OH$											██				██								
Sample	$Ca_5(PO_4)_3F$											██												
Sample	Zn - $Ca_5(PO_4)_3F$													██										
Sample	$(Ca,Zn)_5(PO_4)_3F$							██																

78

Table 6.1: C 1s		Binding Energy, eV															
Type	Mineral	281.5	281.6	281.7	281.8	281.9	282.0	282.1	282.2	288.7	288.8	288.9	289.0	289.1	291.4	291.5
Lit	$Zn_5(CO_3)_2(OH)_6$													█		
Lit	carbonates									█	█	█	█	█	█	█
Std	$Zn_3(PO_4)_2$	█			▦											
Std	$CaZn_2(PO_4)_6$															
Sample	$Ca_5(PO_4)_3OH$					█	█									
Sample	$Zn - Ca_5(PO_4)_3OH$		█					▦								
Sample	$(Ca,Zn)_5(PO_4)_3OH$															
Sample	$Ca_5(PO_4,CO_3)_3OH$							█								
Sample	$Zn - Ca_5(PO_4,CO_3)_3OH$					▦										
Sample	$(Ca,Zn)_5(PO_4,CO_3)_3OH$				▦											
Sample	$Ca_5(PO_4)_3F$		█													
Sample	$Zn - Ca_5(PO_4)_3F$				█	▦										
Sample	$(Ca,Zn)_5(PO_4)_3F$				█											

5.3.   Visual Minteq

The chemical speciation of the system was modeled with Visual Minteq. In the low loading-HAP scenario approximately 1.8×10^{-5} M of hydrozincite (0.015 g/L) are predicted to form (with no mineral species excluded from being allowed to precipitate). Under the high loading scenario hydrozincite is predicted to be the main mineral species to be present, approximately 1.62×10^{-3} M (1.39 g/L). The latter is above the instrument detection limit of XPS (1000 ppm) and can be readily detected. Therefore the simulations run with Visual Minteq are in agreement with the qualitative elemental speciation identified by XAS and XPS.

CHAPTER 6

CONCLUSIONS

Sorption of heavy metals and radionuclides onto apatite has been well demonstrated (Lee, 2005; Perrone, 2001; Chen 1997; Xu, 1994; Peld, 2004; Fuller, 2002). However, the exact molecular scale mechanism of removal from solution is not entirely understood. This research sought to investigate the molecular scale sorption mechanism using a combination of methods, including batch tests and surface analytical techniques, to study how Zn^{2+} is sequestered by apatite. The overall scope of the project was to study the sorption mechanism in order to assess the environmental viability of an apatite - PRB in a recycled materials beneficial use application in highways.

Results from the kinetic experiment show that the removal of $[Zn]_{aq}$ from solution occurs rapidly (< 60 min). This emphasizes that the reaction occurs readily and is thermodynamically favorable.

Isotherms measure sorption in terms of solute remaining in solution after contact with the sorbent. However, as discussed previously problems arise with this method when the solubility of Zn-mineral species is exceeded and the minerals precipitate from solution, making them unavailable to sorb onto apatite. It was first necessary to ensure that removal of Zn^{2+} from the solution occurred as sorption onto apatite and not simply as the formation of precipitates, namely carbonate, oxide and hydroxide precipitates. The pH adsorption edge was conducted below the solubility limit of hydrozincite $(Zn_5(CO_3)_6(OH)_6)$, smithsonite $(ZnCO_3)$ and zincite (ZnO), as predicted by Visual

Minteq. Results demonstrate that a dramatic decrease in $[Zn]_{aq}$ occurs well below concentration at which the above-mentioned minerals would fall out of solution and therefore removal of Zn^{2+} from solution can be attributed to sorption onto apatite and not the precipitation of Zn hydroxides, carbonates and/or oxides.

At low $[Zn]_{aq}$ sorption behavior follows the Langmuir isotherm. The formation of a co-precipitate and in turn a pure precipitate is evidenced in the BET isotherms, Figures 5.3 and 5.4. The BET isotherms suggest that the dominant sorption mechanism shifts from surface complexation to precipitation. However, because in multilayer sorption co-precipitation can begin to occur before all surface sites of the monolayer are filled it is difficult to accurately state when co-precipitation begins.

Results from the zeta potential analysis, support the argument that there is a shift in the mechanism by which Zn^{2+} is removed from solution. At low concentrations the surface charge changes rapidly with the addition of Zn^{2+} ions. This would be characteristic of a surface complexation reaction where the ions remain at the solid-liquid interface and thus have a strong influence on the zeta potential. At high concentrations (> 1. 32 mmol Zn/g Apatite) the further addition of positively charged ions does not appear to affect the surface charge as dramatically. This could be attributed to the incorporation of Zn^{2+} into a co-precipitate that has a neutral surface charge.

The batch experiments provide information regarding the sorption mechanism in terms of changes in $[Zn]_{aq}$ before and after the reaction. However they do not provide information on the mineral composition of the resulting Zn-sorbed apatite. X-ray spectroscopy was used to study the surface characteristics and composition of the minerals. By analyzing the minerals at various loading levels, as well as prior to Zn^{2+}

addition, it was possible to study the solid phase that results from the sorption experiments.

X-ray photoelectron spectroscopy was used to probe the surface chemistry of the apatite; curve fitting of the sample spectra made it possible to characterize the evolution in chemical state as a function of Zn^{2+} loading. The XAS analysis consisted primarily of a qualitative analysis of the x-ray absorption near edge (XANES) portion of the spectra and its Fourier transform (FT). It served to identify similarities in the local geometry around the sorbing atoms (Zn), especially the inter-atomic distances between Zn-O. Results from both techniques are compared in Table 5.4.

The most striking results from these spectroscopic analyses are the identification of Zn-phosphate minerals at very low Zn^{2+} loadings. The XAS spectra identified strong similarities to scholzite at 0.0016 mmol/g HAP and to synthetic zinc phosphate also at 0.0016 mmol/g CAP. Although these concentrations are orders of magnitude below the solubility product of Zn-phosphate minerals possible dissolution-precipitation reactions could account for the formation of these minerals. The phosphate ions released as a result of apatite dissolution are available to react with the Zn^{2+} ions present at the solid-liquid interface even at low $[Zn]_{aq}$.

XPS also identified scholzite and hopeite (as well as zinc hydroxide) as likely species present at the particle surface at relatively low Zn^{2+} loadings (0.92 - 0.99 mmol/g). These Zn^{2+} loadings correspond to the portion of the BET isotherm where sorption begins to level off prior to the dramatic increase characteristic of a precipitation reaction. At this Zn-loading it is very probable that dissolution-precipitation reactions would account for the formation of a Zn-phosphate solid solution and indicates that co-

precipitation begins to occur well before the maximum sorption capacity, q_{max}, predicted by the Langmuir isotherm.

At the elevated Zn^{2+} loadings of all three apatites, 8.22 mmol/g HAP, 4.48 mmol/g CAP and 2.74 mmol/g FAP, XAS identified the presence of hydrozincite, $(Zn_5(CO_3)_2(OH)_6)$ and XPS identified the presence of zinc carbonate hydroxide, $[ZnCO_3]_2 \cdot [Zn(OH)_2]$. Zinc carbonate hydroxide is a synthetic mineral with the same stoichiometric composition as naturally occurring hydrozincite. Hydrozincite is reported to be the most stable species of Zn under atmospheric $[CO_2]$ (Zachara, 1998) and when modeling the system in Visual Minteq it is the first mineral predicted to precipitate. Therefore, the evidence for the formation of hydrozincite under the given experimental conditions is strong. The formation of a zinc carbonate hydroxide implies that dissolved CO_3 plays an important role in the complexation of Zn^{2+}. The more soluble metal carbonate complexes dominate the speciation of Zn^{2+} thus interfering with the formation of Zn-phosphate minerals (K_{sp} = -10.26 for $ZnCO_3$, -35.3 for hopeite and -34.1 for scholzite). This is in agreement with the findings of Lee et al 2005 and Fuller et al 2003. Although the formation of hydrozincite dominates the Zn speciation at elevated concentrations it does not exclude the possibility of formation of Zn-phosphate minerals identified at the lower concentration. It simply emphasize that hydrozincite is present in much larger concentrations and dominates the system.

BIBLIOGRAPHY

Baillez, S; Nzihou, A; Beche, E; Flamant, G. "Removal of Lead (Pb) by Hydroxyapatite Sorbent". *Process Safety and Environmental Protection*. 82 (B2). 175-180 (2004).

Benjamin, M. Water Chemistry. McGraw Hill (2002).

Biji, A; Falini, G; Foresti, E; Gazzano, M; Ripamonti, A; Roveri, N. *Journal of Inorganic Biochemistry*. 49 (1993) 69-78.

Chen, X; Wright, J; Conca, J; Peurrung, L. "Effects of pH on Heavy Metal Sorption on Mineral Apatite". *Environmental Science & Technology*, 31 (1997) 624-631.

Cao, X; Ma, L.Q; Chen, M; Hardison, D; Harris, W. "Weathering of Lead Bullets and Their Environmental Effects at Outdoor Shooting Ranges." *Journal of Environmental Quality*. 32 (2003) 526-534.

Conca, J; Wright, J; Triay, I. "PIMS: A Technology for clean-up of Heavy metals and Radionuclides Throughout the World". *Reprinted from the Proceedings of the NATO Advanced Research Workshop*. Krakow, Poland. (1998).

Conca, J; Lu, N; Parker, G; Moore, B; Adams, A; Wright, J; Heller, P. "PIMS – Remediation of Metal Contaminated Waters and Soils". *Proceedings of the Second International Conference on Remediation of Chlorinated and Recalcitrant Compounds*. (2000)

Davies, N; Taylor, M; Simkiss, K. "The Influence of Particle Surface Characteristics on Pollutant Metal Uptake by Cells". *Environmental Pollution.* Vol 96 (2) (1997), 179-184.

Dzombak, D; Morel, F. *Surface Complexation Modeling. Hydrous Ferric Oxide*. Wiley-Interscience Publication (1990).

Eighmy, T; Kinner, A; Shaw, E; Dykstra E; Francis, C. "Hydroxylapatite (Ca5(PO4)3OH) Characterization by XPS: An Environmentally Important Secondary Mineral". Surface Science Spectra, vol 6 (3), (1999) 193-201.

Eighmy, T; Eusden, J.D. "Phosphate Stabilization of MSW Combustion Residues: Geochemical Principles". (unpublished)

Ergun, C; Webster, T.J.; Bizios, R; Doremus, R.H. "Hydroxylapatite with Substituted Magnesium, Zinc, Cadmium and Yttrium. I. Structure and Microstructure". *Journal of Biomedical Materials Research.* 59 (2), (2002), 312-317.

Fedoroff, M; Jeanjean, J; Rouchaud, J; Mazerolles, L; Trocellier, P; Maireles-Torres, P; Jones; D. "Sorption Kinetics and Diffusion of Cadmium in Calcium Hydroxyapatites". *Solid State Sciences*. 1, (1999) 71-84.

Felker, D; Sherwood, P. "Zinc Phosphate (Zn3(PO4)2) by XPS". *Surface Science Spectra*, vol 9 (2002) 106-113.

Fuller, C; Bargar, J; Davis, J. Piana, M. "Mechanism of Uranium Interactions with Hydroxyapatite: Implications for Groundwater Remediation". *Environmental Science and Technology*. 36 (2002) 158-165.

Fuller, C; Bargar, J; Davis, J. "Molecular-Scale Characterization of Uranium Sorption by Bone Apatite Materials for Permeable Reactive Barrier Demonstration". *Environmental Science and Technology*. 37 (2003) 4642-4649.

FHWA. "The user guidelines for waste and byproduct materials in pavement construction." Turner-Fairbank Highway Research Center; FHWA, 1998.

Duc, M; Lefevre, G; Fedoroff, M; Jeanjean, J; Rouchaud, J.C.; Monteil-Rivera, F; Dumonceau, J; Milonjic, S. "Sorption of selenium anionic species on apatites and iron oxides from aqueous solutions". *Journal of Environmental Radioactivity*, 70 (2003), 61-72.

Jarcho, M; Bolen, C.H.; Thomas, M.B.; Bobick, J; Kay, J.F.; Doremus, R.H. "Hydroxylapatite Synthesis and Characterization in Dense Polycrystalline Form". *Journal of Materials Scienc.* 11 (1976) 2027-2035.

Kulik, D; Kersten, M. "Zqueous Solubility Diagrams for Cementitious Waste Stabilization Systems. 4. A Carbonation Model for Zn-doped Calcium Silicate Hydrate by Gibbs Energy Minimization". *Environmental Science & Technology*, 36 (2002) 2926-2931.

Lee, Y; Elzinga, E; Reeder, R. "Sorption Mechanisms of Zinc on Hydroxyapatite: Systematic Uptake Studies and EXAFS Spectroscopy Analysis". *Environmental Science & Technology*, 39 (2005) 4042-4048.

Leyva, A, Marrero, Smichowski, P; Cicerone, D. "Sorption of Antimony onto Hydroxyapatite". *Environmental Science and Technology*. 2001, 35, 3669-3675.

Li, L; Stanforth, R. "Distinguishing Adsorption and Surface Precipitation of Phosphate on Goethite (-FeOOH)". *Journal of Colloid and Interface Science*, 230 (2000) 12-21.

Lower, S; Maurice, P; Traina, S; Carlson, E. "Aqueous Pb sorption by hydroxylapatite: Applications of atomic force microscopy to dissolution, nucleation, and growth studies." *American Mineralogist.* 83 (1998) 147-158.

Ma, Q.Y; Traina, S.J.; Loga, T.J; Ryan, J.A. "In situ Pb immobilization by apatite" *Environmental Science & Technology*, 27 (1993) 1219-1228.

Mandjiny, S, Zouboulis, A.I. & Matis, K.A. "Removal of Cadmium from Dilute Solutions by Hydroxyapatite. I. Sorption Studies". *Separation Science and Technology*, 30(15), pp. 2963-2978, 1995.

Middelburg, J; Comans, R.N.J. "Sorption of Cadmium on Hydroxyapatite". *Chemical Geology*, 90 (1991) 45-53.

Monteil-Rivera, F; Fedoroff, M; Jeanjean, J; Minel, L; Barthes, M; Dumonceau, J. "Sorption of Selenite (SeO_3^{2-}) on Hydroxyapatite: An Exchange Process". *Journal of Colloid and Interface Science*, 221 (2000) 291-300.

Monteil-Rivera, F; Fedoroff, M; Jeanjean, J. "Sorption of Selenite Ions on Hydroxyapatites." *Journal of Materials Science*, 18 (1999) 1143-1145.

Moulder, J. Stickle, W. Sobol, P. Bomben, K. *Handbook of X-Ray Photoelectron Spectroscopy*. Perkin Elmer Corporation (1992).

Newville, M. "Fundamentals of XAFS." cars9.uchicago.edu/xafs/tutorials.html (2004)

Nriagu, J.O. "Formation and stability of base metal phosphates in soils and sediments". *Phosphate minerals*. Berlin: Springer-Verlag, 1984. p. 318-29.

Nriagu, J.O. "Lead orthophosphates. IV: formation and stability in the environment." *Geochim Cosmochim Acta* 1974, 38:887.

Peld, M; Tonsuaadu, K; Bender, V. "Sorption and Desoprtion of Zn^{2+} and Cd^{2+} ions in Apatite-Aqueous Systems". *Environmental Science & Technology*, 38 (2004) 5626-5631.

Perrone, J; Fourest, B; Giffaut, E. "Sortpion of Nickel on Carbonate Fluoroapatites". *Journal of Colloid and Interface Science*, 239 (2001) 303-313.

Posner, A; Blumenthal, N; Betts, F. "Chapter 11: Chemistry and Structure of Precipitated Hydroxides" (1982).

Puls, R. "Permeable Reactive Barrier Technologies for Contaminant Remediation." USEPA/600/R-98/125 (1998)

Rakovan, J. Newville, M. Sutton, S. "Evidence of heterovalent europium in zoned Llallagua apatite using wavelength dispersive XANES". *American Mineralogist*. 86 (2001) 697-700

Rakovan, J. Reeder, R. Elzinga, E; Cherniak, D. Tait C. Morris, D. "Surface Characterization of U(VI) in Apatite by X-ray Absorption Spectroscopy". *Environmental Science & Technology*, 36 (2002) 3114-3117.

Ramachandran, G.N.; Srinivasan, R. *Fourier Methods in Crystallography*. Wiley Interscience.1970.

Ravel, B. Using Athena. feff.phys.washington.edu/~ravel/software/exafs (2005).

Roberts, D. Scheinost, A. Sparks D. "Zinc Speciation in a Smelter-Contaminated Soil Profile using Bulk and Microspectroscopic Techniques". *Environmental Science & Technology*, 36 (2002) 1742-1750.

Sauer, J.; Benson, C; Edil, T. "Metals Leaching from Highway Test Sections Constructed with Industrial Byproducts." (unpublished)

Singh, S.P; Ma, L.Q; Harris, W.G. "Heavy Metal Interactions with Phosphatic Clay: Sorption and Desorption Behavior." *Journal of Environmental Quality*. 30 (2001) 1961-1968.

Somasundaran, P; Wang, Y.H.C. "Surface Chemical Characteristics and Adsorption Properties of Apatite". *Adsorption on and Surface Chemistry of Hydroxyapatite*. (1984) 129-149.

Sposito, G. "Distinguishing Adsorption from Surface Precipitation." *ACS Symposium Series: Geochemical Processes at Mineral Surfaces* (1986) 217-228.

Sposito, G. *The Chemistry of Soils*. Oxford University Press (1989).

Stumm, W. *Chemistry of the Solid-Water Interface*. Wiley-Interscience Publication (1992)

CSMA Ltd. United Kingdom. www.csma.ltd.uk/techniques/xray_photoelectron.htm

Thomson, B; Smith, C; Busch, R; Siegel, M; Baldwin, C. "Removal of Metals and Radionuclides Using Apatite and Other Natural Sorbents." *Journal of Environmental Engineering*, (2003) 492-499.

Traina, Samuel; Laperche, V. "Contaminant Bioavailability in Soils, Sediments, and Aquatic Environments." *National Academy of Science colloquium "Geology, Mineralogy, and Human Welfare"* (1998) 3365-3371.

UNEP. *Enviornmental Aspects of Phosphate and Potash Mining*. (2001).

USGS; Jasinski, S: *USGS: Mineral Commodity Summaries: Phosphate Rock*. (2005).

Vega, E.D., Pedregosa, J.C. Narda, G.E. "Interaction of Oxovanadium(IV) with Crystalline Calcium Hydroxyapatite: Surface Mechanism with no Structural Modification." *Journal of Physics and Chemistry of Solids*, 60 (1999) 759-766.

Waychunas, G.A.; Fuller, C.C.; Davis, J.A. "Surface complexation and precipitate geometry for aqueous Zn(II) sorption on ferrihydrite I: X-ray absorption extended fine structure spectroscopy analysis." *Geochimica et Cosmochimica Acta*. VOL 66(7), (2002), 1119-1137.

Weber, W. *Physicochemical processes for Water Quality Control*. John Wiley & Sons Press. 1972.

Wu, L; Forsling, W; Schindler, P. "Surface Complexation of Calcium Minerals in Aqueous Solution". *Journal of Colloid and Interface Science*. 147, No. 1 (1991) 178-185.

Xu, Y; Schwartz, F.W. "Sorption of Zn^{2+} and Cd^{2+} on Hydroxyapatite Surfaces." *Environmental Science and Technology*, 28, No. 8 (1994).

ZetaSizer Nano Series, User Manual. Malvern Instruments (2004).

APPENDIX A

XPS spectra

TABLE A.1: Zn 2p and Zn LMM BE References

Element	Mineral	Position, eV	Reference
Zn 2p	$Zn_5(CO_3)_2(OH)_6$	1021.4	Dake L.S., Baer D.R., Zachara J.M. (1989)
		1021.6	Moretti G., Fierro G., Lo Jacono M., Porta P. (1989)
		1022.7	Dake L.S., Baer D.R., Zachara J.M. (1989)
	Zn	1021.9	**NIST**
		1021.6	**NIST**
		1021.7	NIST
		1021.8	NIST
		1021.9	NIST
		1020.8	NIST
		1022.1	NIST
		1021	NIST
		1021.8	GaWi77, + (PE)
	ZnO	1022.1	Barr T.L., Yin M., Varma S (1992), Deroubaix
		1022.3	Dake L.S., Baer D.R., Zachara J.M. (1989)
		1021.9	Campbell C.T., Daube K.A., White J.M
		1022.5	GaWi77
		1022.7	Zachara *et. al.* (1988)
		1021.8	Scho73a, WRDM79 (PE)
		1022	NIST
		1021.6	NIST
		1021.8	NIST
		1021.4	NIST
		1021.5	NIST
		1021.2	NIST
	$CaZn_2(PO_4)_6$	1022.43	this work
	$Zn(PO_4)_2$	1022.45	this work
	$ZnCO_3$	1022.5	Dake L.S., Baer D.R., Zachara J.M. (1989)
	$Zn_3(PO_4)_2$	1022.65	this work
	$Zn(OH)_2$	1022.7	Dake L.S., Baer D.R., Zachara J.M. (1989)
		1022.3	Harvey, D.T.; Linton, R.W. (1984)
Zn LMM	$Zn_3(PO_4)_2$	986.415	this work
		986.7	Zin *et. al.* (2004)
	$Zn(OH)_2$	986.60	Deroubaix *et. al.* (1992)
		987.2	Deroubaix *et. al.* (1992)
		986.5	Dake L.S., Baer D.R., Zachara J.M. (1989)
	$CaZn_2(PO_4)_6$	986.5	this work
	$Zn(PO_4)_2$	986.3	this work
		987.4	Dake L.S., Baer D.R., Zachara J.M. (1989)
	$ZnCO_3$	988.0	Moretti G., Fierro G., Lo Jacono M., Porta P. (1989)
	$Zn_5(CO_3)_2(OH)_6$	987.1	Dake L.S., Baer D.R., Zachara J.M. (1989)
		988.2	Deroubaix *et. al.* (1992)
	ZnO	987.7	NIST
		988.8-988.9	NIST

TABLE A.2: Ca 2p, P 2p, O 1s, F 1s and C 1s BE Reference			
Element	**Mineral**	**Position, eV**	**Reference**
Ca	$Ca_5(PO_4)_3OH$	347.13	Eighmy *et. al.* (1999)
		347.4	Zin *et. al.* (2004)
		347.8	Landis W.J., Martin J.R. (1984)
Ca	$Ca_5(PO_4)_2F$	347.6	Landis W.J., Martin J.R. (1984)
Ca	$CaZn_2(PO_4)_6$	347.87	this work
P 2p	$Zn_3(PO_4)_2$	133.5	Felker D, Sherwood P (2003)
		133.6	Zin *et. al.* (2004)
	$Ca_5(PO_4)_3OH$	132.86	Eighmy *et. al.* (1999)
		133.2	Zin *et. al.* (2004)
		133.8	Landis W.J., Martin J.R. (1984)
P 2p	$CaZn_2(PO_4)_6$	134.05	this work
P 2p	$Ca(H_2PO_4)_2·H_2O$	134.3	Zin *et. al.* (2004)
O 1s	$Zn_3(PO_4)_2$	532.0	this work
		533.89	Felker D, Sherwood P (2003)
	ZnO	529.9	Haber J., Stoch J., Ungier, L
		530.2	Barr T.L., Yin M., Varma S (1992)
		530.3	**NIST**
		530.4	NIST
		530.5	Deroubaix *et. al.* (1992)
		530.6	NIST
		530.8	Barr T.L., Yin M., Varma S (1992)
		530.9	NIST
		531.2	NIST
	$Ca_5(PO_4)_3OH$	531.1	Eighmy *et. al.* (1999)
		531.8	Landis W.J., Martin J.R. (1984)
	$CaZn_2(PO_4)_6$	531.7	this work
	oxide	529.6 - 529.8	Zin *et. al.* (2004)
	phosphate	531.1- 531.4	Zin *et. al.* (2004)
	hydroxide	532.6 - 533.1	Zin *et. al.* (2004)
	carbonates	531.5 - 532.5	Perkin Elmer (1992)
	H_2O	532.8	NIST
		533.1	NIST
		533.3	NIST
		534.8	NIST
		535.1	NIST
		538	NIST
F 1s	$Ca_5(PO_4)_3(OH,F)$	684.5	Eighmy *et. al.* (1999)
	$CaZn_2(PO_4)_6$	684.6	Landis W.J., Martin J.R. (1984)
C 1s	$Zn_5(CO_3)_2(OH)_6$	289.1	Moretti G., Fierro G., Lo Jacono M., Porta P. (1989)
	$Ca_5(PO_4)_3OH$	284.8	Eighmy *et. al.* (1999)
	CO_3	288-291.5	NIST
	$Zn_3(PO_4)_2$ (syn)	281.715	this work
	$Zn_3(PO_4)_2$	281.552	this work
	$CaZn_2(PO_4)_6$	281.55	this work

(a) Ca 2p

x 10^1

Name	Pos.	FWHM	%Area
Ca 2p	347.39	1.819	67.567
Ca 2p	350.93	1.947	32.433

Binding Energy (eV)

(b) O 1s

x 10^1

Name	Pos.	FWHM	%Area
O 1s	531.18	1.885	100.000

Binding Energy (eV)

(c) P 2p

Name	Pos.	FWHM	%Area
P 2p	133.57	2.095	100.000

Binding Energy (eV)

(d) C 1s

x 10^1

Name	Pos.	FWHM	%Area
C 1s	284.80	1.778	100.000

Binding Energy (eV)
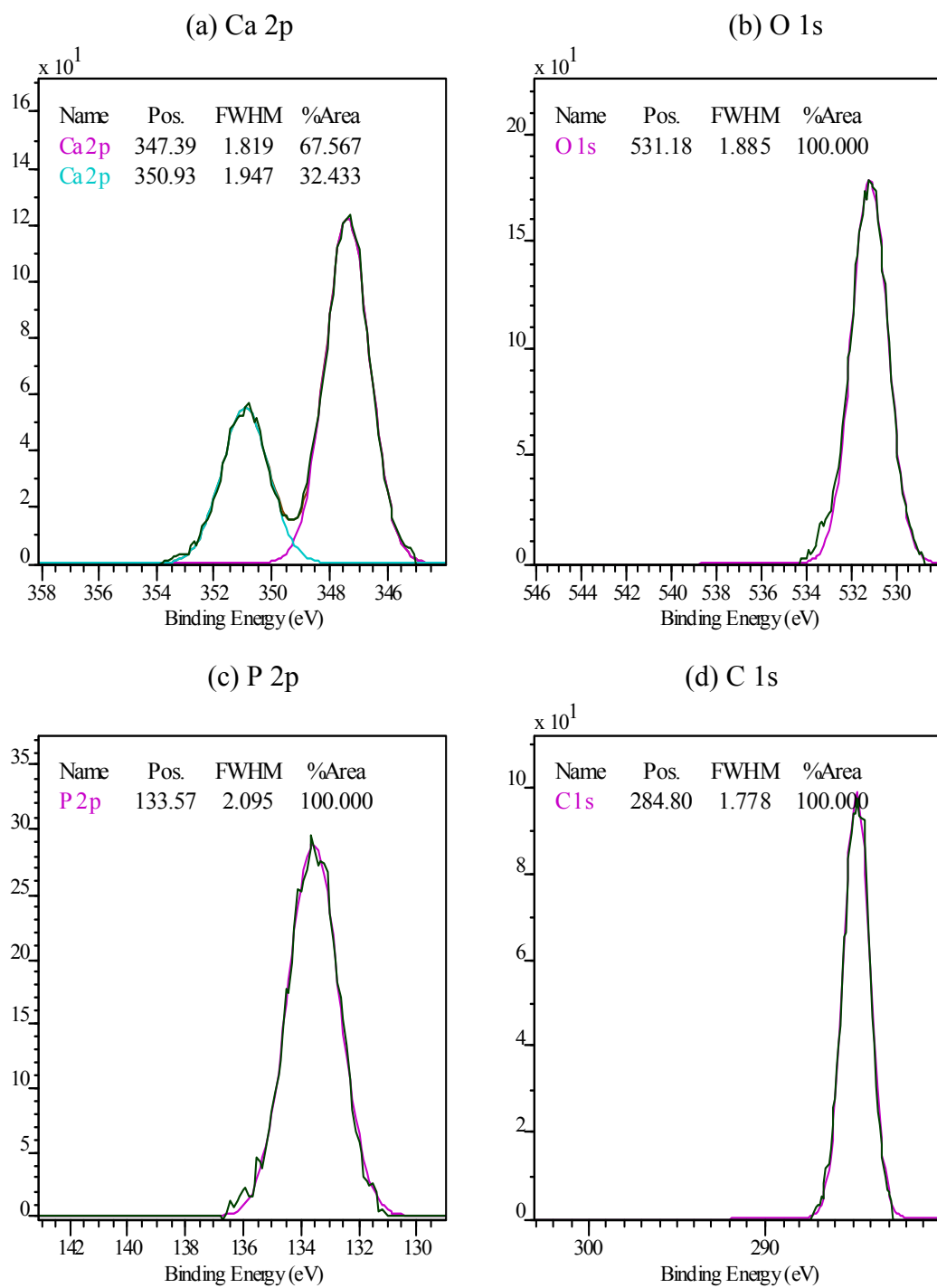
Figure A.1: (a) Ca 2p, (b) O 1s, (c) P 2p and (d) C 1s photoelectron lines of HAP with no Zn-loading

(a) Ca 2p

Name	Pos.	FWHM	%Area
Ca 2p	347.45	1.849	66.681
Ca 2p	350.97	1.945	33.319

(b) O 1s

Name	Pos.	FWHM	%Area
O 1s	531.31	1.994	95.261
O 1s	533.63	1.665	4.739

(c) P 2p

Name	Pos.	FWHM	%Area
P 2p	133.58	1.990	100.000

(d) C 1s

Name	Pos.	FWHM	%Area
C 1s	284.80	1.897	100.000
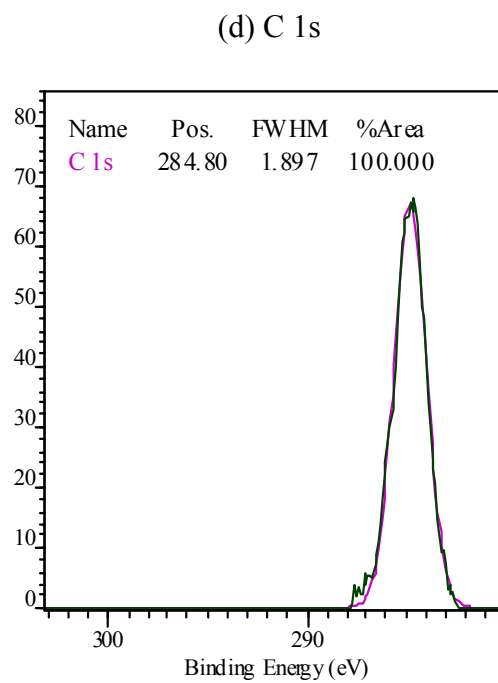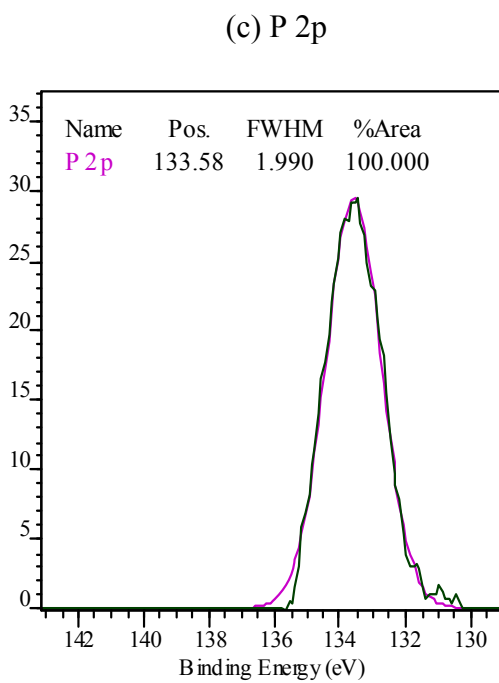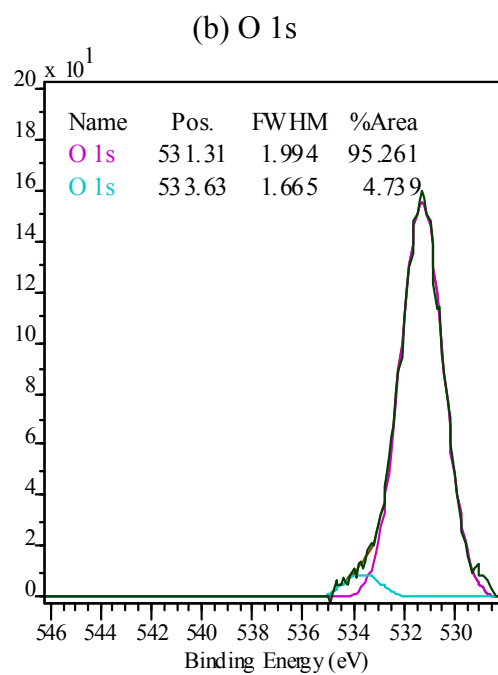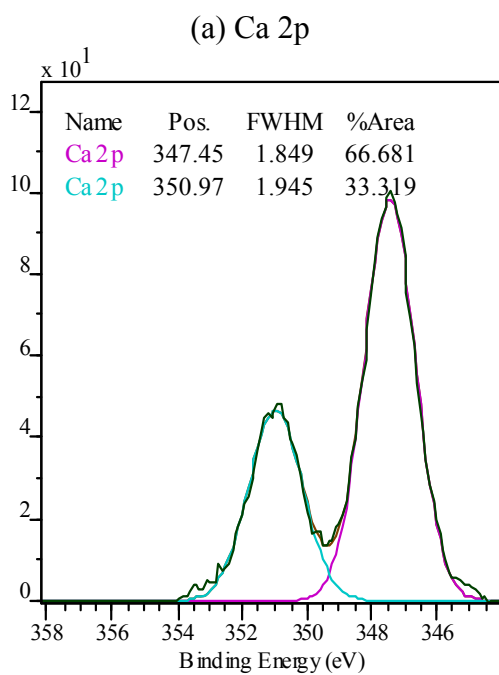
Figure A.2: (a) Ca 2p, (b) O 1s, (c) P 2p and (d) C 1s photoelectron lines of 0.93 mmol/g HAP

(a) Ca 2p

Name	Pos.	FWHM	%Area
Ca 2p	347.20	1.754	77.213
Ca 2p	350.81	1.380	22.787

(b) O 1s

Name	Pos.	FWHM	%Area
O 1s	531.14	2.238	100.000

(c) P 2p

Name	Pos.	FWHM	%Area
P 2p	133.49	2.244	100.000

(d) C 1s

Name	Pos.	FWHM	%Area
C 1s	284.80	1.934	100.000
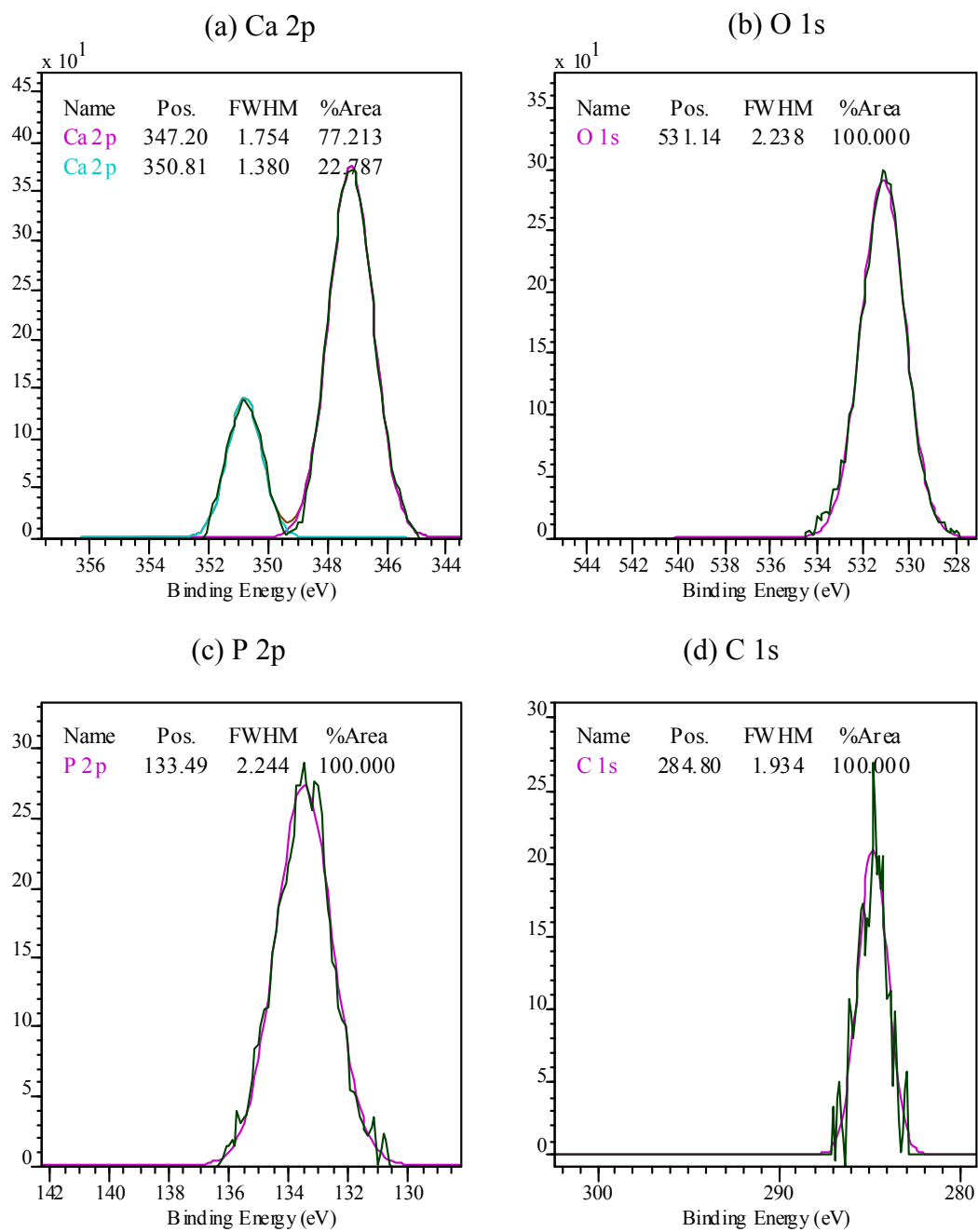
Figure A.3: (a) Ca 2p, (b) O 1s, (c) P 2p and (d) C 1s photoelectron lines of 8.26 mmol/g HAP

(b) O 1s

Name	Pos.	FWHM	%Area
Ca 2p	347.44	2.045	65.536
Ca 2p	350.95	2.209	34.464

Name	Pos.	FWHM	%Area
O 1s	531.19	2.194	100.000

(c) P 2p

Name	Pos.	FWHM	%Area
P 2p	133.62	2.487	100.000

(d) C 1s

Name	Pos.	FWHM	%Area
C 1s	284.80	2.031	100.000
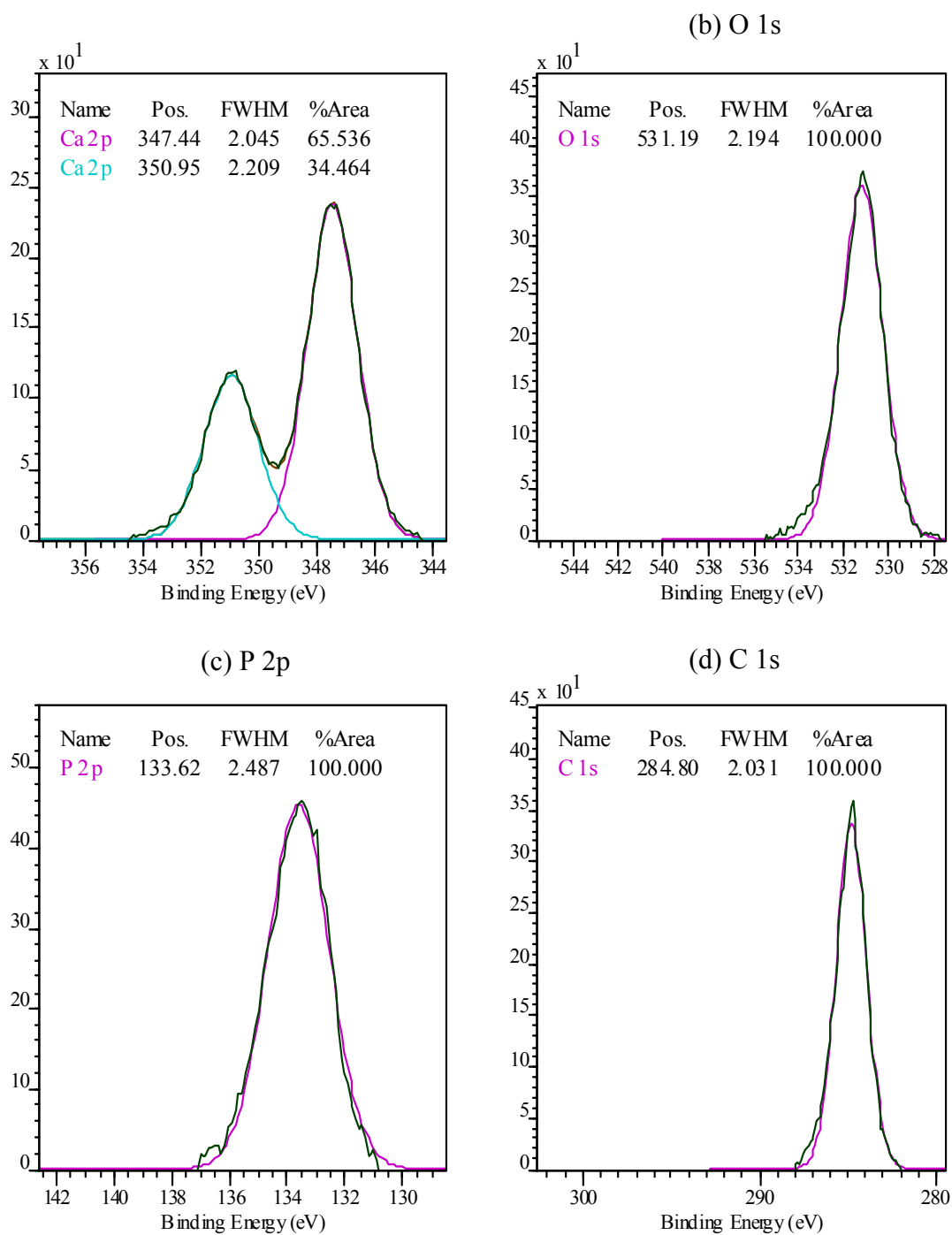
Figure A.4: (a) Ca 2p, (b) O 1s, (c) P 2p and (d) C 1s photoelectron lines of CAP with no Zn-loading

60

(a) Ca 2p

x 10¹

Name	Pos.	FWHM	%Area
Ca 2p	347.49	2.013	66.246
Ca 2p	351.03	2.133	33.754

(b) O 1s

x 10¹

Name	Pos.	FWHM	%Area
O 1s	531.21	2.037	87.016
O 1s	532.95	2.006	12.984

(c) P 2p

Name	Pos.	FWHM	%Area
P 2p	133.82	2.390	100.000

(d) C 1s

x 10¹

Name	Pos.	FWHM	%Area
C 1s	284.80	1.973	100.000
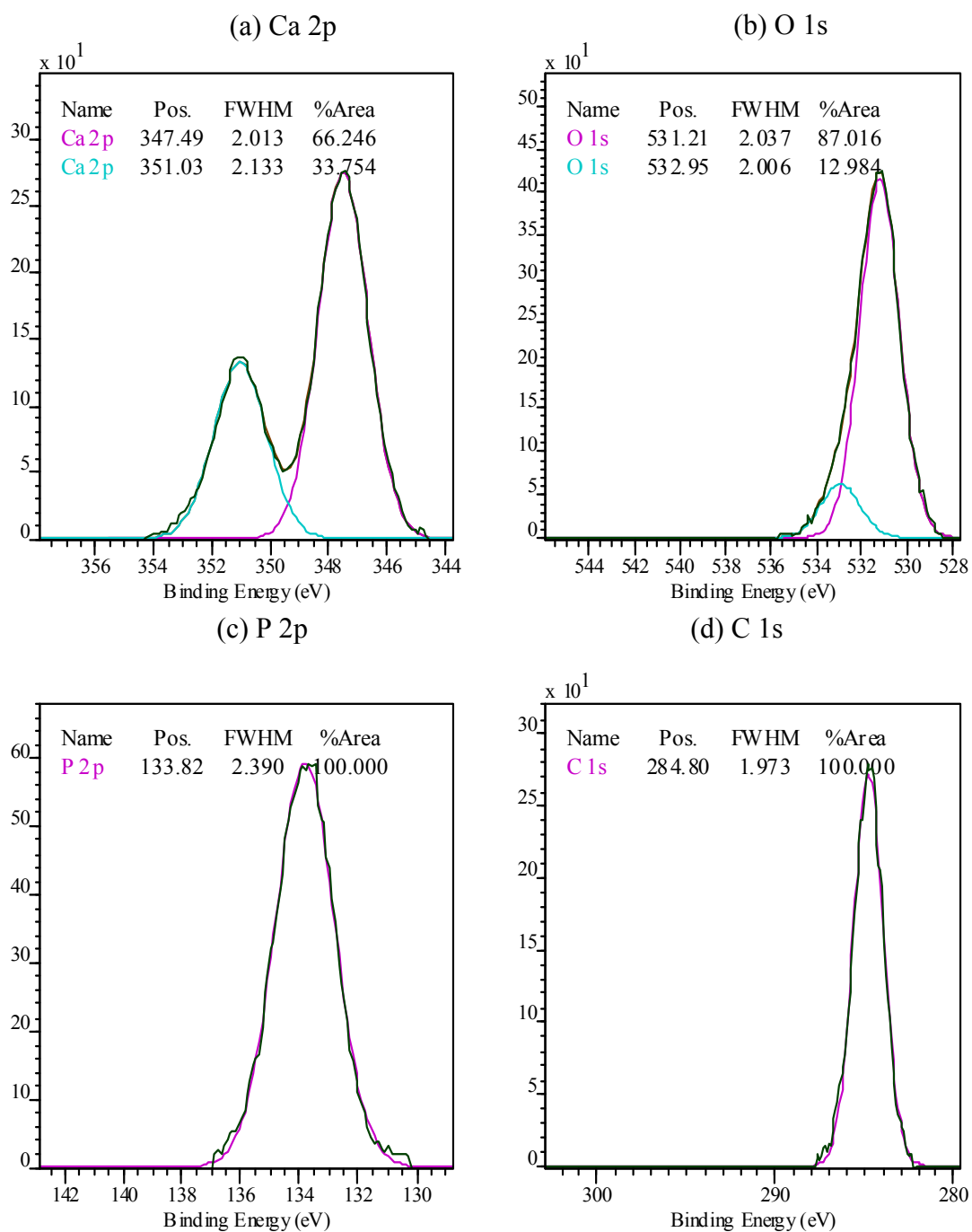
Figure A.5: (a) Ca 2p, (b) O 1s, (c) P 2p and (d) C 1s photoelectron lines of 0.99 mmol/g CAP
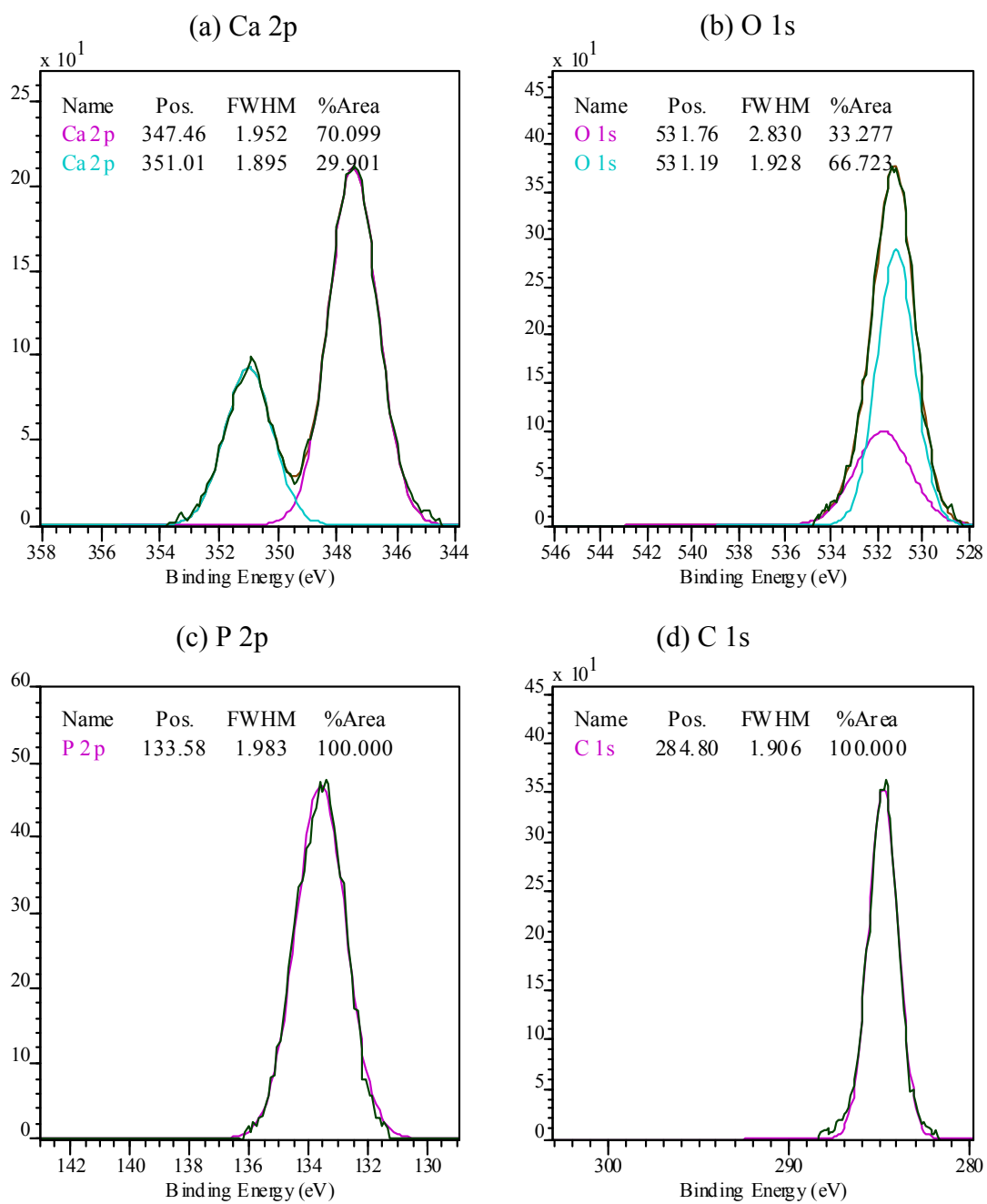
Figure A.6: (a) Ca 2p, (b) O 1s, (c) P 2p and (d) C 1s photoelectron lines of 4.48 mmol/g CAP

(a) Ca 2p

x 10^1

Name	Pos.	FWHM	%Area
Ca 2p	347.56	1.983	66.846
Ca 2p	351.09	2.095	33.154

Binding Energy (eV)

(b) O 1s

x 10^1

Name	Pos.	FWHM	%Area
O 1s	531.35	2.198	100.000

Binding Energy (eV)

(c) P 2p

Name	Pos.	FWHM	%Area
P 2p	133.63	2.120	100.000

Binding Energy (eV)

(d) F 1s

Name	Pos.	FWHM	%Area
F 1s	684.54	2.222	100.000

Binding Energy (eV)
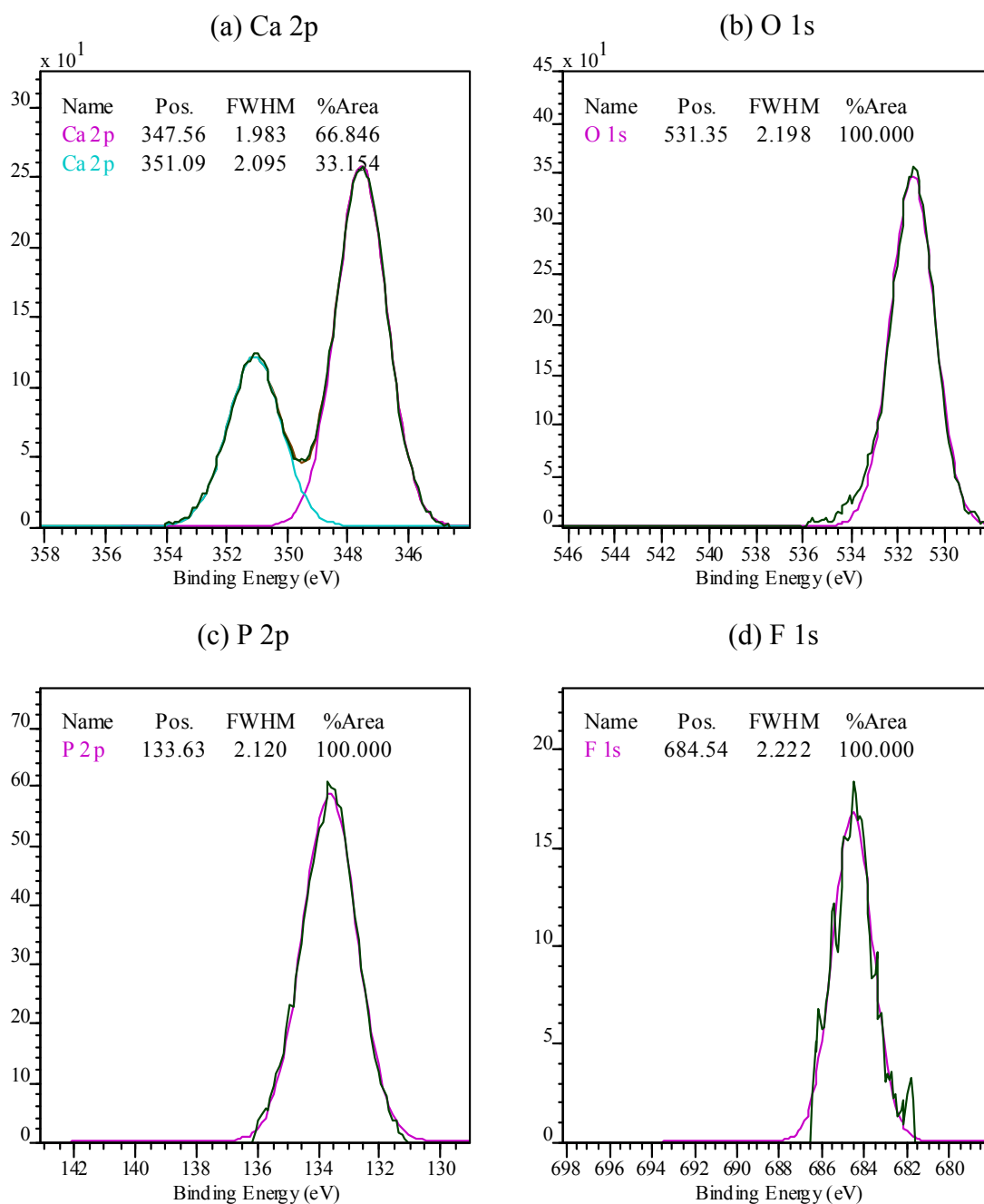
Figure A.7: (a) Ca 2p, (b) O 1s, (c) P 2p and (d) F 1s photoelectron lines of FAP with no Zn-loading

(a) Ca 2p

Name	Pos.	FWHM	%Area
Ca 2p	347.65	2.072	64.040
Ca 2p	351.13	2.224	35.960

(b) O 1s

Name	Pos.	FWHM	%Area
O 1s	531.46	2.135	78.465
O 1s	533.92	3.000	21.535

(c) P 2p

Name	Pos.	FWHM	%Area
P 2p	133.82	2.212	100.000
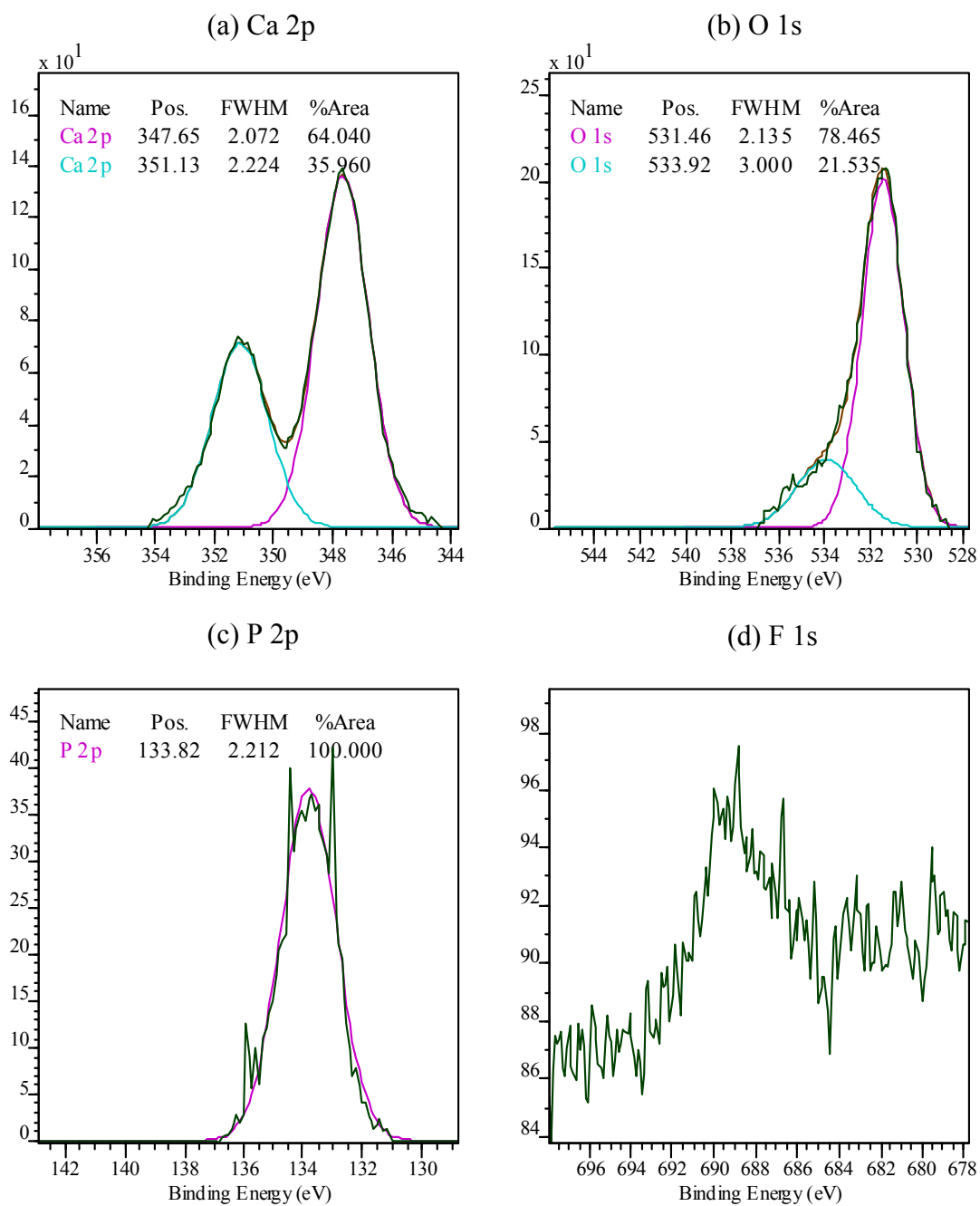
(d) F 1s

Figure A.8: (a) Ca 2p, (b) O 1s, (c) P 2p and (d) F 1s photoelectron lines of 0.92 mmol/g FAP
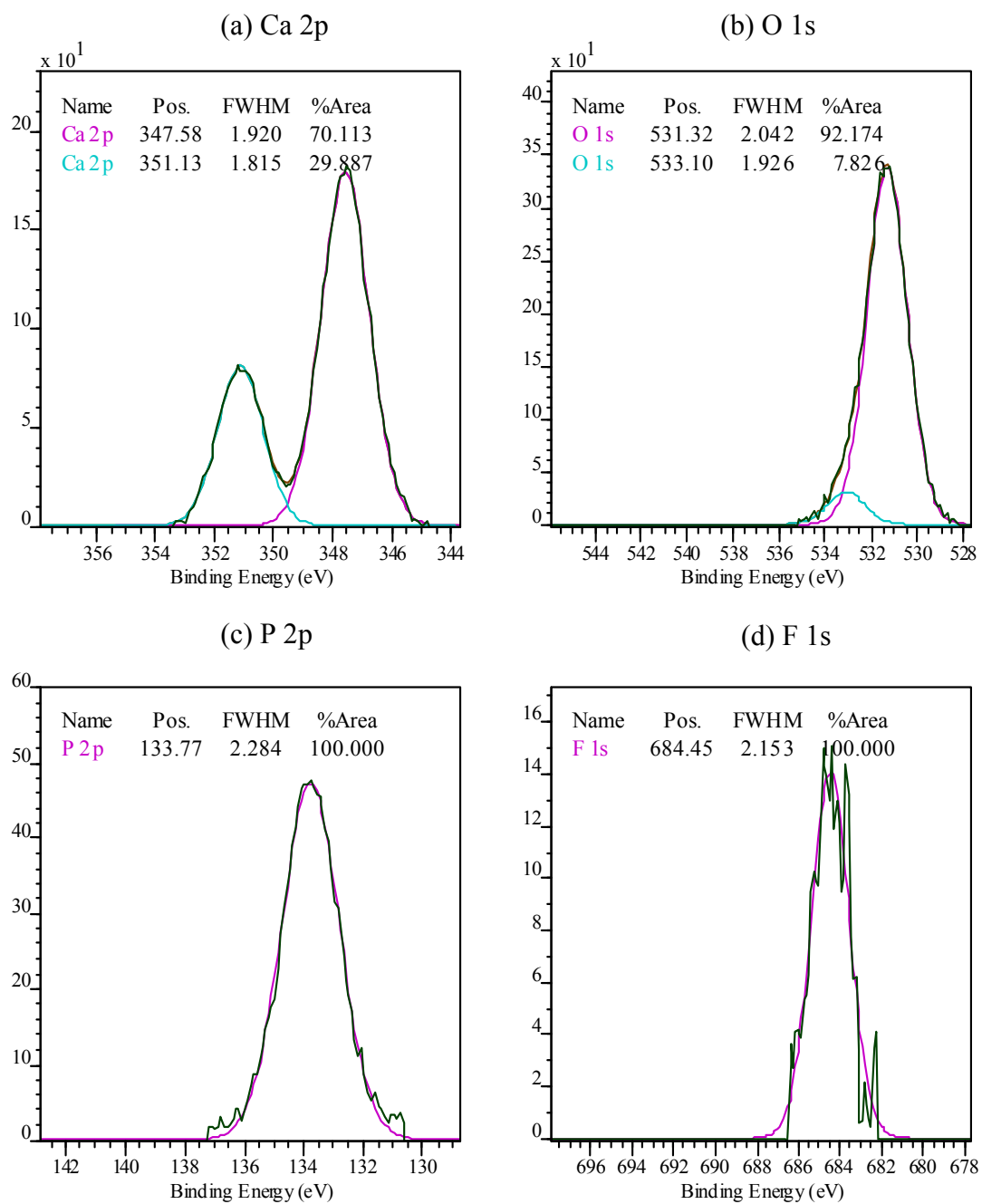
Figure A.9: (a) Ca 2p, (b) O 1s, (c) P 2p and (d) F 1s photoelectron lines of 2.74 mmol/g FAP

(a) General Survey - 0 mmol/g HAP
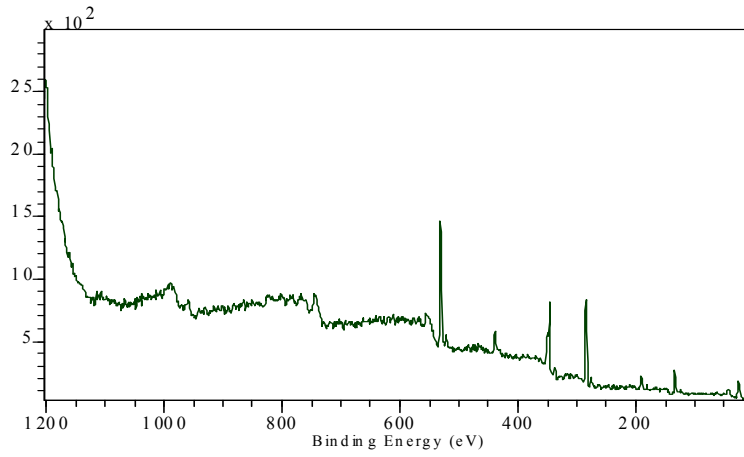
(b) General Survey - 0.93 mmol/g HAP
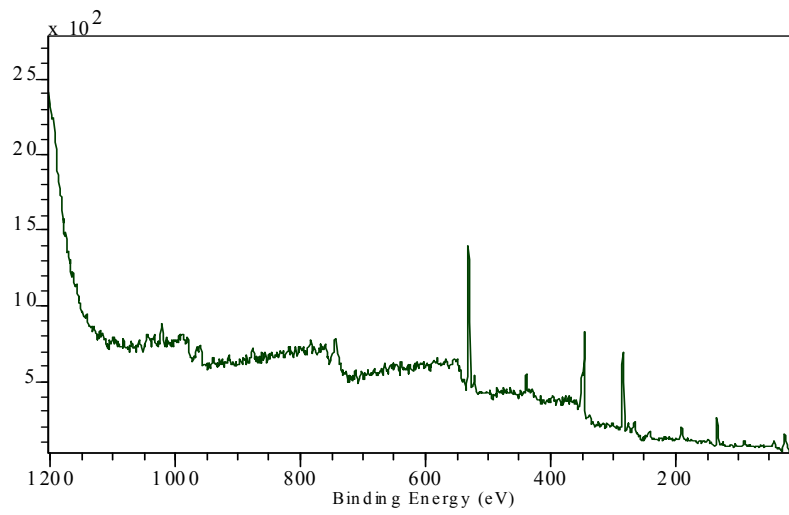
(c) General Survey - 8.26 mmol/g HAP
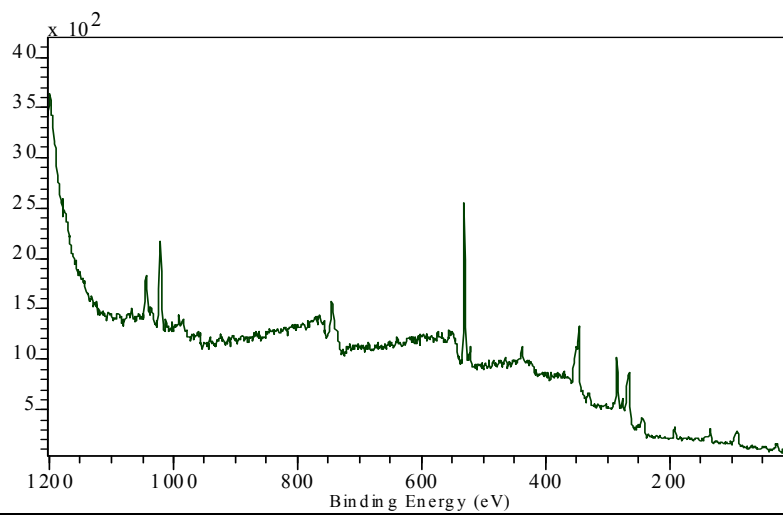
Figure A.10: General survey HAP (a) 0 mmol/g HAP, (b) 0.93 mmol/g HAP and (c) 8.26 mmol/g HAP

(a) General Survey - 0 mmol/g CAP
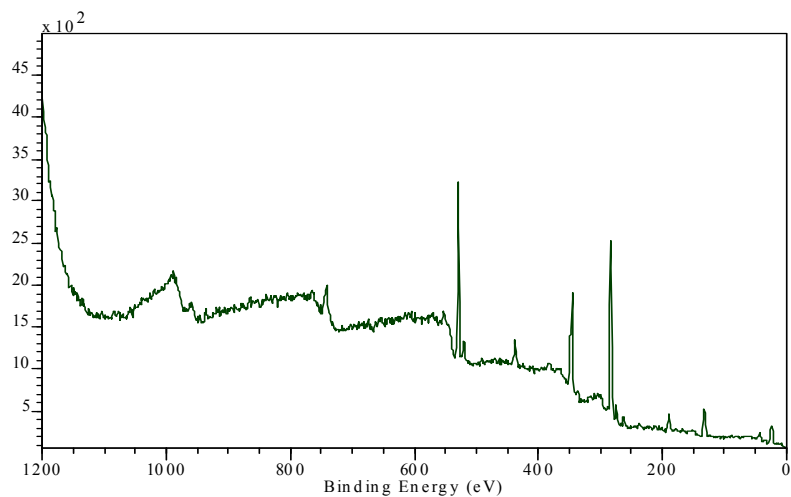
(b) General Survey - 0.99 mmol/g CAP
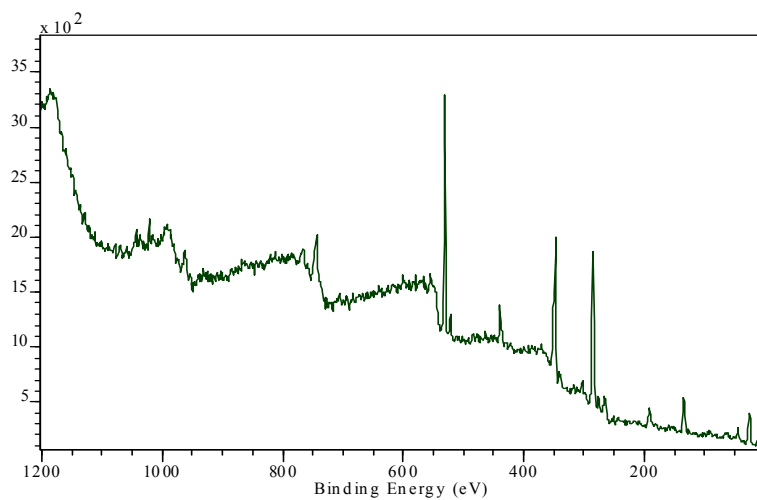
(c) General Survey - 4.48 mmol/g CAP
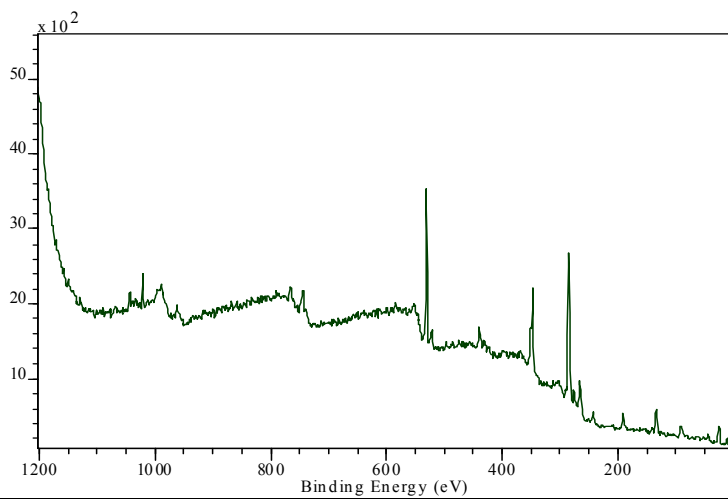
Figure A.11: General survey CAP (a) 0 mmol/g CAP, (b) 0.99 mmol/g CAP and (c) 4.48 mmol/g CAP

(a) General Survey - 0 mmol/g FAP
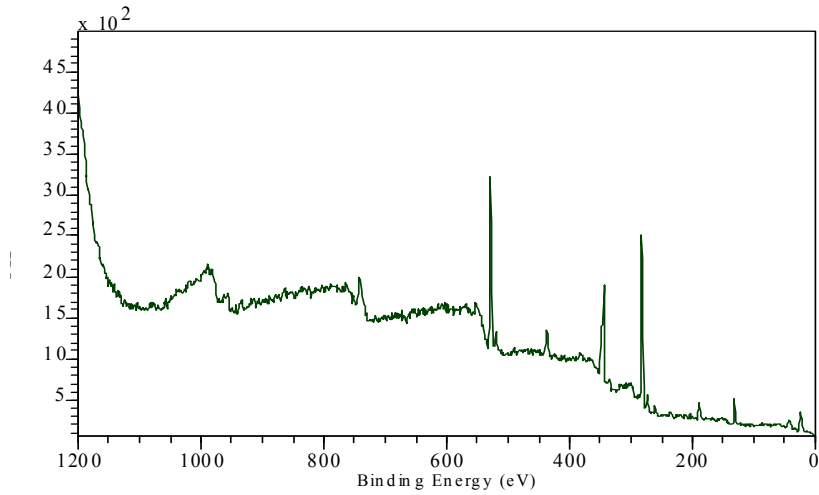
(b) General Survey - 0.92 mmol/g FAP
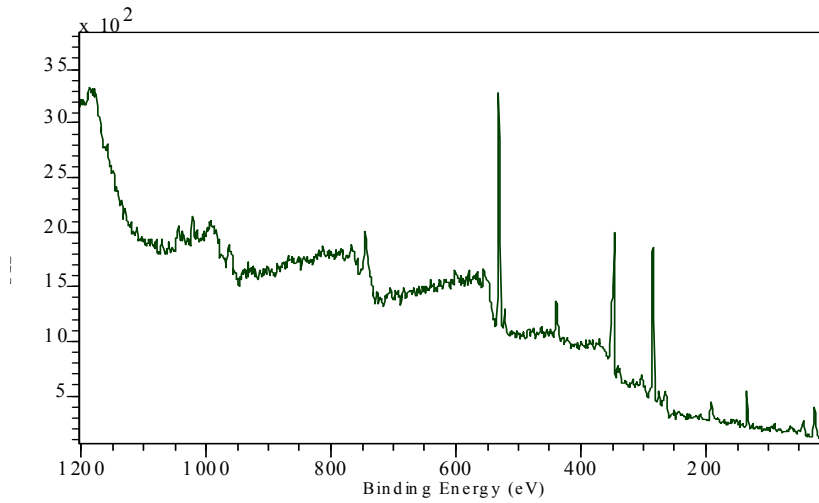
(c) General Survey - 2.74 mmol/g FAP
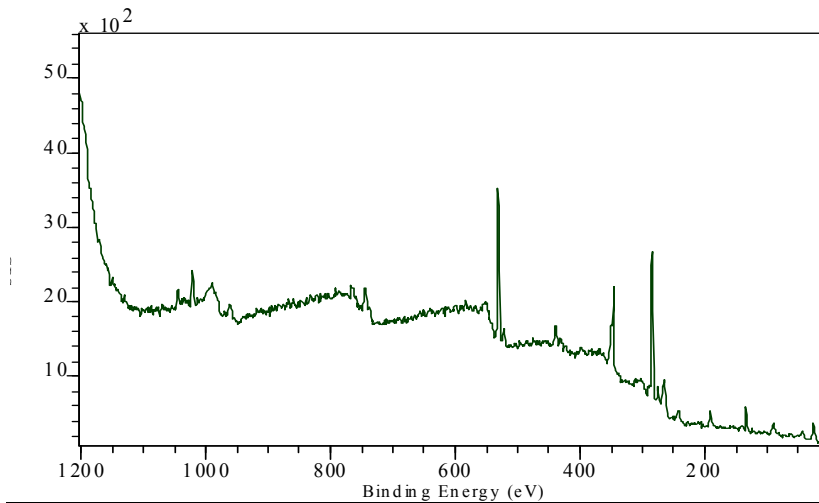
Figure A.12: General survey FAP (a) 0 mmol/g FAP, (b) 0.92 mmol/g FAP and (c) 2.74 mmol/g FAP

APPENDIX B

XAS spectra
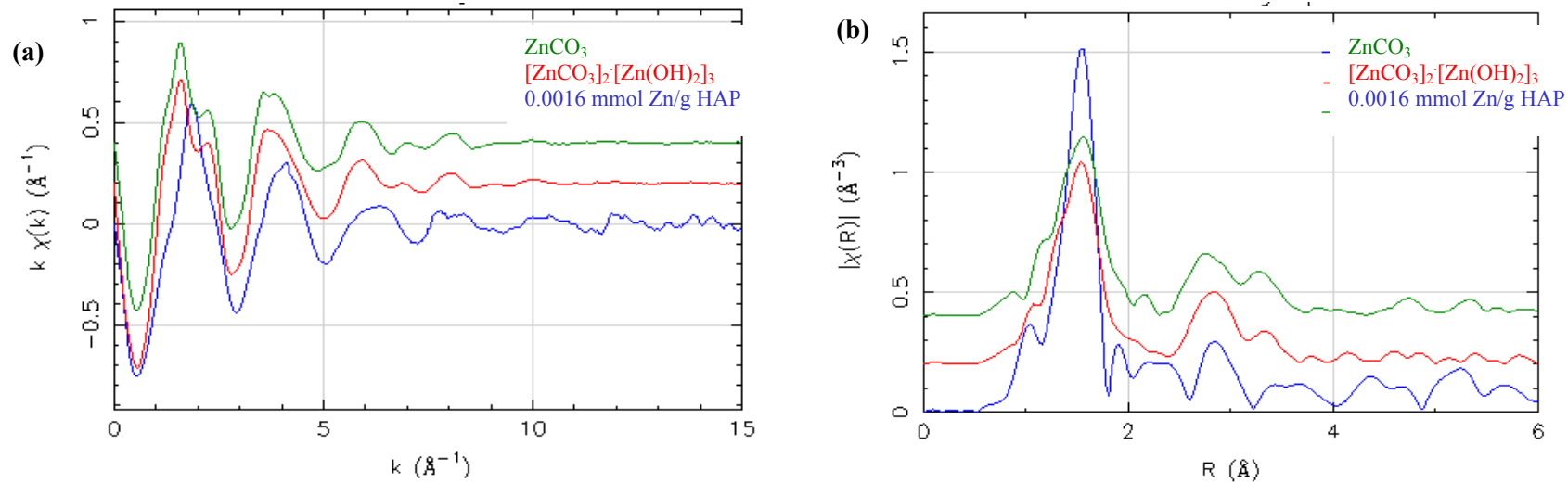
Figure B.1: (a) χ(k) & (b) χ (R) XAS spectra of 0.0016 mmol/g HAP, zinc carbonate, ZnCO₃ & zinc carbonate hydroxide, [ZnCO₃]₂·[Zn(OH)₂]₃

(a)

Zn₃(PO₄)₂
Zn₃(PO₄)₂ (syn)
0.0016 mmol Zn/g HAP

(b)

Zn₃(PO₄)₂
Zn₃(PO₄)₂ (syn)
0.0016 mmol Zn/g HAP
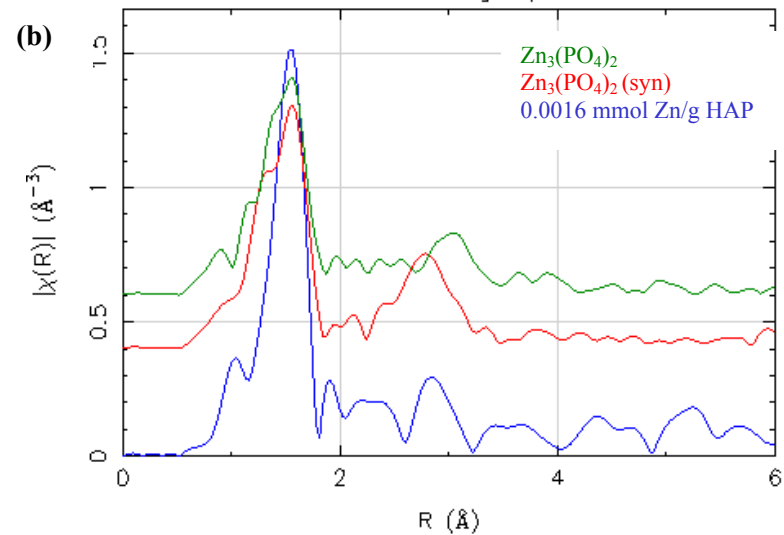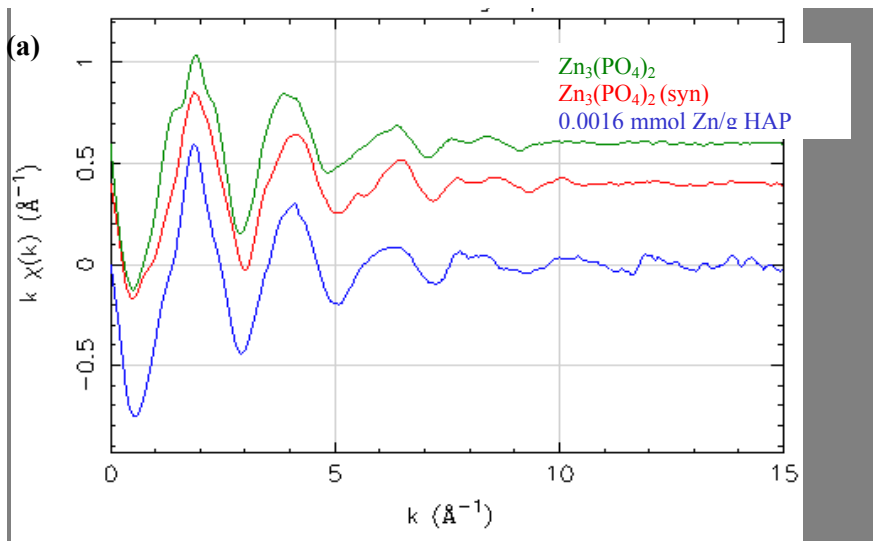
Figure B.2: (a) χ(k) & (b) χ (R) XAS spectra of 0.0016 mmol/g HAP, synthetic zinc phosphate, Zn₃(PO₄)₂ & hopeite, Zn₃(PO₄)₂

(a)

(Zn,Cu)Al₆(PO₄)₄(OH)₈·4(H₂O)
Zn₄(PO₄)₂(OH)₂·3(H₂O)
0.0016 mmol Zn/g HAP

(b)

(Zn,Cu)Al₆(PO₄)₄(OH)₈·4(H₂O)
Zn₄(PO₄)₂(OH)₂·3(H₂O)
0.0016 mmol Zn/g HAP

107

(a)

71

(b)
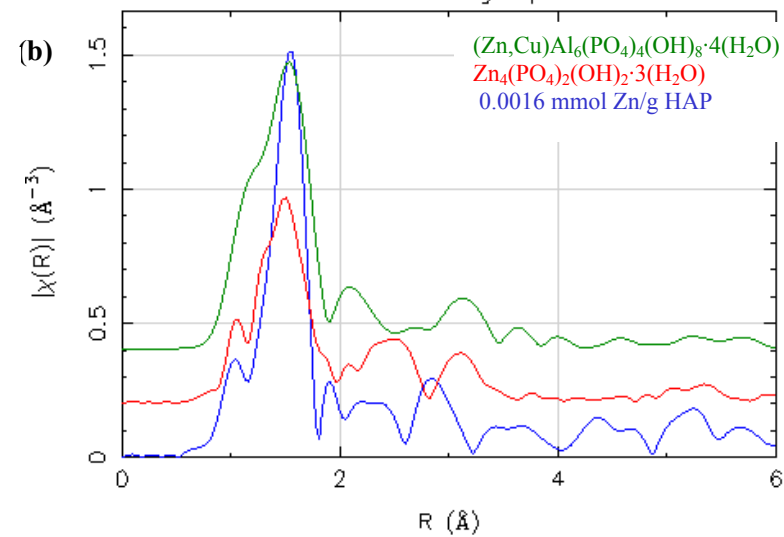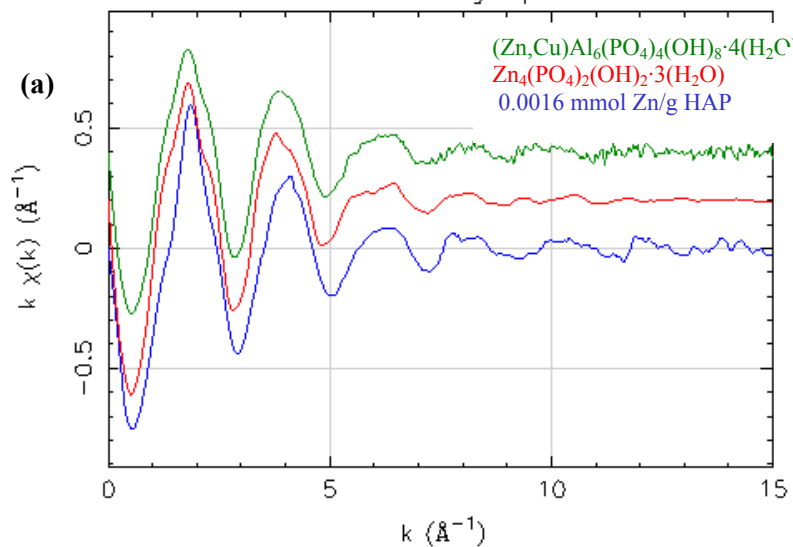
Figure B.3: (a) χ(k) & (b) χ (R) XAS spectra of 0.0016 mM/g HAP, spencerite, $Zn_4(PO_4)_2(OH)_2 \cdot 3(H_2O)$ & faustite $(Zn,Cu)Al_6(PO_4)_4(OH)_8 \cdot 4(H_2O)$
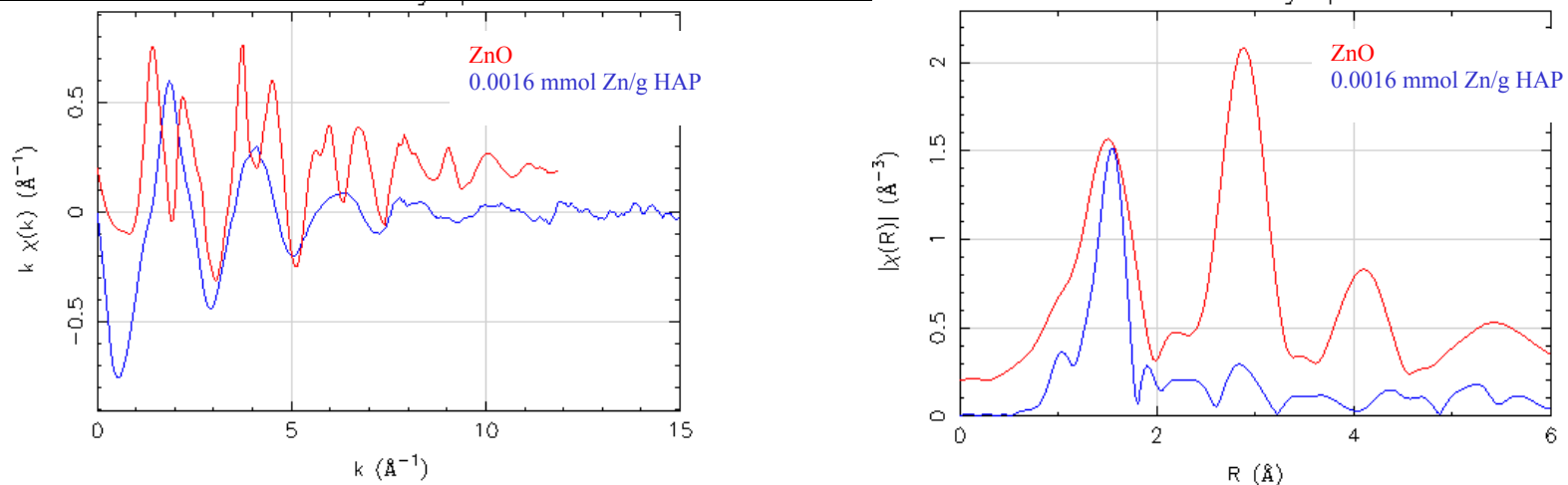
Figure B.4: (a) χ(k) & (b) χ (R) XAS spectra of 0.0016 mM/g HAP, & zinc oxide, ZnO
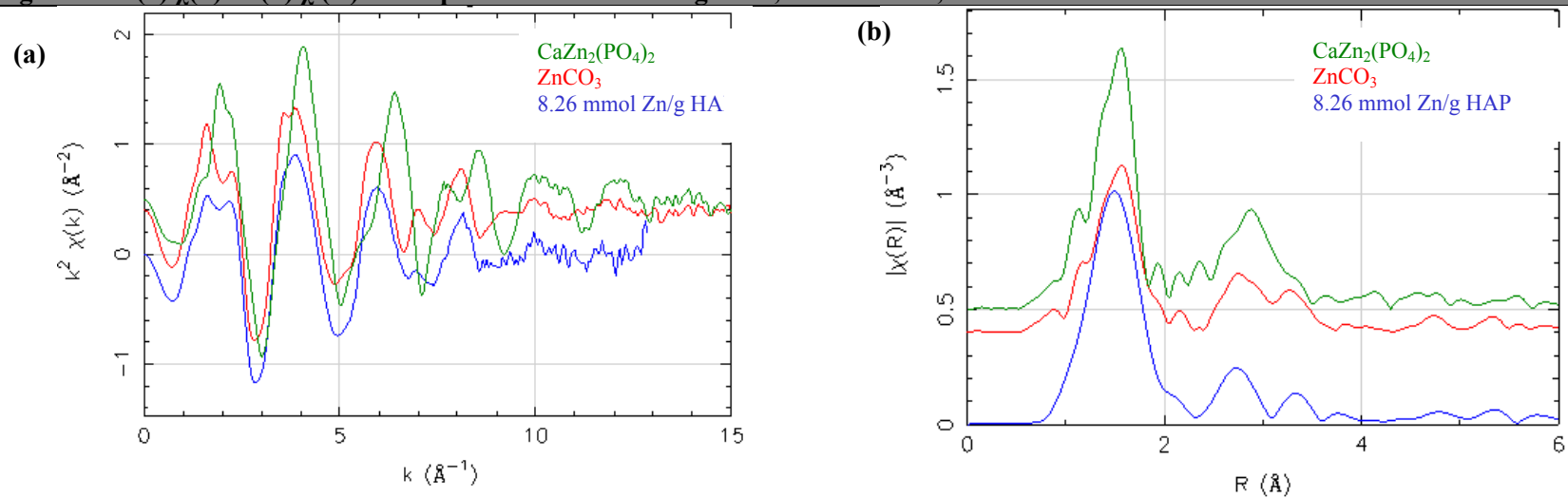
Figure B.5: (a) χ(k) & (b) χ (R) XAS spectra of 8.26 mmol/g HAP, zinc carbonate $ZnCO_3$ & scholzite, $CaZn_2(PO_4)_2$

(a)   (b)
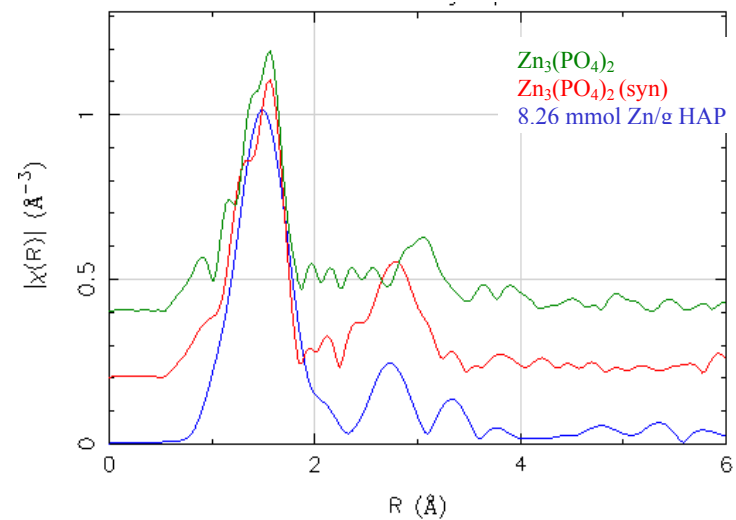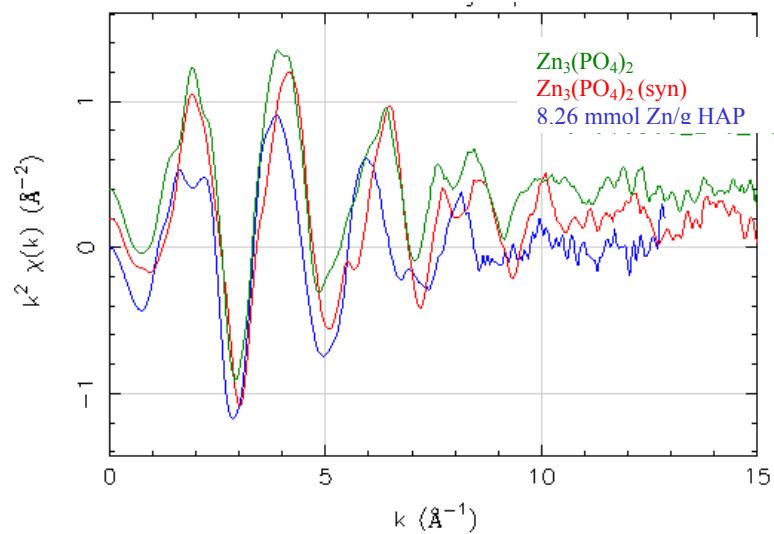
Figure B.6: (a) χ(k) & (b) χ (R) XAS spectra of 8.26 mmol/g HAP, synthetic zinc phosphate, $Zn_3(PO_4)_2$ & hopeite, $Zn_3(PO_4)_2$

(a)

(b)
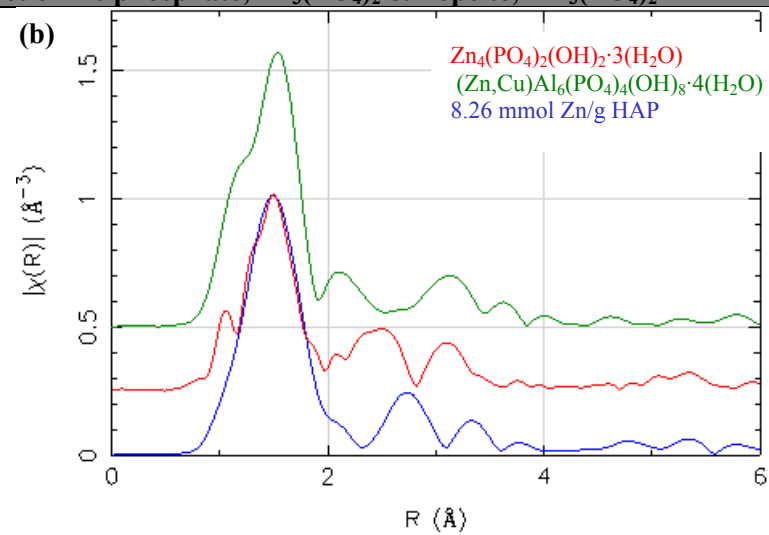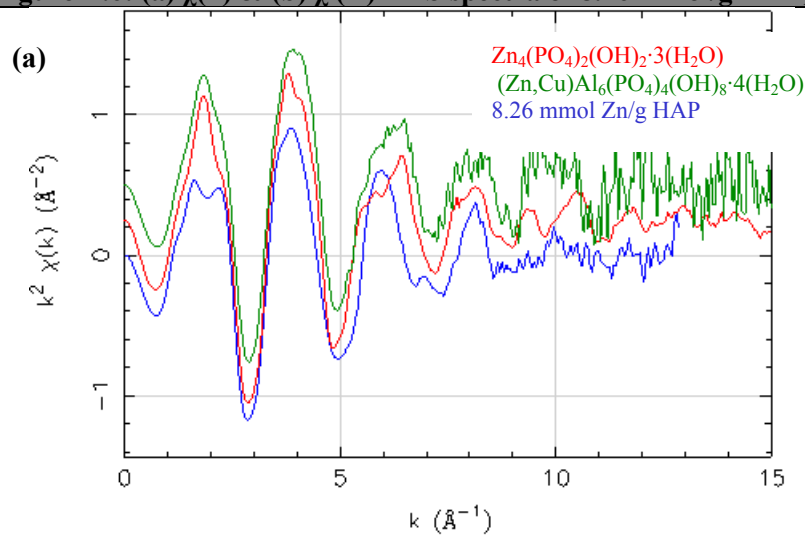
Figure B.7: (a) χ(k) & (b) χ (R) XAS spectra of 8.26 mmol/g HAP, spencerite, $Zn_4(PO_4)_2(OH)_2 \cdot 3(H_2O)$ & faustite $(Zn,Cu)Al_6(PO_4)_4(OH)_8 \cdot 4(H_2O)$
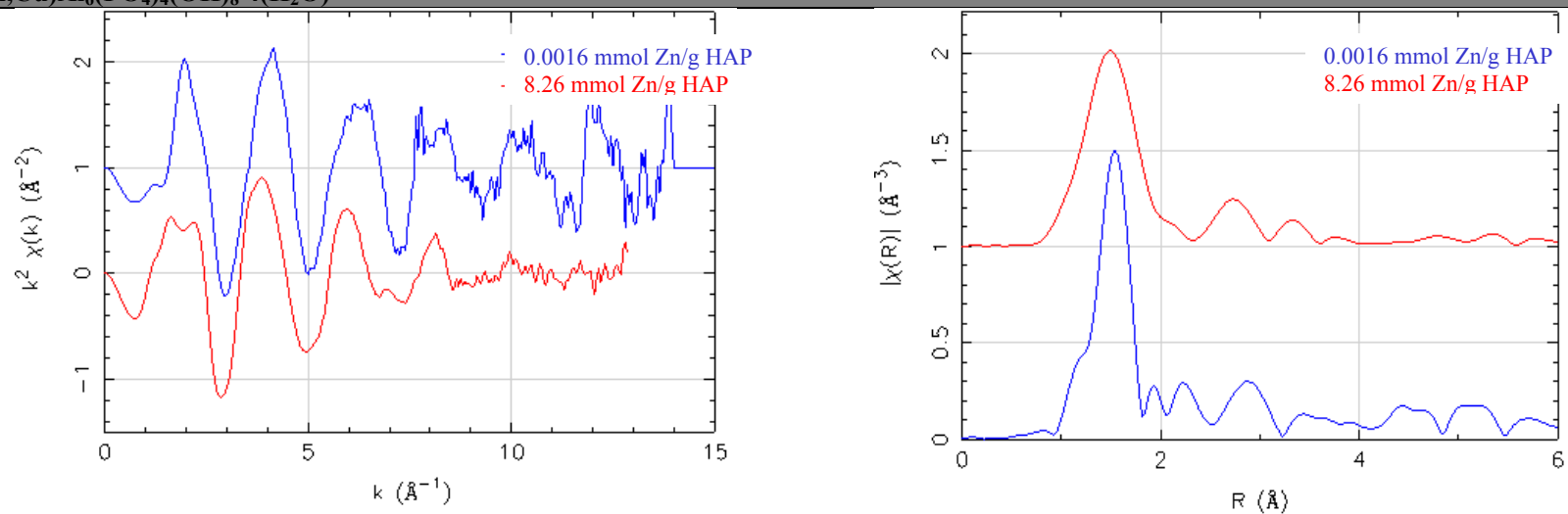
Figure B.8: (a) χ(k) & (b) χ (R) XAS spectra of 0.0016 mmol/g HAP & 8.26 mmol/g HAP
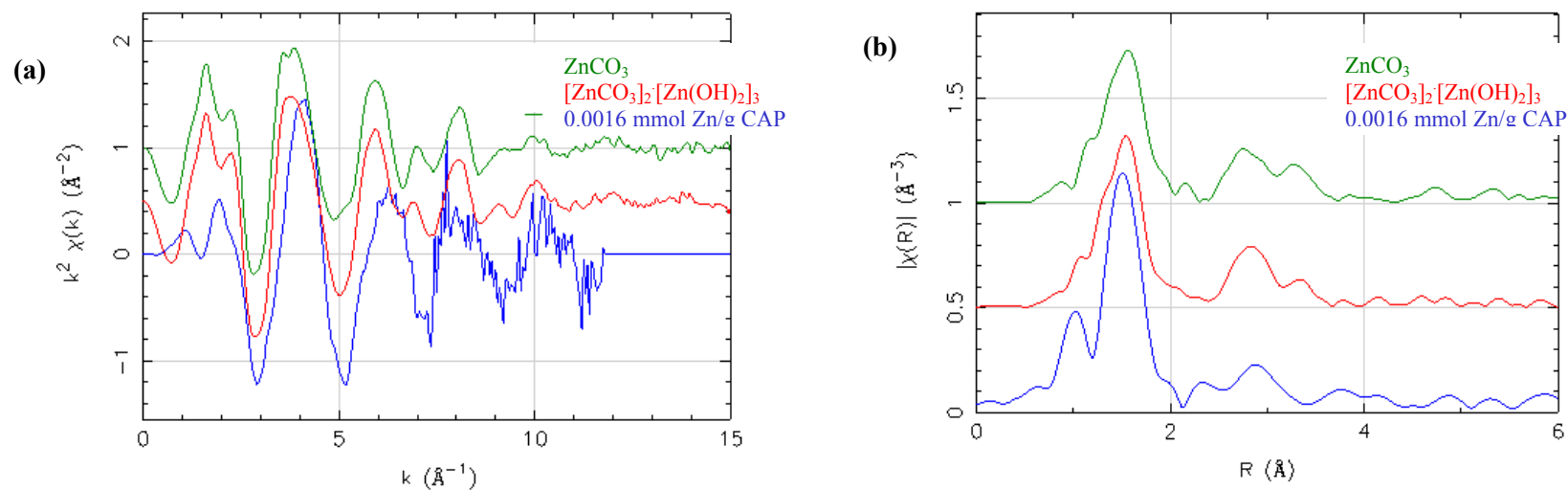
Figure B.9: (a) χ(k) & (b) χ (R) XAS spectra of 0.0016 mmol/g CAP, zinc carbonate, $ZnCO_3$ & zinc carbonate hydroxide, $[ZnCO_3]_2 \cdot [Zn(OH)_2]_3$
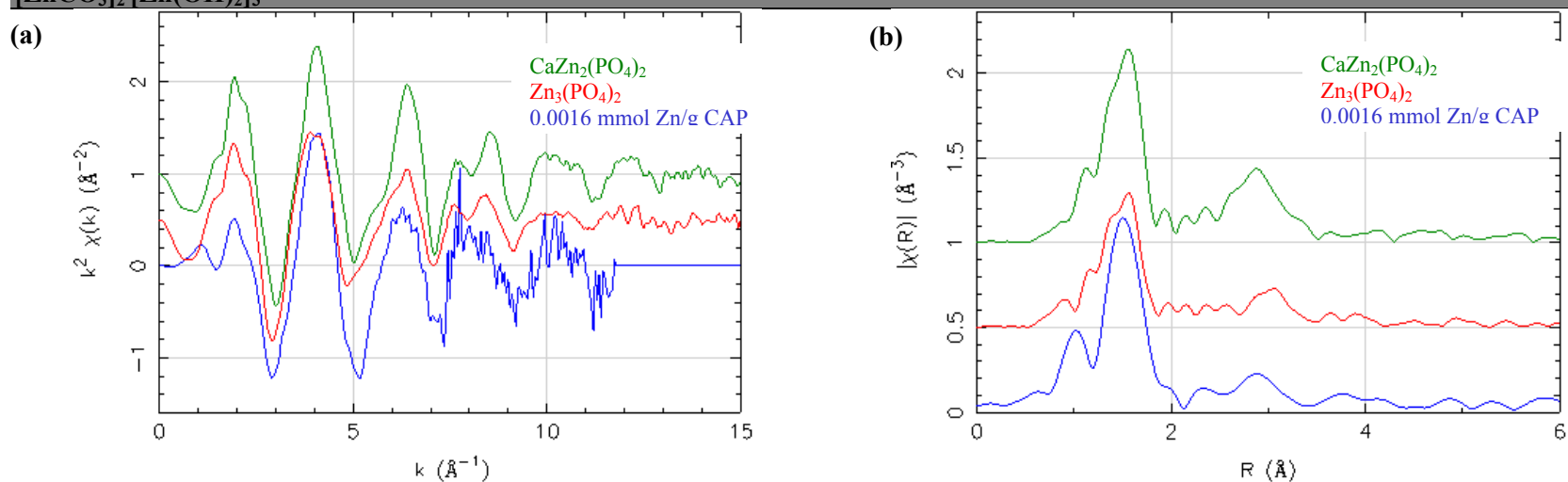
Figure B.10: (a) χ(k) & (b) χ (R) XAS spectra of 0.0016 mmol/g CAP, hopeite, $Zn_3(PO_4)_2$ & scholzite, $CaZn_2(PO_4)_2$
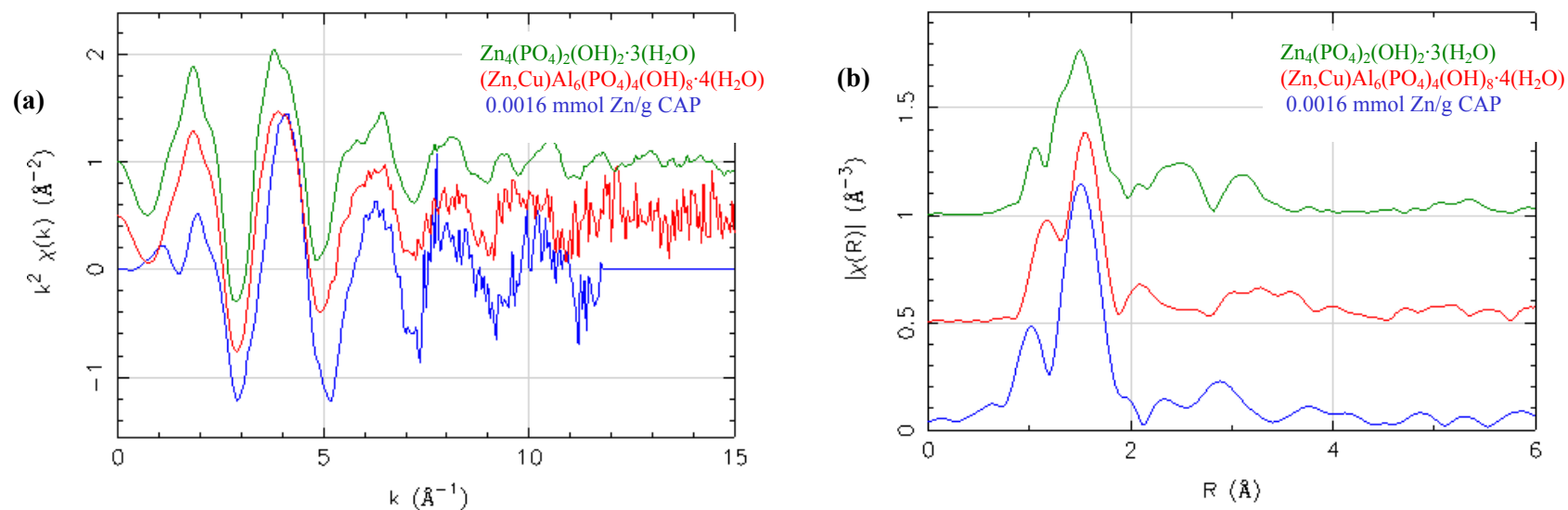
Figure B.11: (a) χ(k) & (b) χ (R) XAS spectra of 0.0016 mmol/g CAP, spencerite, $Zn_4(PO_4)_2(OH)_2 \cdot 3(H_2O)$ & faustite, $(Zn,Cu)Al_6(PO_4)_4(OH)_8 \cdot 4(H_2O)$
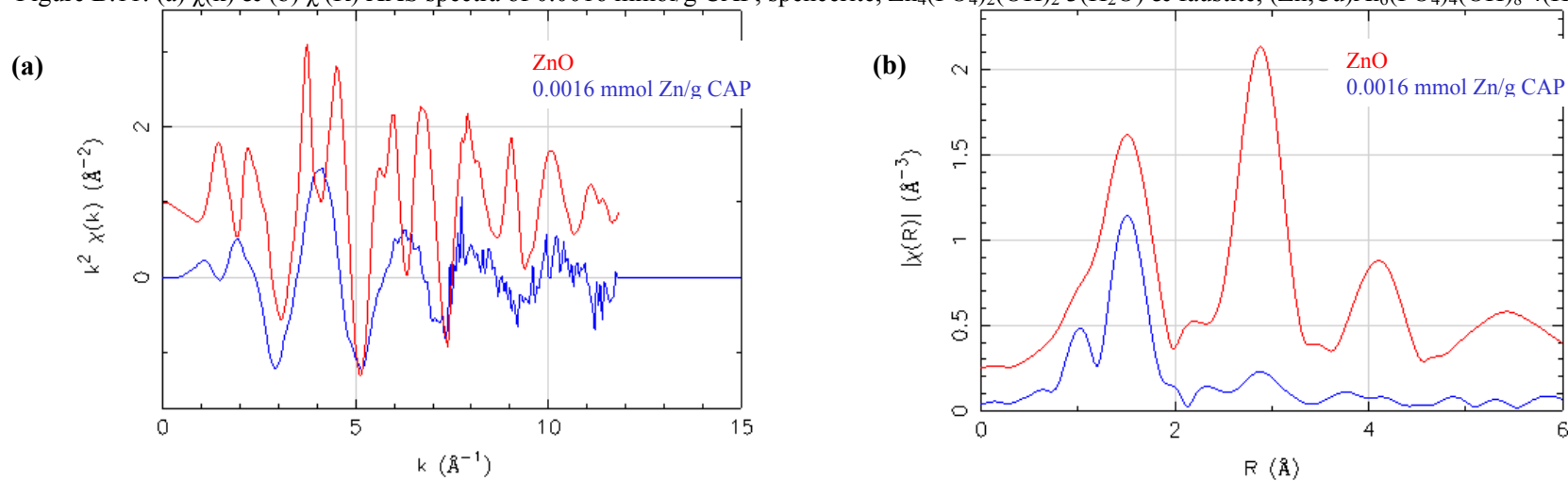
Figure B.12: (a) χ(k) **&** (b) χ (R) XAS spectra of 0.0016 mM/g CAP, & zinc oxide, ZnO
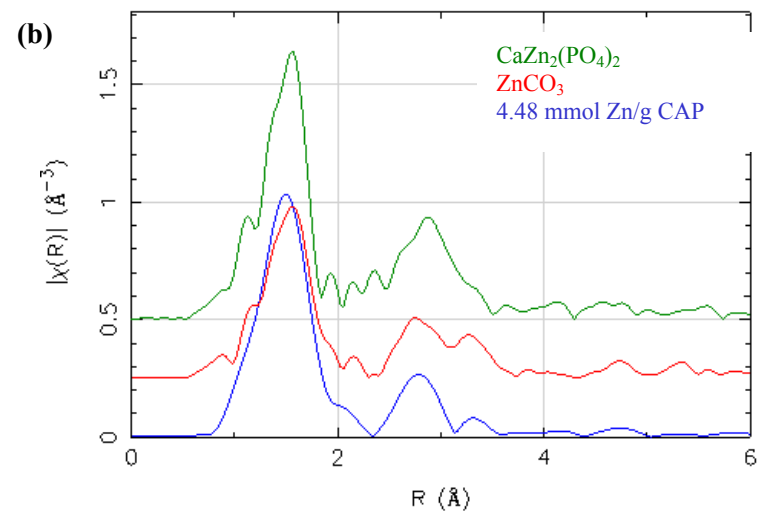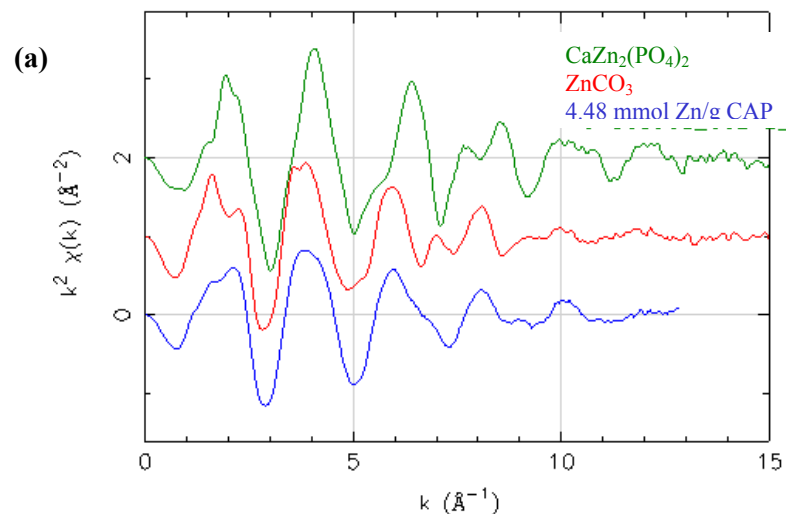
Figure B.13: (a) $\chi(k)$ & (b) $\chi(R)$ XAS spectra of 4.48 mmol/g HAP, zinc carbonate, $ZnCO_3$, & scholzite, $CaZn_2(PO_4)_2$
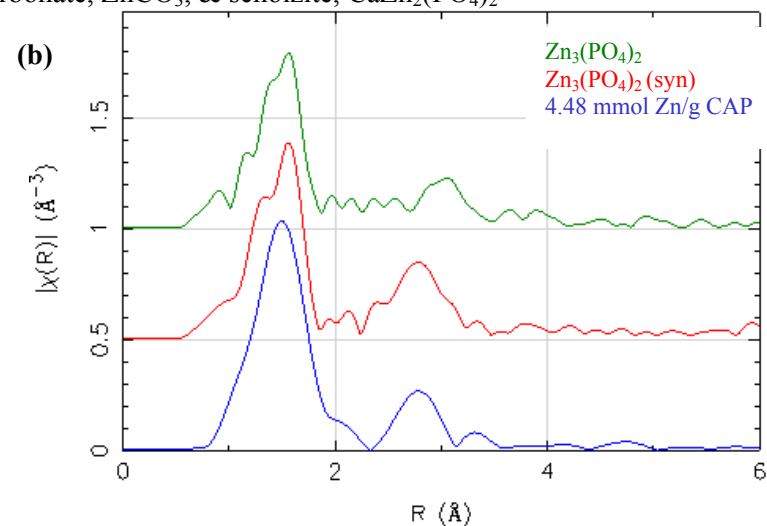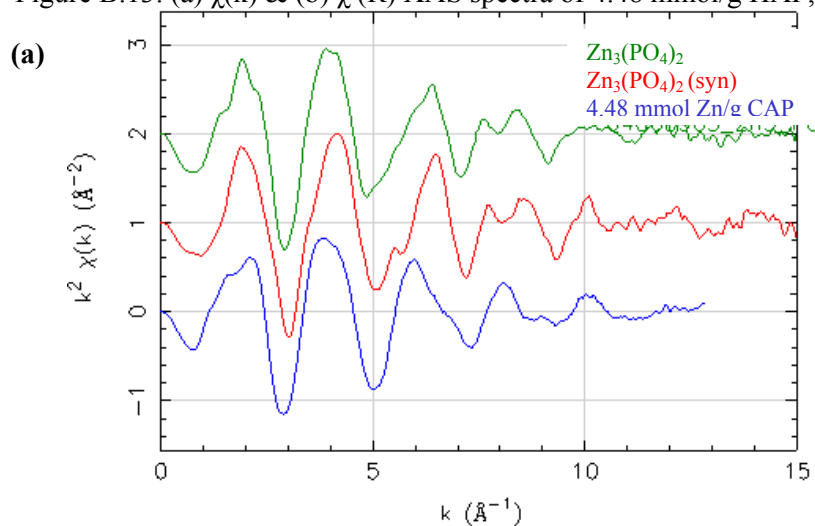
Figure B.14: (a) $\chi(k)$ & (b) $\chi(R)$ XAS spectra of 4.48 mmol/g CAP, synthetic zinc phosphate, $Zn_3(PO_4)_2$ & hopeite, $Zn_3(PO_4)_2$
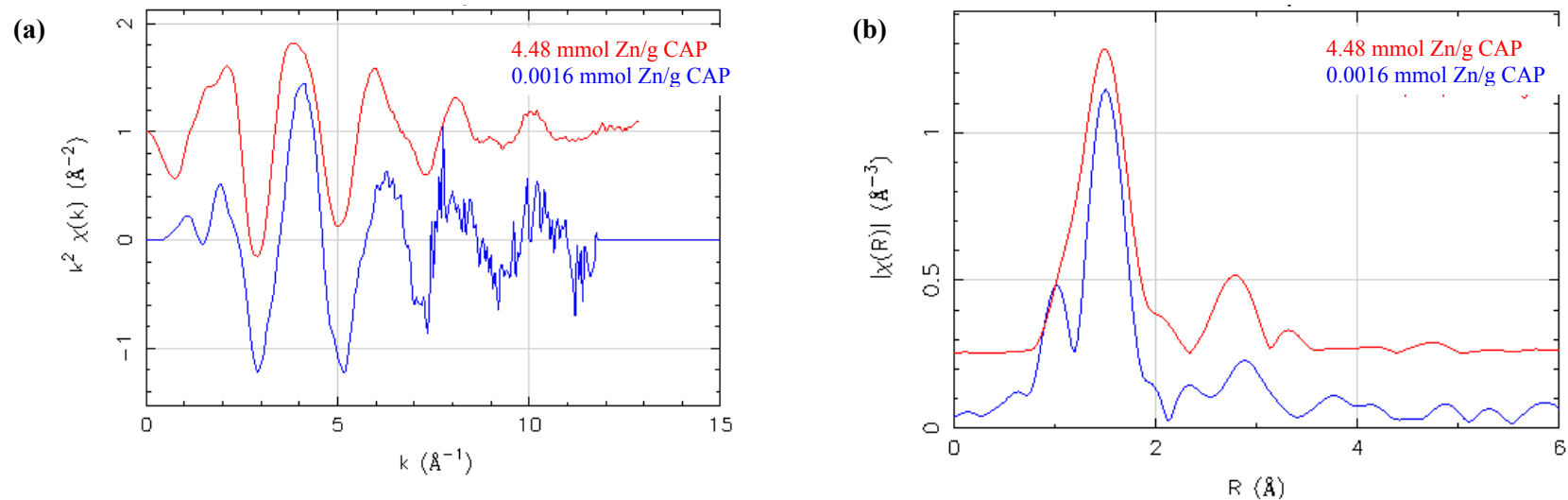
Figure B.15: (a) χ(k) & (b) χ(R) XAS spectra of 0.0016 mmol/g CAP & 4.48 mmol/g CAP
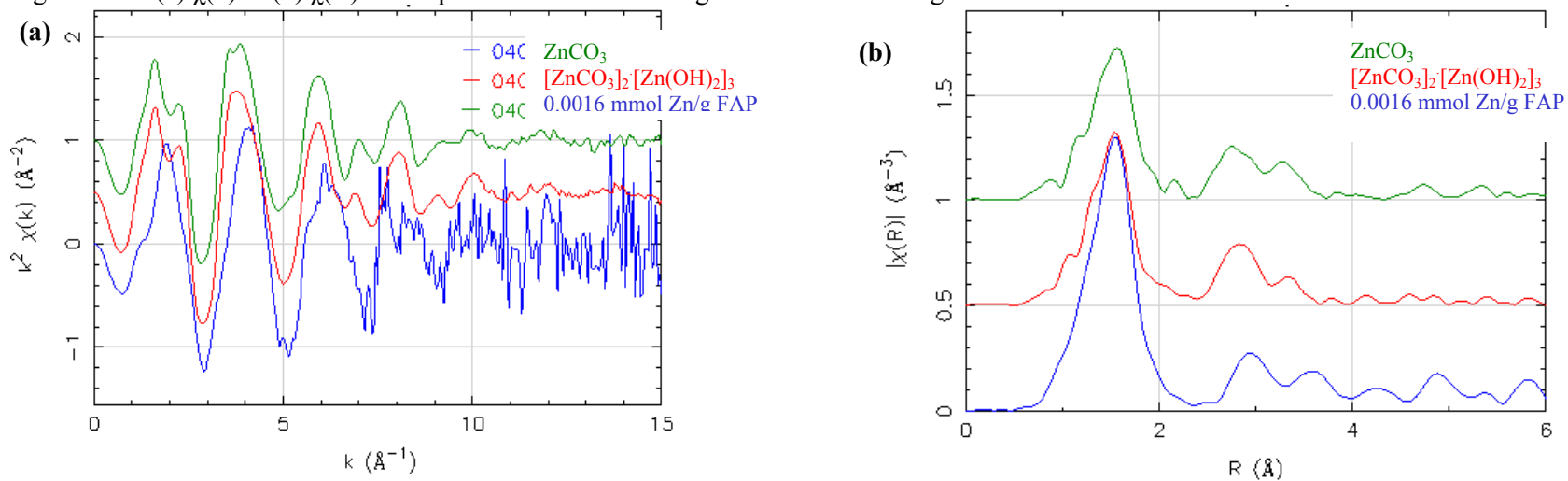
Figure B.16: (a) χ(k) & (b) χ(R) XAS spectra of 0.0016 mmol/g FAP, zinc carbonate ZnCO$_3$ & zinc carbonate hydroxide, [ZnCO$_3$]$_2$·[Zn(OH)$_2$]$_3$
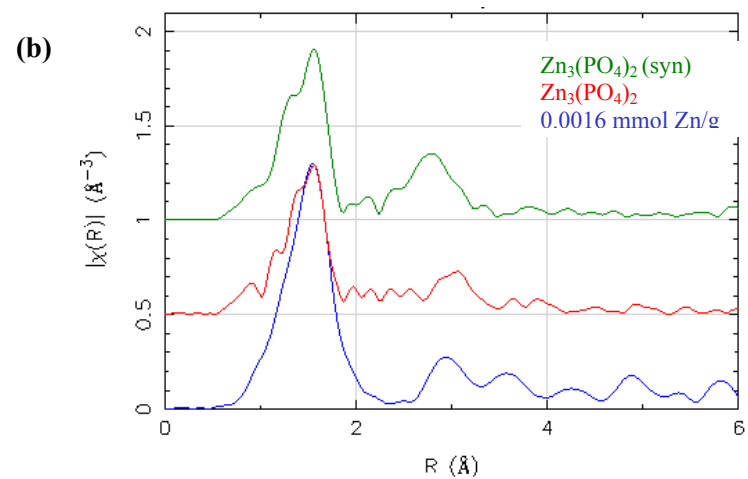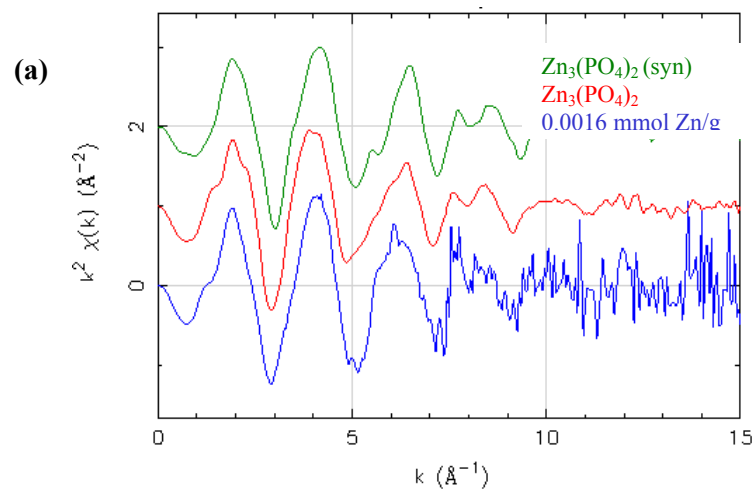
Figure B.17: (a) χ(k) & (b) χ (R) XAS spectra of 0.0016 mmol/g FAP, synthetic zinc phosphate, $Zn_3(PO_4)_2$ & hopeite, $Zn_3(PO_4)_2 \cdot 4H_2O$
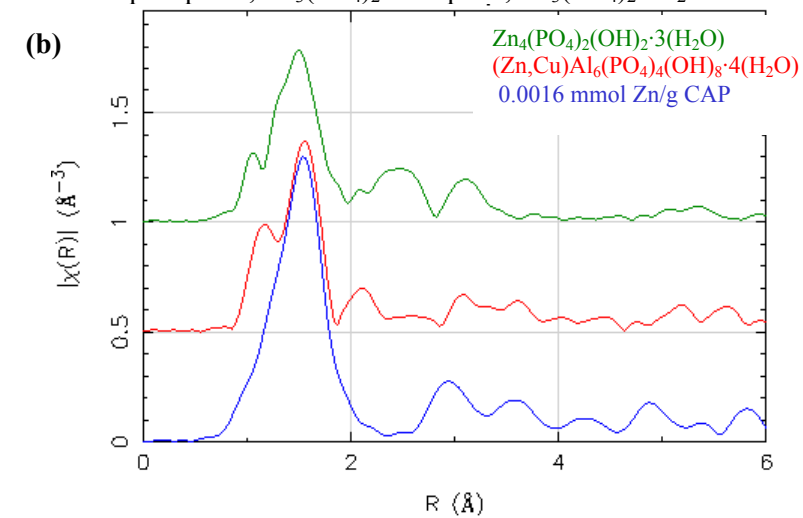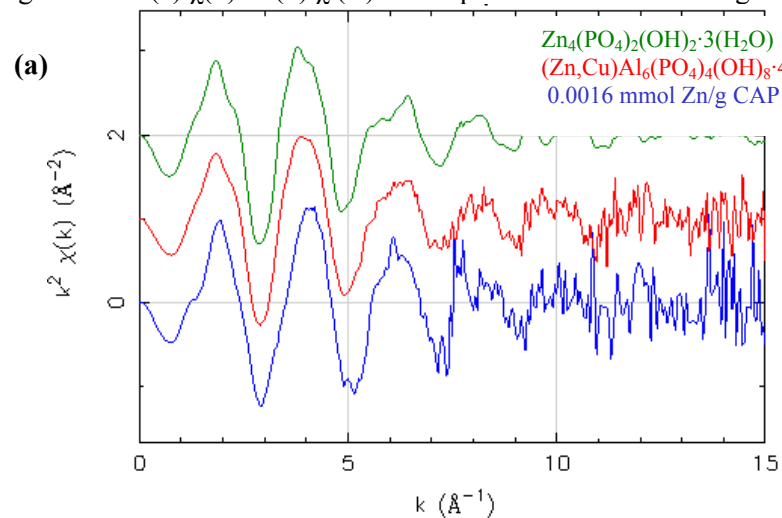
Figure B.18: (a) χ(k) & (b) χ (R) XAS spectra of 0.0016 mmol/g FAP, spencerite, $Zn_4(PO_4)_2(OH)_2 \cdot 3(H_2O)$ & faustite, $(Zn,Cu)Al_6(PO_4)_4(OH)_8 \cdot 4(H_2O)$
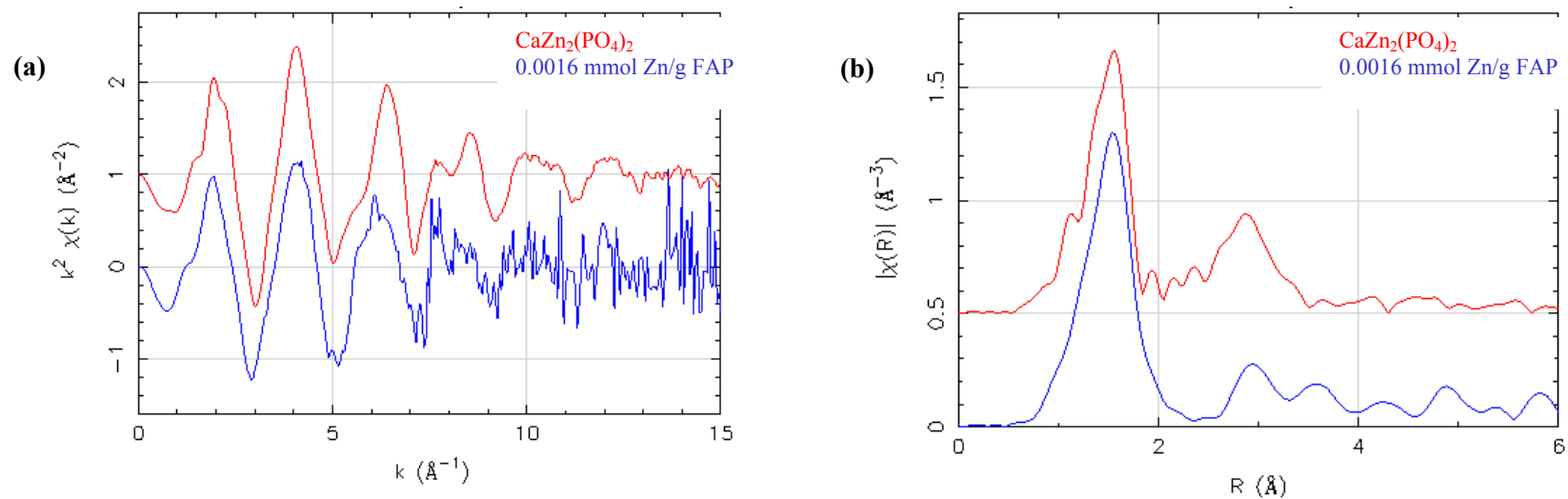
Figure B.19: (a) χ(k) & (b) χ (R) XAS spectra of 0.0016 mmol/g FAP & scholzite, CaZn2(PO4)2
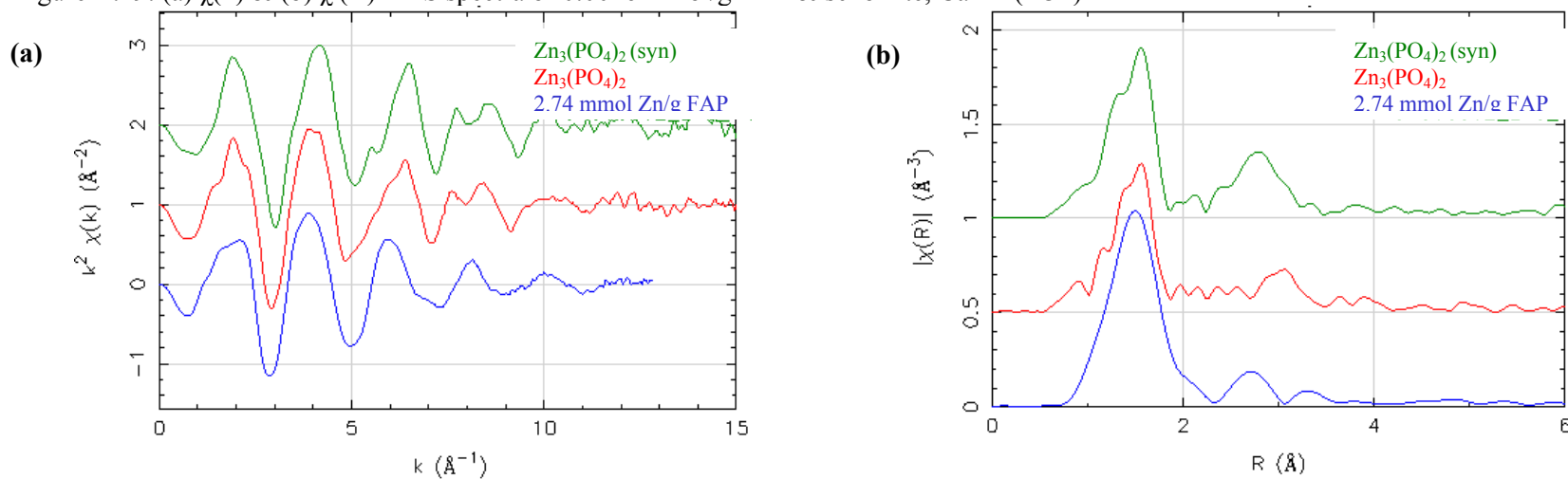
Figure B.20: (a) χ(k) & (b) χ (R) XAS spectra of 2.74 mmol/g FAP, synthetic zinc phosphate, $Zn_3(PO_4)_2$ & hopeite, $Zn_3(PO_4)_2 \cdot 4H_2O$
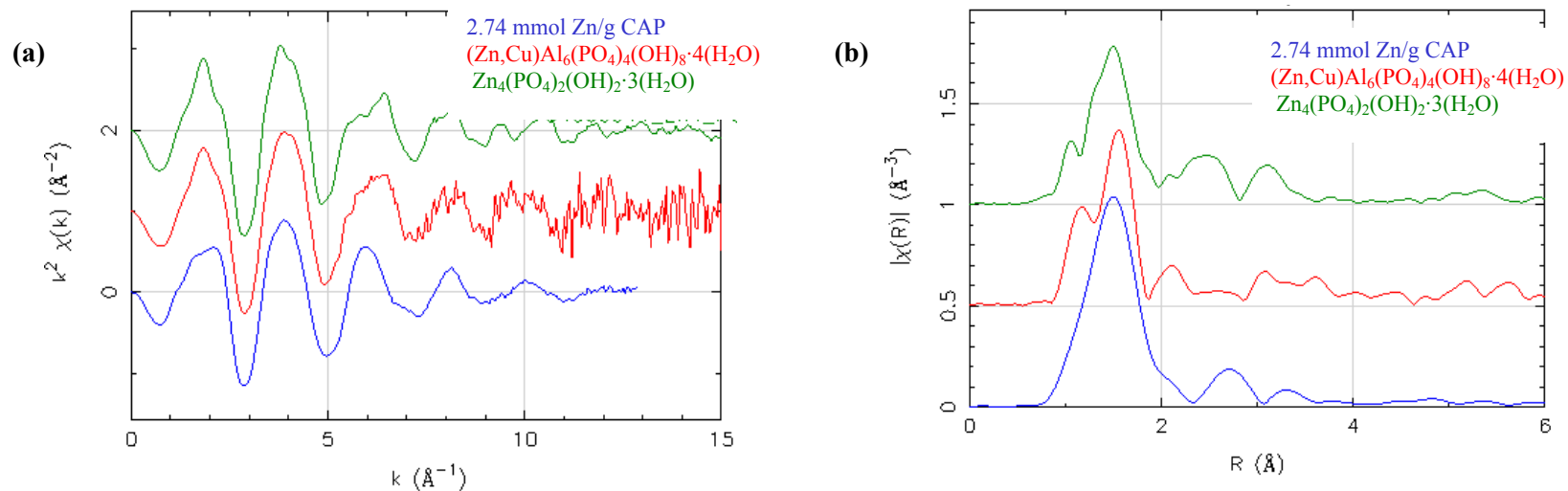
Figure B.21: (a) χ(k) & (b) χ (R) XAS spectra of 2.74 mmol/g FAP, spencerite, $Zn_4(PO_4)_2(OH)_2 \cdot 3(H_2O)$ & faustite $(Zn,Cu)Al_6(PO_4)_4(OH)_8 \cdot 4(H_2O)$
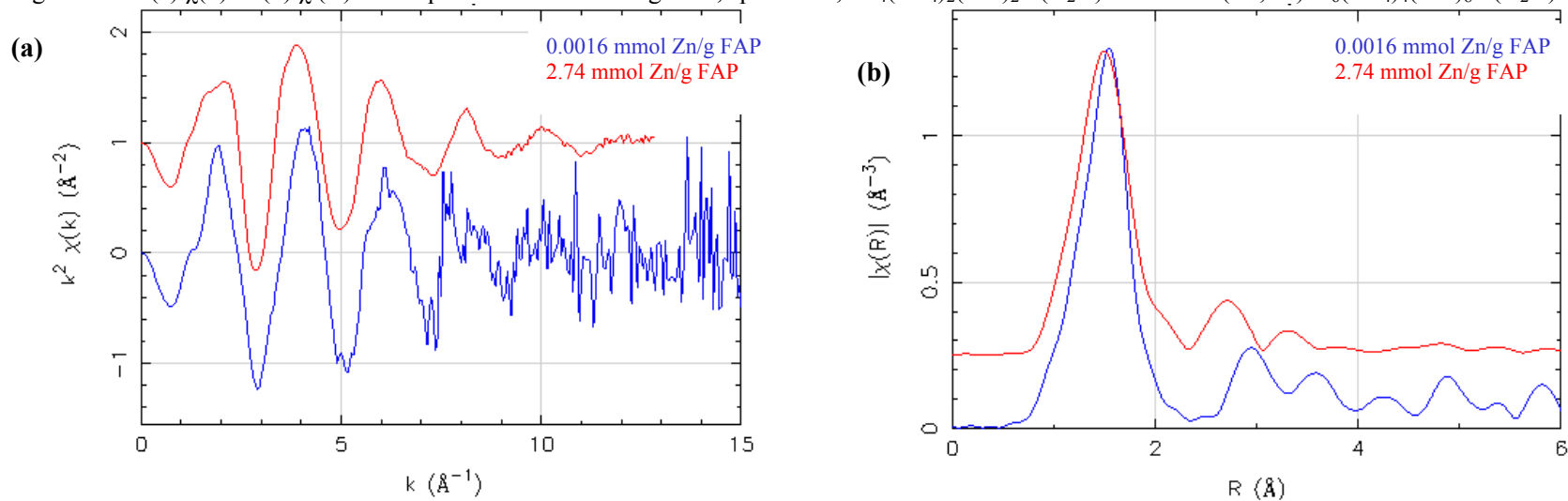
Figure B.22: (a) χ(k) & (b) χ (R) XAS spectra of 0.0016 mmol/g FAP & 2.74 mmol/g FAP

APPENDIX C

Co-precipitate XRD Spectra

Figure C.1 and C.2 display the XRD spectra of the two co-precipitates prepared in the lab by methods described in section 3.3. C.1 was prepared with the intention of obtaining a co-precipitate with the empirical formula $(Ca_4,Zn)(PO_4)_3OH$ and C.2 with the formula $(Ca,Zn_4)(PO_4)_3OH$. C.1 is compared to HAP and CAP from the ICDD database and C.2 is compared to HAP and carbonate fluoroapatite (CFH). Figure C.1 indicates that poor crystallinity was obtained for the low Zn-substituted co-precipitate.
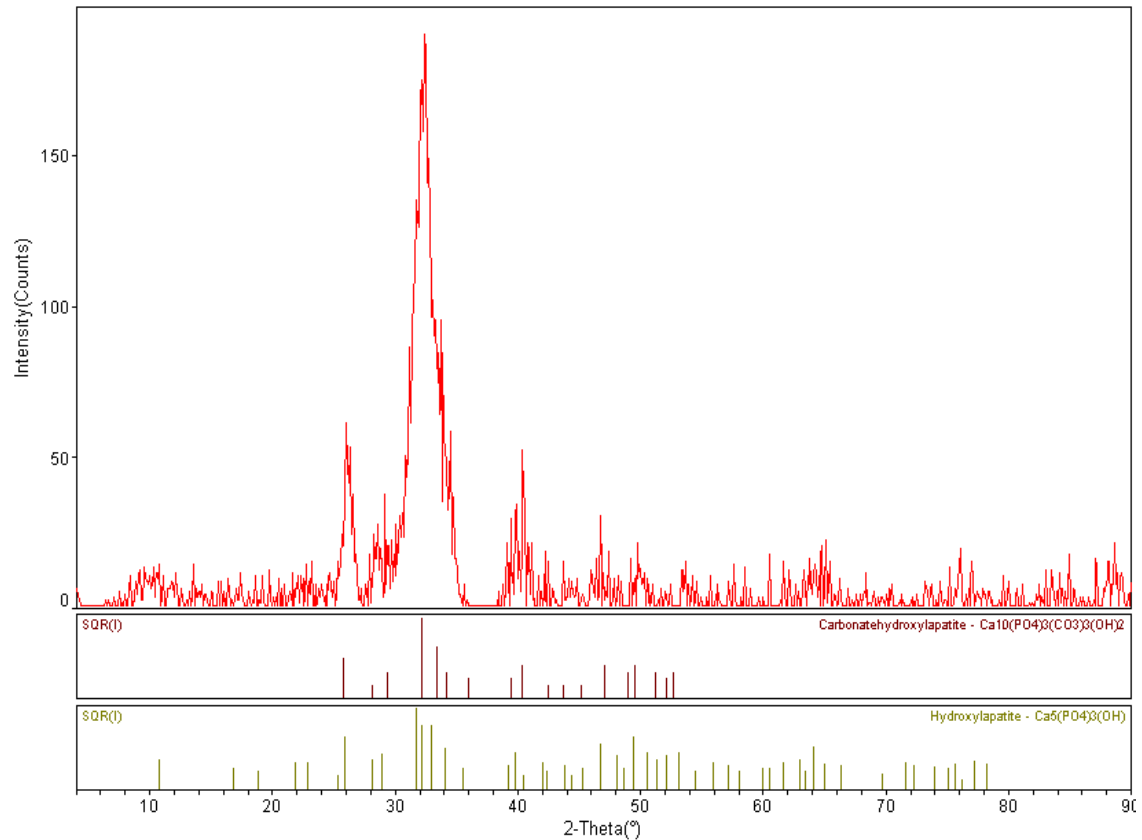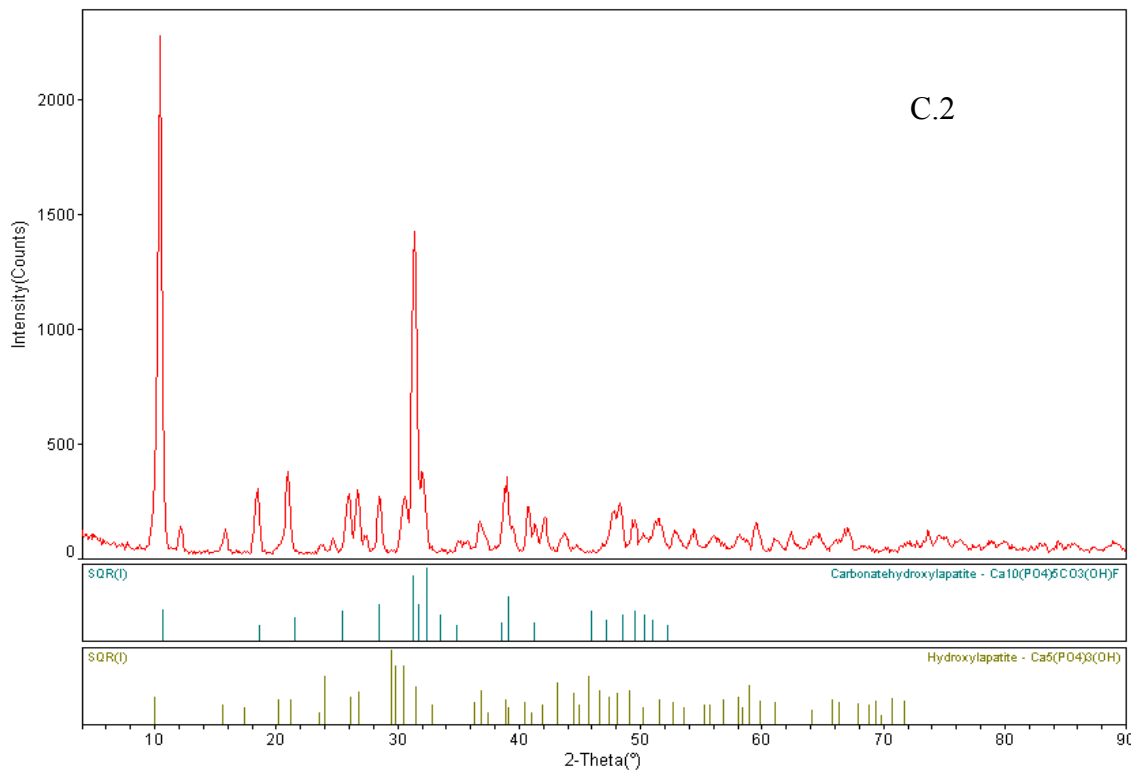
APPENDIX D

HYDRUS 2D

By

Jean Lebrun
Ecole Centrale de Nantes, France

In order to expand the investigation of contaminant behavior in a permeable reactive barrier made of apatite, HYDRUS 2D was used to analyze water flow and solute transport in variably saturated porous media. HYDRUS 2D is a hydro-dynamic and solute transport modeling program based on a finite element model. This phase of the project was conducted by Jean Lebrun from the Ecole Centrale de Nantes, France, as part of an internship at the University of New Hampshire. HYDRUS 2D was used to model the contaminant fate and transport of heavy metals and oxyanions (Cd, Pb, As, Cr, Cu and Zn) in a simulated permeable reactive barrier system. A 1-dimensional column was set up to have the characteristics and properties of a natural apatite. Both saturated and unsaturated conditions were studied, varying both boundary and initial conditions.

HYDRUS 2D uses the Langmuir isotherm (equation 2.1) to model adsorption. The following parameters were used to run the simulations:

Table D.1: Adsorption Parameters used for Saturated Media Simulations

Element	K_{ads} (L/mg)	q_{max} (mg/g)	C (m^3/kg)
Cd	0.015	32.37	0.48555
Pb	2.38	293	697.34
As	2.248	0.167	0.37541
Cr	1.18	0.069	0.08142
Cu	0.129	12.98	1.67442
Zn	0.008	47.24	0.37792

Saturated Water Flow:

For the saturated water flow simulations, the column was designed to have a height of 2 m and a width of 40 cm. Constant pressure was set at the top and bottom of the column to establish a constant water flow. The 1D column was divided into three sections, the uppermost section was set to be loam containing the contaminants at a concentration of 100 kg/m^3, next was the section containing sand (starting at a depth of

1.42 m and ending at 1.93 m) used to simulate the apatite, finally the lowermost section was loam. Sand was used to simulate the apatite section as the size characterization of the natural apatite shows that it has similar grain size distribution. HYDRUS-2D uses the USDA Textural Classes as the soil parameters used in the simulations; for the present scenario the following parameters were utilized:

Table D.2: Soil Parameters used for Saturated Media Simulations

	θ_r	θ_s	α (m^{-1})	n	K_s (m/day)
Loam	0.078	0.43	3.6	1.56	0.2496
Sand	0.045	0.43	14.5	2.68	7.128

Where:

θ_r = the residual soil water content

θ_s = the saturated soil water content

α = the parameter in the soil water retention function

n = the parameter n in the soil water retention function

K_s = the saturated hydraulic conductivity

Simulations were run for 500, 5000 and 50,000 days.

Unsaturated Water Flow:

For the unsaturated model a 1D, vertical column scenario was also used. The initial contaminant concentration remained the same, however in this case the column was 3 m long, with 1.30 meters of recycled material at the top, 40 cm of apatite (sand soil parameters used as well) and 1.30 m of loam at the bottom. Soil parameters were calculated with the Rosetta program, which estimates unsaturated hydraulic properties based on soil data (soil texture data, bulk density, etc.). The following parameters were used:

Table D.3: Parameters used for Unsaturated Media Simulations

	θ_r	θ_s	α (m-1)	n	K_o (m/day)
Loam	0.078	0.43	3.6	1.56	0.2496
Sand (Apatite)	0.0507	0.3760	3.44	4.42	0.40
Recycled Material	0.07	0.33	41.59	1.99	1.3

* K_o = unsaturated hydraulic conductivity

To simulate the unsaturated water flow scenario, intermittent rainfall was simulated to occur every three days for fifteen minutes/day. Pressure conditions were set to zero at the bottom of the column and –3 at the top, with a linear distribution throughout the column. Simulations were run from 500 – 1000 days.

RESULTS:

Figures D.1, D.2 and D.3 display the results for Zn under saturated conditions and figures D.4 and D.5 the results for unsaturated conditions. The initial [Zn] in the upper 1.3 m of the column was 100 kg/m^3. The graphs represent the distribution of the contaminant at the given time period. The apatite barrier is depicted as a rectangle.

Saturated Water Flow:
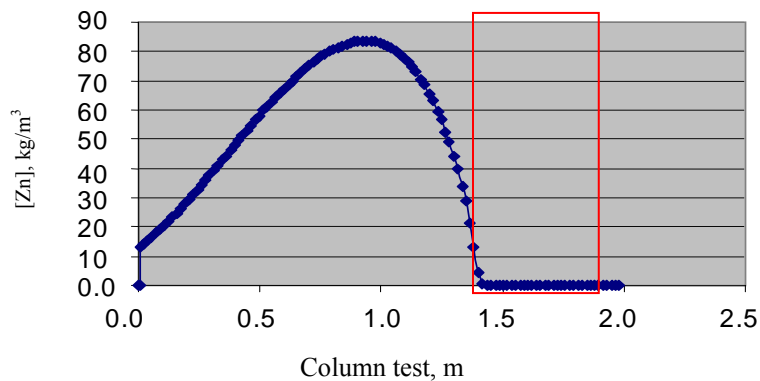
Figure D.1: [Zn] at 500 days under saturated conditions

After 500 days the contaminant has just begun to reach the barrier, most of the contaminants still reside in the upper loam section.
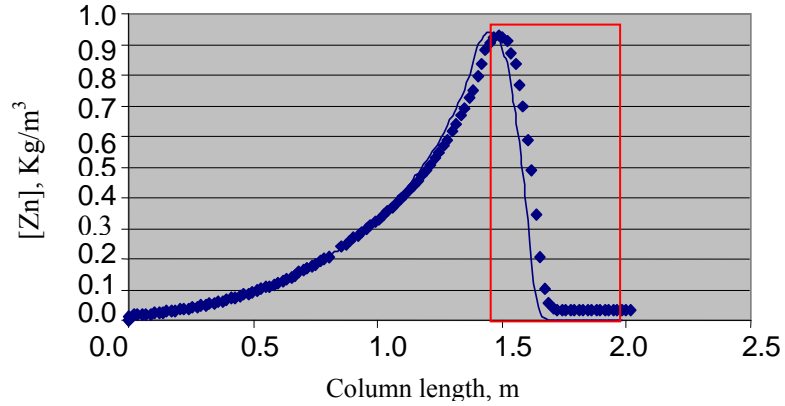
Figure D.2: [Zn] at 5,000 days for saturated conditions

After 5,000 days the contaminants have descended within the column reaching the apatite barrier, concentrations drop dramatically in the barrier, enough so that contaminant levels below the barrier remain at zero. This indicates that the barrier is successful at trapping the contaminant.
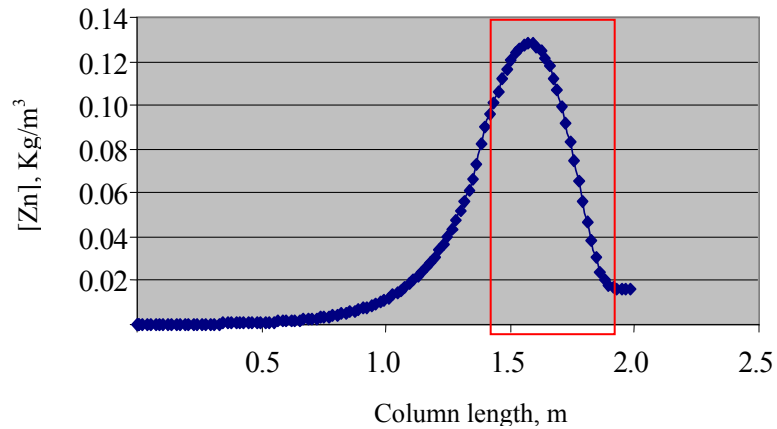
Figure D.3: [Zn] at 50,000 days for saturated conditions.

After 50,000 days the vast majority of the contaminants have reached the barrier, the barrier is successful at reducing the concentrations significantly, however some of the contaminants did pass through the barrier indicating that it was not able to completely immobilize the [Zn]. It is important to consider that initial [Zn] is considerably high (100 Kg/m^3), this was done to simulate a highly contaminated scenario, but shows that under very contaminated conditions a thicker barrier would be necessary (> 50 cm).

Unsaturated Water Flow:

After 500 days under unsaturated water flow conditions the concentration of Zn at the top of the column has dropped to zero, most of the contaminants reached the apatite barrier, where [Zn] drop dramatically. Below the barrier [Zn] is zero, indicating that the PRB was successful at containing the contaminant.

At 1000 days the contaminant front has not progressed much in comparison to the 500 days scenario. As in the 500 days scenario the apatite PRB is successful at immobilizing the contaminant in that concentrations below the barrier are zero.
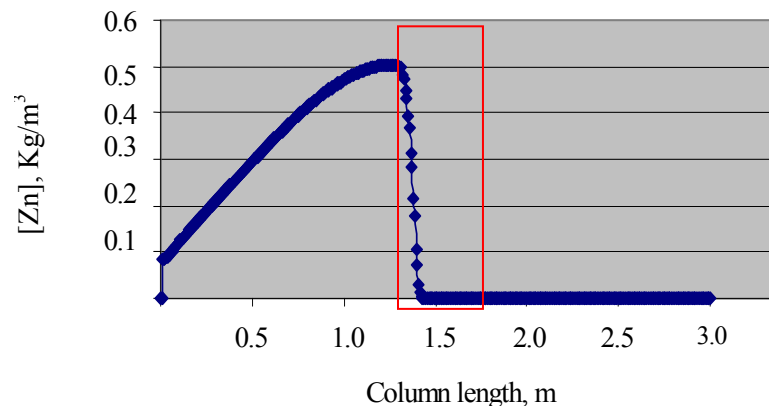
Figure D.4: [Zn] at 500 days for unsaturated conditions
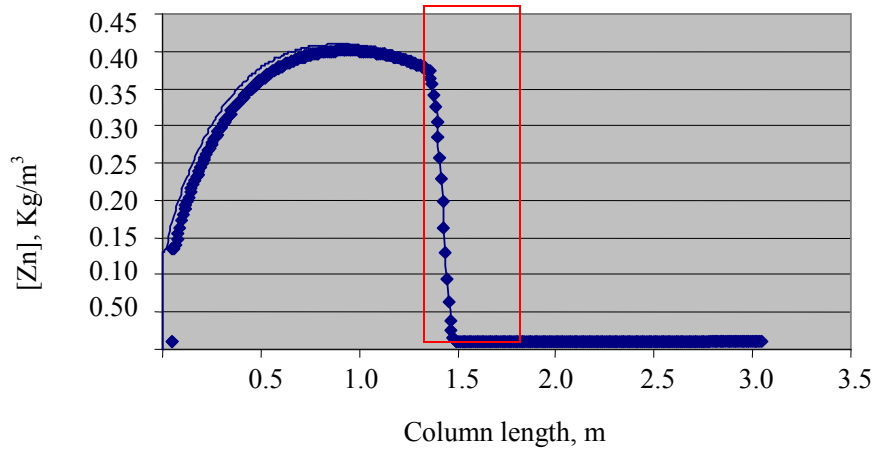
Figure D.5: [Zn] at 1,000 days for unsaturated

In interpreting the results from HYDRUS 2D it is important to consider the influence of the input parameters. The B_{max} = 47.24 mg/g (0.722 mmol/g) utilized is a conservative parameter in comparison to the B_{max} observed in the sorption isotherms conducted in this research. The adsorption coefficient, K_{ads} = 0.008 L/mg, is also conservative, as apatite has been reported to have a high affinity for Zn by other authors ranging from 550 – 175,000 mL/g (Wright, 2005; Eighmy, unpublished). Having used conservative parameters and still obtaining favorable results HYDRUS 2D supports the use of apatite as a PRB for contaminant control of heavy metals.